Dissertation for the Degree of Doctor of Philosophy

# A Study on Einzel Lens Design and Fabrication for a Microcolumn

**by**

**Om Krishna Suwal**

**June 2013**

**Department of Physics and Nanoscience**

**Graduate School**

**Sun Moon University**

**Republic of Korea**

# A Study on Einzel Lens Design and Fabrication for a Microcolumn

**by**

**Om Krishna Suwal**

**Supervisor: Ho Seob Kim**

**June 2013**

**Department of Physics and Nanoscience**

**Graduate School**

**Sun Moon University**

**Republic of Korea**

# A Study on Einzel Lens Design and Fabrication for a Microcolumn

by

**Om Krishna Suwal**

Dissertation submitted to the

Department of Physics and Nanoscience

and the Graduate School of Sun Moon University

in partial fulfillment of the

requirements for the degree of

**Doctor of Philosophy**

June 2013

# CERTIFICATE OF APPROVAL

THIS DISSERTATION **"A STUDY ON EINZEL LENS DESIGN AND FABRICATION FOR A MICROCOLUMN"** WRITTEN BY **OM KRISHNA SUWAL** HAS BEEN APPROVED AFTER APPROPRIATE EXAMINATION AND STANDARDS SUCCESSFULLY MET FOR THE **DEGREE OF DOCTOR OF PHILOSOPHY** IN THE DEPARTMENT OF PHYSICS AND NANOSCIENCE, SUN MOON UNIVERSITY, KOREA.

Defense Date: June 24, 2013

**Dae-Wook Kim, Ph.D., Professor (*Chairperson*)**
Department of Physics and Nanoscience,
Sun Moon University

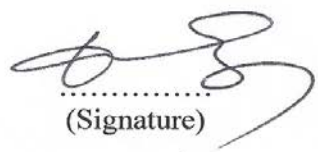
(Signature)

**Won Kweon Jang, Ph.D., Professor**
Division of Electronics, Computer and
Communication Engineering, Hanseo University

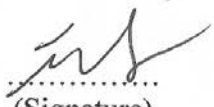
(Signature)

**Young Chul Kim, Ph.D., Ass. Professor**
Department of Optometry,
Eulji University

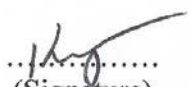
(Signature)

**Seungjoon Ahn, Ph.D., Professor**
Department of Physics and Nanoscience,
Sun Moon University


(Signature)

**Ho Seob Kim, Ph.D., Professor (*Supervisor*)**
Department of Physics and Nanoscience,
Sun Moon University


(Signature)

**Graduate School, Sun Moon University**

# Acknowledgements

First of all, I would express my acknowledgement to my dissertation advisor Prof. Ho Seob Kim whose guidance and dedication to perfection helped me to be what I am today. I am very thankful to dear Prof. Dae Wook Kim for academic guidance, moral supports, continuous caring, and inspiration.

I am also grateful to technicians, engineers, and staffs of Center of Electron Beam Technology (CEBT), and Korea Institute of Science and Technology (KIST) for providing me laboratory facilities and supports in the course of experiments.

I acknowledge Mr. Youngbuk Lee, Ms. Anjli Sharma, Mr. Sanjeev Kanth, and Mr. Seong Woong Choi for kind cooperation in lab works. Special thanks goes to my colleague Mr. Vinaya Kumar Jha for always being supportive during my Ph. D. study at the same lab.

I am thankful to all the Nepalese communities at Sun Moon University and Seoul National University for helping me in many directions during my stay in Korea.

I am very obliged to my mother Ms. Mangal Maiya Suwal, father Mr. Hari Krishna Suwal, brother Sunil, and sisters Roshan Maiya, Meena, and Sunita for their eternal love and care and allowing me far for the study with all kinds of supports. I could stand tall because of strong emotional supports from my beloved wife Puna Maya Maharjan, whose passion and love always delights me for stepping ahead.

# TABLE OF CONTENTS

# LIST OF FIGURES

# LIST OF TABLES

# ABBREVIATIONS

| | |
|---|---|
| DRIE | Deep reactive ion etching |
| E1 | First electrode of Einzel lens |
| E2 | Middle electrode of Einzel lens |
| E3 | Third electrode of Einzel lens |
| EPMA | Electron Probe Micro Analyzer |
| ES | Electrostatic |
| FESEM | Field Emission Scanning Electron Microscope |
| FOV | Field of view |
| PR | Photoresist |
| S1 | Extractor, first lens-electrode of source lens |
| S2 | Accelerating electrode, second electrode of source lens |
| S3 | Limiting aperture electrode, third electrode of source lens |
| SAFE | Self aligned field emitter |
| STM | Scanning tunneling microscopy |
| WD | working distance |

**Abstract**

A Study on Einzel Lens Design and Fabrication

for a Microcolumn

Om Krishna Suwal

Department of Physics and Nanoscience

Graduate School of

Sun Moon University

Supervisor: Prof. Ho Seob Kim

Miniaturization of an electron optical system has been one of the core research interests after the first development of microcolumn in 90s. The microcolumn is composed of a micro-electron emitter, a miniaturized electrostatic source lens, deflectors, and a miniaturized objective lens. Although steady improvements have been reported on the performance and characteristics on microcolumn, some challenges are still remained in the fabrication and optimization for the design of each component composing a microcolumn. Among them, this work focuses on the design and fabrication of electrostatic lenses and the analysis on the microcolumn performance depending on Einzel lens structure.

Two types of electrostatic lenses have been designed, fabricated, and analyzed; the first one is thin Si membrane supported by bulk Si and other is supported by Pyrex and both types have a circular aperture at the center of Si membrane. In the first case, there is limit in controlling gap between lenses though the surface area of membrane is smaller than later one. In the latter case, we can control the gap freely and get flexibilities in the design of source or Einzel lens structures.

In Chapter II, the simulation results on the variation of electrostatic potential and field depending on the lens types are analyzed. Also, in order to investigate the influence of gap between the lens-electrodes in an Einzel lens, a few types of Einzel lenses were studied by varying the gap from 150 to 500 μm. The variations of scan range have been analyzed in retarding mode operation using either one-lens or two-lens focusing method.

Experiments including the fabrication of electrostatic lenses and the assembly of microcolumns are described in Chapter III in details. We successfully developed the lens fabrication techniques for membrane type lens-electrodes exploiting micro-electro-mechanical systems (MEMS) processes, and the multiple lens-electrodes were properly aligned along the optical axis using the well-known laser diffraction technique with the alignment accuracy of ~1 μm.

To realize the simulation results in practice, we assembled two types of microcolumns having different Einzel lens structures. The experimental results on these microcolumns obtained in both one-lens and two-lens focusing modes are described in Chapter IV. Image quality, scan range, and resolution were varied depending on the modes of operation for different Einzel lens structures.

As in simulation results, the scan range increases with the decrease of the gap in source lens focusing mode, while the trend is reversed in two-lens focusing mode. The criteria of gap adjustment in the design of Einzel lens structure for wider scan range are discussed.

# 1 CHAPTER I: INTRODUCTION

Since the miniaturization of an electron optical system first proposed by Chang et al. [1] in late 1980s, there have been immense interests in the fabrication of a suitable microcolumn for various purposes, such as low-cost portable scanning electron microscope (SEM) [2-4], direct e-beam lithography [5-12], and parallel beam inspection tools [13-15]. The column is ~1 cm in length and made of electrostatics components; and it is strictly optimized for low voltage operation. As the column is small and components are electrostatic, MEMS fabricated Si components are used in a microcolumn which keeps lower operating cost because vacuum, power, and facility requirements are minimal. Moreover, the small size allows the columns to be assembled into arrays and operated parallel, providing high-throughput imaging or lithography capability [9, 16]. Basically, electron-electron interaction gets minimized in ultra-short columns and therefore should support higher beam currents by gaining electron collection efficiency.

The Major components of microcolumn, as shown in Fig. 1.1, are (i) an electron emitter as an e-beam source, (ii) source lens for extracting, accelerating and limiting beam size, (iii) deflectors for wide field of view and magnification, and (iv) Einzel lens for focusing e-beam without altering its energy. The effective e-beam size of such column is given as [17]:

$$d_1^2 = (Md_0)^2 + d_d^2 + d_{C_s}^2 + d_{C_c}^2$$

where, $d_1$ = probe size, M = column magnification, $d_0$ = virtual source size, $d_d$ = $1.5/\alpha_1\sqrt{V}$, V = beam energy, $d_{Cs} = 0.25\ C_s\ \alpha_1^3$, $d_{Cc} = C_c\ \alpha_1\ \Delta V/V$, $C_s$ = spherical aberration coefficient, and $C_c$ = chromatic aberration coefficient.

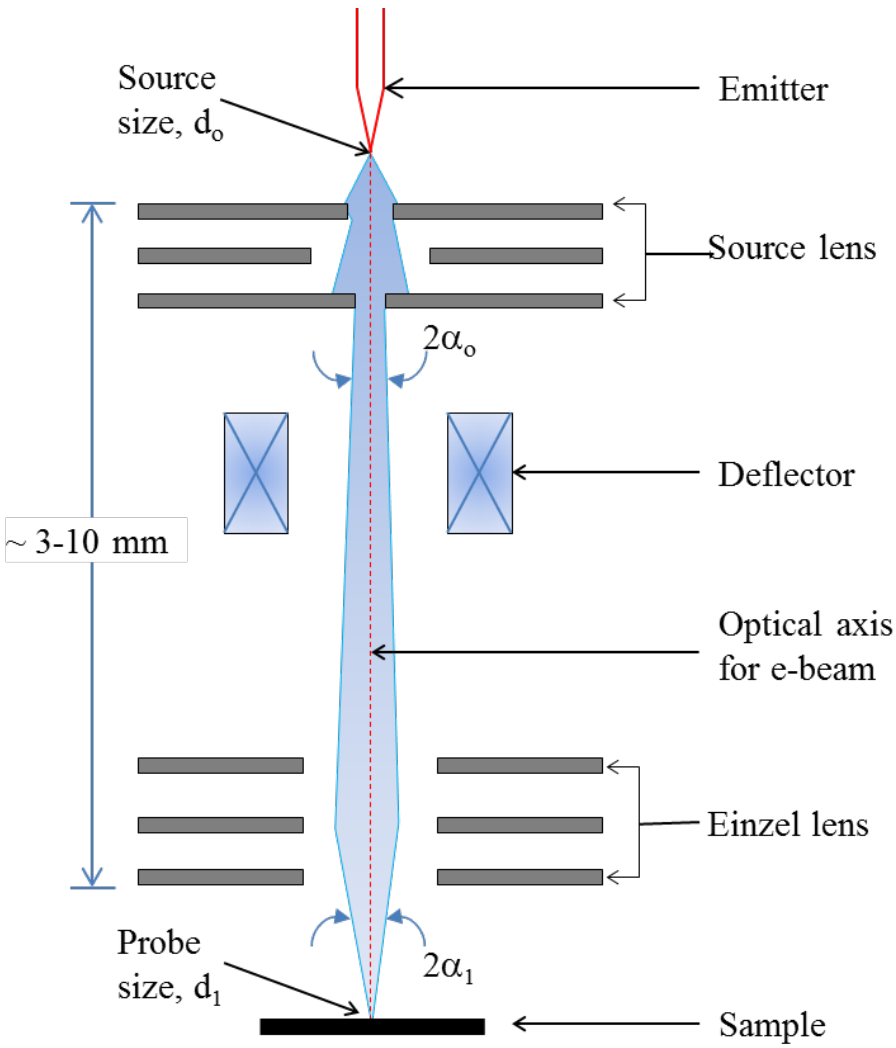


**Fig. 1.1** A schematic cross section of an electron optical system, simply known as microcolumn.

The desire of miniaturization of an electron microscopy has been realized after crucial evolvement of miniaturized micro-lenses with field emission emitter. As all the components are fabricated through MEMS technology, the overall size of microcolumn is ~1 cm in size, and the device is optimized for low voltage e-beam column. IBM research group [1, 18, 19] at the end of 90s first unwrapped the potentiality of miniaturized e-beam column by reporting a scanning tunneling microscope (STM) controlled field emission tip in conjunction with microlenses. The tip was aligned with miniaturized electron lens with STM feedback to form a self-aligned field emission (SAFE) microsource to achieve a significant improvement in emission stability and noise [1]. The microsource was immediately used with combination of magnetic lens achieving ~4 nm resolution [1].

The focusing power and beam spot size of electrostatic lens is known to function of applied voltage and lens size [20]. Muray et.al [21] presented a complete 1-keV electron beam microcolumn acquiring field ranging from 10-100 μm with image resolution 200 nm and it was expected to achieve probe size 8 nm with beam semi-convergent angle of 2.5 mrad at 1 mm working distance. The use of Si membrane as an electrode and Pyrex as a spacer in electrostatic lenses have been investigated for miniaturized electron column [22] for aberration-free e-beam focusing with smaller, as possible as, spot size.

Several papers report about an electron beam microcolumn which enable to focus ~10 nm size at 1 nA beam current at working distance ~1 mm using Si membrane lens electrodes [9, 23-26]. Thomson and Chang [26] suggests that the performance of Einzel lens can be improved by reducing the aperture size and

gap between electrodes at image side of Einzel lens and operating it at an accelerating mode in reducing spherical and chromatic aberration. The production of an 8 nm probe diameter at 1 mm working distance with a 1 keV beam energy has been reported [26]. Sainin et. al. [25] reported an achievement of 10-20 nm beam diameter, 1 nA current, and a 100 μm field of view by a microcolumn using carbon nanotube emitter at 1 keV and 50 μm thick Si lens electrode. With the modification of microcolumn structure, Large field of view is reported which presents ~40 mm × 40 mm without using any Einzel lens and ~170 mm × 170 mm by introducing a deflector between Einzel lens and sample [27] though its resolution is not satisfactory.

Fig. 1.2 demonstrates photographs of two generation of microcolumn: (a) prototype (b) improved microcolumn [28, 29]. The improved microcolumn uses field emitter tip without aid of STM, both the source and Einzel lenses are aligned separately, and assembled in a compact housing. The basic differences between them are presented in Table 1.1

Because of small in size, multicolumn can be assembled at a small area and column itself can be travelled over the sample stage rather than stage movement. This offers the multicolumn structures for high throughput, especially in e-beam lithography. Some of the arrayed microcolumn structures have been practiced such as single column module (SCM), monolithic column module (MCM), and wafer-scale column module (WCM) [12, 28, 30-34]. There is freedom of testing and operating individually in SCM, however dense packing of multicolumns is possible in MCM. WCM offers the capabilities of mass production and high

packing-density despite a challenge of individual column characterization after assembly [28].

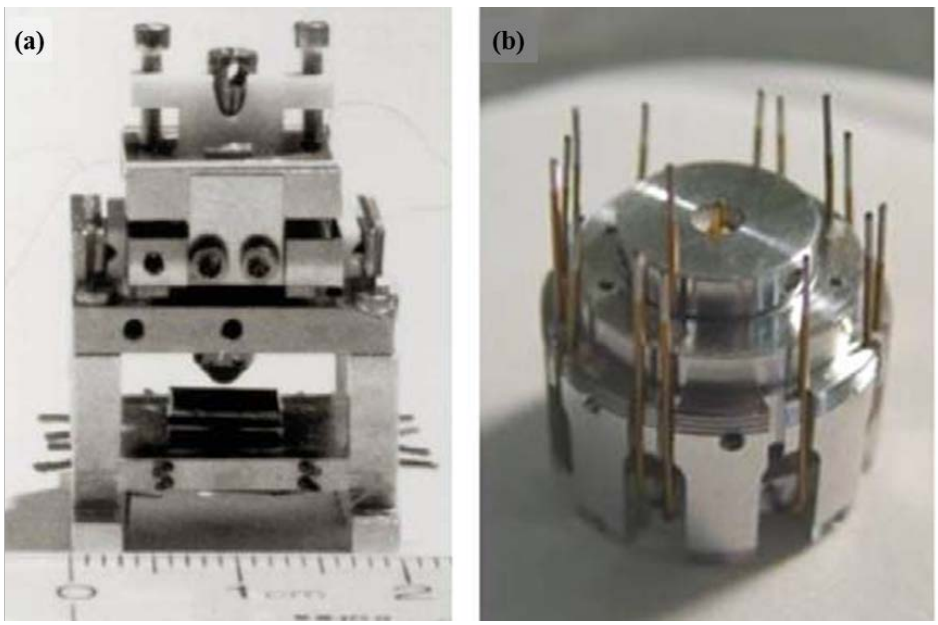


**Fig. 1.2** Photographs of two generations of microcolumn. (a) Prototype microcolumn (IBM). (b) Improved microcolumn (SMU) [28].

**Table 1.1** Differences between prototype and improved lens designs.

| | **IBM** | **SMU** |
|---|---|---|
| Size | 20 x 20 mm footprint | 20 mm circular diameter |
| Column height | ~3.5 mm | ~6.5 mm |
| Electron source | Schottky emitter (1800 K) | Cold field emitter (300 K) |
| Resolution | 10 nm imaging, 100 nm lithography | 60 nm lithography |
| Alignment method | SAFE-STM | Optical / Laser |

Several features of microcolumn including its miniaturized size, small probe size, low voltage capability, consists of only electrostatic components, simplicity in design, and feasibility of multibeam operation make it versatile applications. Some of the prominent uses are in electron microscopy, nanolithography, metrology, inspection, testing and miniature spectroscopy. An electron beam microcolumn is assembled for low voltage SEM of which the size as well as cost of microscope is reduced. The mini-SEM also can be conveniently combined with scanning tunneling microscope (STM) and atomic force microscope (AFM) [2-4, 35].

Microcolumn is quite useful for maskless nanolithography because an e-beam is precisely manipulated using the electric circuit. Moreover, the column itself is moved over the resist coated sample rather than sample because of its small size. The lithography throughput is as high as 25 wafers/hour for 100 nm lithography using 1 keV microcolumn [5, 6, 8, 36, 37].

The necessity to monitor pattern fidelity is conveniently performed with low voltage e-beam microcolumn for various purposes such as pattern-to-pattern comparison, pattern-to-data comparison, defect detection, and feature extraction [5, 13-15]. Sub-micrometer defect on circuit or patterns is inspected by low voltage secondary electron microscope imaging for surface defects and specimen current measurement for internal defects [13, 15].

Non-contact testing on semiconductor chips is done using miniaturized e-beam column, for example, short test of interconnecting nets of a packaging substrate or a flat panel display by injecting electrons by one column and detecting by another column [15, 38, 39].

Microcolumn can be converted into a miniature spectrometer by adding some extra components to provide material analysis capability. Others potential applications are in flat panel display, and high density storage system.

The interest of fabrication of a complete column-on-a-chip has still several challenges related to the material and design constraints; such as stable miniaturized electron source for collimated high dense electron emission, thin electrostatic lens for aberration-free transport of electrons, and miniaturized scanner for wide range of beam deflection. This dissertation presents a design and fabrication of an electrostatic lens for a microcolumn.

## 1.1 Electrostatic lenses: source and Einzel lenses

An electrostatic (ES) lens is an electrical device that assists in the transport of charged particles (e.g., electrons, ions, protons etc.). Analogous to optical lens, it also magnifies or converge the electron trajectories, shrink or diverge the electron beam. Utilizing the properties of ES lens in manipulating the e-beam trajectories, it has been used in various purposes such as to focus electrons emitted from cathode on a screen in cathode-ray tube (CRT) and television picture tube, to guide electrons emitted from a sample or source to an electron analyzer, and to focus the ion beam to make a microbeam for irradiating individual cells.

An endeavor to precisely control the transpose of the charged particles has been the core of research interests in the field of electron or ion beam technology [40-44]. Transpose of charged particles is mostly controlled by electron lenses

analogous to the optical lenses which refract electrons path, converting or diverging e-beam. Unlike light, e-beam not only get focused or diverged, but also accelerated/decelerated when passes through electric or magnetic fields and self-divergence due to electron-electron interactions. As charged particles (e.g., electrons) interact with both electric and magnetic field, a lens can be constructed from either of them or combination of both the fields. Although electromagnetic lens has been widely used in focusing high energy e-beam for its capability in handling high energy beam with low aberration, the magnetic lens can hardly be implemented in a microcolumn because of its bulky size and incompatibility with microfabrication technology. Whereas, electrostatic lens is milli/micro-meter size, easy to integrate, and compatible with microfabrication process and largely used at low voltage operation.

A miniaturized electrostatic lens is being used in order to control the transpose of e-beam inside the column because its size is compatible to micrometer range and can be fabricated following a robust microfabrication technology. An electrostatic lenses are constructed from a coaxially aligned multiple electrodes with insulating gaps. Electric potential is applied to specific electrodes and rests of electrodes are grounded providing electric field gradient inside the column. E-beam is transposed through the column and gets refracted according to the field gradient at the gap between electrodes. The electrostatic lens may be cylindrical, quadrupole, circular, or planar according to the geometrical shape of the lens-electrodes. The miniaturized electrostatic lens can be fabricated following well-established MEMS technology which sizes reduces to a few micrometer to several hundred micrometer; hence the size of microcolumn can

be reduced to a few millimeter size. Using appropriate insulating materials between lens-electrodes, several kilo-volt can be applied.

The performance of a microcolumn is severely affected by the electron optical lenses which are composed of coaxially aligned electrodes separated by an insulating material. It plays the role of guiding an electron beam with an appropriate energy and size. Electrostatic lenses are generally made of heavily doped Si membranes separated by electrically insulating spacers and the performance of both source and Einzel lenses depend on the geometric completeness.

Electrostatic lens is fabricated either by bond-then-drill or drill-then-bond technology. For any case, electrodes should be geometrically well-defined and coaxially well-aligned. Bond-then-drill method follows the processes of stacking of electrodes separated by Pyrex then drill right through the multilayer structures. Several drilling technologies have been employed such as UV-laser drilling [45, 46], wet and dry etching, deep RIE, LIGA, FIB, and ultrasound vibration drilling. The major disadvantages of this method are tapering effect and non-uniform cylindrical shape.

Drill-then-bond method first fabricates individual lenses with cylindrical hole through electrodes. Electrodes are normally fabricated from silicon wafers following sequences of MEMS processes: photolithography, RIE, wet etching etc. Multiple electrodes are aligned with spacing between them with insulators using optical microscope or laser diffraction method. The major challenge of this method is accurate axial alignment of three electrodes. Even sub-micron misalignment between electrodes produces significant aberration and distortion.

To mitigate the misalignment problem, I here present thin electrostatic lenses fabricated by conventional MEMS techniques in this research [47].

There are several issues to be addressed in fabricating microlenses such as perfectly round hole ($\Delta r/r < 0.1\%$) (roughness < 5 nm), perfect alignment (<1%), and well bonding [2, 17, 26]. Of important, the MEMS technique such as photolithography and deep Si etching technique enable in making such a round hole within the technical limitations of processes. The laser alignment technique is applicable in aligning the lenses with the accuracy of a few micrometers. Anodic bonding, an electrochemical bonding at over 200 $^{o}$C and 200 V does make bonding well.

The microfabrication technique has been employed in making electrostatic lenses for microcolumn because the size can be miniaturized down to micrometer. However, there are several technical challenges in fabrication of suitable lenses such as controlling the desire thickness of lens electrode and insulators, making geometrically perfect apertures, and aligning the electrodes with sub-micrometer accuracy. I performed several experiments in fabricating controllable thickness of lens electrode from a few to several hundred micrometers. The flexible thickness was used in studying the effects of gaps in lens structure on the performance of microcolumn. The finding of effects of variation in electrodes gap is presented in this dissertation.

## 1.2 Research purpose

The first lens model studied in this research has multiple lens-electrodes aligned through the apertures along the optical axis separated by Pyrex. The lens-

electrode was made of a Si membrane with a circular aperture at its center and the membrane is mechanically supported by bulk Si. The fabrication process is relatively easy and the lens-electrode is mechanically robust though the membrane thickness is only a few micrometers because of supporting bulk Si [48-50]. But the non-etched bulk Si is a matter of restrictions in several cases. For example, the geometrical structures restrict us in constructing the electrostatic lenses with flexible gaps between electrodes. It cannot be reduced down the gap between lens-apertures below to the wafer thickness. The thick Si further hurdles in alignment of electrodes and provides unnecessary longer path for electron beam. It increases aberration and distortion of beam due to interference on electric field produced by Si wall.

To overcome the restrictions due to bulk Si, another electrostatic lens has been investigated in this research. For the flexible lens electrode thickness and gap between electrodes, a lens-electrode structure was modified, fabricated and its performance has been evaluated. Chapter II presents design of both electrostatic lens models. In the second model, a large area (~10 mm × 10 mm) thin (~ a few micrometer) Si membrane bonded with Pyrex acts as a lens-electrode which does not have any unnecessary bulk Si unlike in the first model. It demonstrates some notable features like flexible thickness (a few micrometers to several tens of micrometers) of Si membrane, flexible thickness of insulating materials (Pyrex can be a few tens of micrometer to several hundreds of micrometer). To comprehend the electrical properties of electrostatic lens system, a computer simulation was performed implementing a finite element analysis method for solving partial differential equations related to electric

potential/field. The simulation results indicates that the electric potential/field distribution in electrostatic lens structure depends upon the geometrical structures of lens. For example, the variation of electric potential along the axis is higher when the electrodes separation is lowered.

Chapter III presents design of photomasks based on cadence drawing, successful fabrication techniques of lens electrodes, its alignments and bonding, and microcolumn assembly. It discusses fabrication of electrostatic lenses following the MEMS fabrication processes such as boron doping, oxidation, photolithography, deep Si etching, wet etching process, and anodic bonding techniques. The multiple lens electrodes were aligned and bonded following the laser diffraction technique which accuracy was measured by transmission optical microscopy. Finally, assembly of emitters, source lens, deflectors, Einzel lens, and sample (or detector) are discussed.

Chapter IV presents various modes of microcolumn operation for the characterizations of lens fabricated. It discusses in one-lens and two-lenses focusing modes. In these modes of operation, surface imaging techniques are elaborated.

One of the prominent issues of microcolumn is field of view (FOV) which is of inadequately small range as compared to its counterparts. Chapter V discusses the influence of Einzel lens structures on FOV variation. There are still several technical challenges in achieving larger field of view with better resolution. Experimental and simulation results are presented for analysis of scan ranges with the modification of Einzel lens structures.

The conclusions are design and successful fabrication of an electrostatic lens (source and Einzel lens) which includes several features like flexible gap between electrodes, flexible lens thickness, and applicable to high voltage using thick insulator without increase in overall lens thickness. The performance of the fabricated electrostatic lens was carried out in order to study scan range variation with the changes in Einzel lens structure. The experimental and simulation results shows that scan range increases with reducing gap between lens-apertures in one-lens focusing mode but the trend is reverse in two-lens focusing mode. The results indicate the necessity of adjustment of gap between the lens electrodes for the wider FOV and better resolution.

# 2 CHAPTER II: DESIGN AND SIMULATION OF EINZEL LENS MODELS

Einzel lens is an objective lens which primary function is to focus e-beam without altering energy of e-beam. It is usually composed of three co-axially aligned circular apertures through which e-beam passes and its trajectories are guided by electric or magnetic force produced by corresponding field applied on lens system. According to nature of field used in Einzel lens system, the lens is called electrostatic or magnetic lens. Electrostatic lens is used in microcolumn because of its miniaturized size and simplicity in design.

The performance of microcolumn is predominantly affected by the electron optical lenses which are normally electrostatic in the nature of field. The ideal electrostatic lens is supposed to have very smooth and geometrically well-defined apertures, and the possibly accurate aligned along an optical axis passing through center of aperture. Modern day's column comprises two lens systems: a source lens and an objective or Einzel lens. Although, both of lenses are similar in nature of construction except some variation in aperture sizes, gaps between electrodes, and number of lens-electrodes. Source lens may have single or multiple lens-electrodes. In the case of three lens electrodes, the first lens-electrode extracts electron from tip and second electrode accelerates it and third electrode controls the beam waist.

Objective lens is usually constructed with three identical lens-electrodes aligned along an optical axis with rotational symmetry. In normal operation, the middle electrode is biased either negatively or positively with respect to inner

and outer grounded electrodes. As both the inner and outer electrodes are biased with same potential, hence the lens system is also known as an equipotential lens or an Einzel lens because it does not alter the e-beam energy passing through it.

The simplest example of an electrostatic lens consists of a circular conducting electrode (disk or tube) which is normally negatively biased. An electron passing along the optical axis experiences equally radial inward forces from all points of electrode and therefore, suffers no deflection, whereas off-axis electrons are forced toward the axis. A practical form of an electrostatic lens uses three coaxially aligned circular conducting electrodes in parallel so that the electric field produced by the central electrode is limited to localized region. This kind of lens is known as a unipotential or Einzel lens because electrons that enter and leave through it do not alter its energy.

## 2.1 Principle of electrostatic lens

Let an electron with charge e mass m, moving with velocity **v** projected at an angle $\theta$ to x-axis into a uniform electric field **E**. If the potential of the lower plate, y = 0, is $V_0$, then the initial velocity and the trajectory of the electron is given as [51] (The derivation is presented in Appendix 1A.1.1):

$$v_0 = \sqrt{-2eV_0/m} \qquad 2.1$$

and

$$y = \frac{e}{2m} E t^2 + v_0 t \sin\theta \qquad 2.2$$

The region between any two equipotential $V_n$ and $V_{n+1}$ is approximated by the constant average potential

$$\bar{V}_n = {}^1\!/_2\,(V_n + V_{n+1}) \qquad 2.3$$

The electron, moving in this stepwise approximation to the real potential, follows straight-line paths between equipotential, but it is subject to an impulsive force at each boundary where the potential is assumed to be changed. This force is normal to the boundary thus leaving the momentum parallel to the boundary unaffected. Equating the tangential components of velocity we obtain

$$v_n \sin\theta_n = v_{n+1} \sin\theta_{n+1} \qquad 2.4$$

Combining equations 2.1 and 2.4 leads to

$$\frac{\sin\theta_{n-1}}{\sin\theta_n} = \sqrt{\frac{\bar{V}_n}{\bar{V}_{n-1}}} = \sqrt{\frac{V_{n+1} + V_n}{V_n + V_{n-1}}} \qquad 2.5$$

The equation 2.5 is analogous to Snell's law for the refraction of a light ray as it passes from one medium to another. It is seen that the quantity analogous to the optical index of refraction is √V or simply electron velocity. A bundle of electron paths passing through a common point near the axis of an axially symmetric field system can be made to pass through another common point by a relatively limited region of field variation. The first common point is appropriate to call the object and the second point is the image. Imperfections in this process are naturally called aberrations.

Unlike light lens, the electron lens is not confined by well-delineated boundaries, but consists of a more or less indefinite region in which the potential distribution must be an appropriate solution of Laplace's equation.

The derivation of focal length for thin electrostatic lens is found elsewhere [51] and the re-derived in Appendix A:. The focal length is a function of potential on the lens and given as:

$$\frac{f_2}{f_1} = -\sqrt{\frac{V_2}{V_1}} \qquad 2.6$$

Which is analogous to the corresponding law in light optics for a lens between two different media. If $f_2$ is positive, then $f_1$ is negative, but both conditions imply convergence. Thus the diverging or converging action of the lens works both ways. The sign of lens depends on the sign of "$V_0$" which determines the integral, since all other factors are positive. Thus, wherever the axial potential curves concavely upward, it is a converging region, and wherever it curves concavely downward, it is diverging.

## 2.2 Einzel lens model

There are numerous models of electrostatic lenses in practice depending upon necessity and usefulness. Most popular types are double-cylinder accelerating or retarding lens and the triple cylinder unipotential lens. Both of them are rotational symmetric along the optical axis having circular aperture at center for electron passage. A simplest model of typical unipotential lens is illustrated in Fig. 2.1. In this example three rotation-symmetric coaxial electrodes composed of either cylinder or disc are arranged along the optical axis. The primary function of outer electrodes is to limit the extension of electric field applied on

the central electrode. The power of lens is determined by the potential difference between center and outer electrodes as described in section 2.1.

Fig. 2.1 illustrates a schematic of a typical Einzel lens system which is consists of a set of three identical symmetric electrodes. It is an example of typical equipotential lens made of identical lens electrodes. As its name, the outer electrodes are kept with equal potentials (grounded in normal operation) which provides equal and opposite axial electric field components. If left part of central lens exerts converging force on electrons at center then the right part exerts diverging force to the electron beam passing through the lens system. Because of these equal and opposite forces, the electrons are forced to go through the axial line and focused somewhere at the axial line.

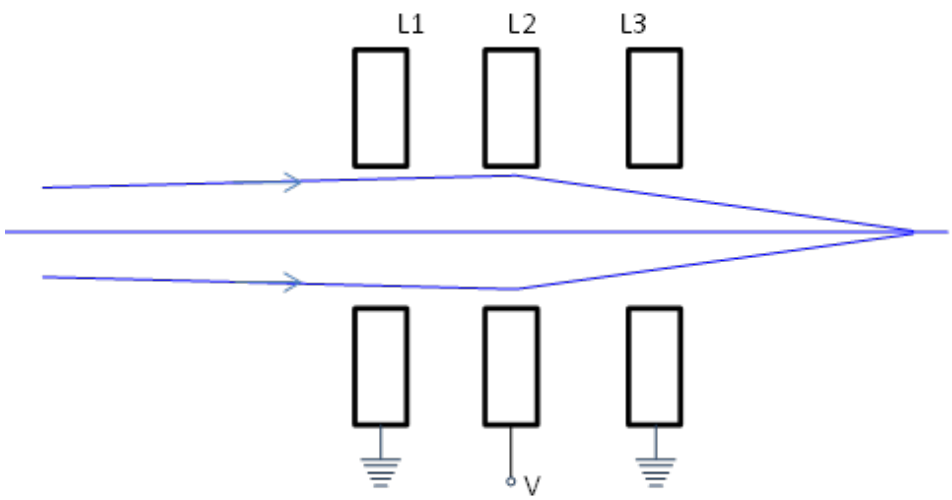


**Fig. 2.1** The simplest electrostatic lens model. Three circular electrodes L1, L2, and L3 are spaced by insulators. In normal operation, central electrode is normally negatively (or positively) biased whereas outer electrodes are grounded.

Fig. 2.2 shows a schematic of our first electrostatic lens model. The lens is composed of three heavily doped Si electrodes supported by bulk Si and separated by electrically thick-Pyrex (Fig. 2.2 (a)).

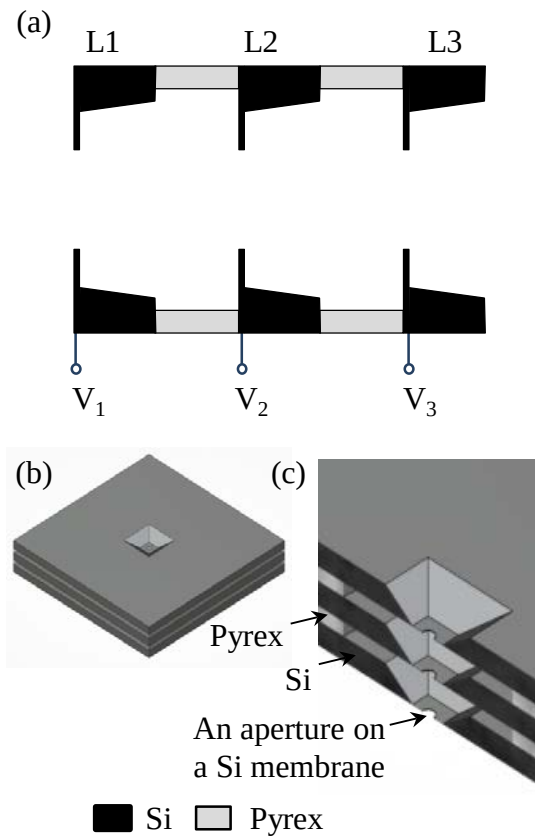


**Fig. 2.2** An electrostatic lens design of which Si membrane is supported by bulk Si and separated by Pyrex. (a) Schematic representation of the lens structure. Solid black block is Si substrate used as an electrode and gray block is Pyrex used as an insulator between electrodes. (b) Schematic top view of the model. The typical dimension is 8×8×1.5 mm. (c) Cross section view of the aperture on membrane region. Pyrex ~200 μm, Si membrane ~ 1 μm, Bulk Si ~350 μm. It has limit in miniaturization of the lens structure.

The center of electrodes has micron size circular aperture on thin Si membrane for electrons passage. The size of aperture has been selected from a few micrometers to several hundred micrometers depending on purpose of its use. The membrane thickness may be as thin as 1 μm to a few tens of micrometers. The thickness of bulk Si is equal to wafer thickness (~350 μm). 3D schematic and a cross section views are shown in Fig. 2.2 (b) and (c). Note that the inclined Si wall of window is fallouts of anisotropic wet Si etching which makes ~54$^{o}$ to the surface. The fabrication of such design is explained in elsewhere [49]. The major drawbacks of this model are limitation of gap between lens electrodes that cannot be reduced down below wafer thickness, field disturbance due to bulk Si, and thick lens structure.

To overcome the limitations of our first lens structure, the second lens model has been designed as illustrated in Fig. 2.3. The major structural modification in this model is the exclusion of bulk Si. The mechanical support for the membrane is provided by the insulating Pyrex itself. This single structural modification brings several functional advances: the electrodes are separated purely by insulating materials (Pyrex), the gap between electrodes only depend upon the Pyrex thickness, the miniaturization of gap is no more restricted by thickness of bulk Si, the gap can be well-adjusted depending upon the utilities of the lens system, high voltage can be applied to electrode because of high breaking voltage of Pyrex, and overall thickness of lens structure can be down to sub millimeter. A schematic and cross section views of modified lens design are illustrated in Fig. 2.3 (b) and (c). The dimension of the modified lens structure then reduces to 8×8×0.6 mm for selected Pyrex thickness 200 μm.

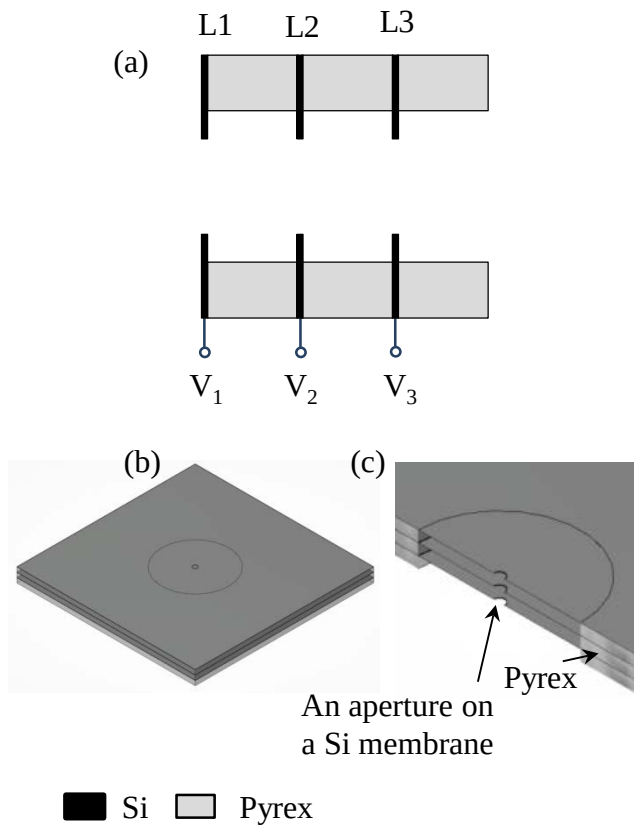


**Fig. 2.3** Another electrostatic lens design of which Si membrane is supported by Pyrex. (a) Schematic representation of the lens structure. Solid black block is Si substrate used as an electrode and gray block is Pyrex used as an insulator between electrodes. (b) Schematic top view of the model. The typical dimension is 8×8×0.6 mm (c) 3D cross section view of the aperture on membrane region. Pyrex ~200 μm, Si membrane ~ 10 μm. The Si membrane is supported by Pyrex rather than bulk Si substrate. The miniaturization of lens structure is possibly down to a few hundred micrometers.

The second design can be used as a source lens as well as an Einzel lens. For instance, the aperture sizes 50, 100, and 10 μm diameters can be implemented with either uniform or different gaps between electrodes in a source lens system. An identical lens electrodes with uniform aperture size (e.g., 200 μm) and

different gaps between the electrodes are designed for an Einzel lens structure. The effects of gap between lens-electrodes in Einzel lens structure in the scan range is analyzed in this thesis.

**Features of second lens model**

- A flexible lens-electrode thickness (a few micrometers to several tens of micrometers) is assured.
- A flexible gap between lens-electrodes as the gap is determined by the thickness of Pyrex is realized.
- Overall thickness of lens structure is maintained as small as a few hundred micrometers to several hundred micrometers providing freedom of choice.
- Standard microfabrication procedures can be exploited and batch fabrication is possible.
- The miniaturization of electrostatic lens structure is realized.
- Multiple lens electrodes can be directly aligned and staged.
- High voltages can be applied without increasing the gap between lens-electrode because of high breaking voltage capability of Pyrex.
- The electrostatic lens system can be used in constructing e-beam microcolumn with both source and objective lens system.
- This electrostatic lens could be applicable of various e-beam apparatus, for example, electron beam lithography, low voltage SEM, and high-resolution SEM with the combination of electromagnetic lenses.

The comparison between two lens models is presented in Table 2.1. The table shows that both types of model are similar in many ways except geometrical shape of the electrodes. This slight changes in geometry give high freedom in selecting the gap between electrodes and several functional advancements. How the geometrical shape affects in electric potential/field distribution inside the lens system is discussed in chapter IV with the computer simulation data.

**Table 2.1** Comparison between two types of lens models.

| | **Si supported Si membrane lens** | **Pyrex supported Si membrane lens** |
|---|---|---|
| Electrode | Si membrane | Si membrane |
| Aperture on | Si membrane | Si membrane |
| Miniaturization | Limited by Si and Pyrex thickness | Only limited by Pyrex thickness |
| Mechanical support for membrane | Bulk Si | Pyrex |
| Gap flexibility | Limited by bulk Si and Pyrex | Limited by Pyrex |

## 2.3 Simulation of electric potential/field distribution for 2D Einzel lens module

With the development of computer simulation tools, the understanding on electrostatic lens approaches to very specific and definite. The simulation tools has been used for various purposes of interests including designing an electrostatic lens module, calculating the physics of lens structure, calculating the electric filed/potential variations, tracking electron or charged particles inside the lens system, interrelation/interaction with other electrical components etc. [20, 43, 47, 52-55]. This chapter presents a simulation of an electrostatic

lens structures in the COMSOL Multiphysics software [56]. COMSOL is finite element analysis method software which calculates the physics of a module by solving partial differential equations. Among the various modules of physics available in this software here AC/DC module [56] was used. Both the two Einzel lenses design presented in chapter II are used for 2D simulation of electric potential and field distribution inside the lens system (Fig. 2.4).

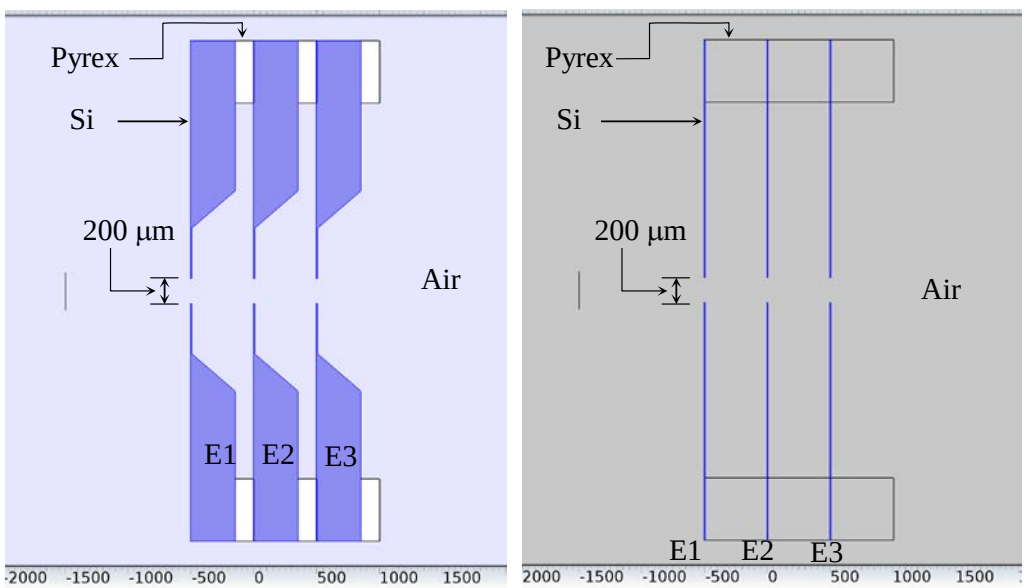


(a) Si supported lens-electrode model (b) Pyrex supported lens-electrode model

**Fig. 2.4** An Einzel lens modules designed for simulation of electric potential and field. (a) Si supported lens-electrode model. (b) Pyrex supported lens-electrode model. Both the designs are identical except the geometrical shape and membrane supporting materials.

Si and Pyrex are used as an electrode and an insulator and air/vacuum for surrounding environment. The Si membrane of thickness 10 μm is used as a lens-electrode with an aperture 200 μm. The gaps between lens electrodes are set 500 μm for both models however bulk Si and Pyrex are used as a mechanical

supporter for the Si membrane in the first (Fig. 2.4 (a)) and second (Fig. 2.4 (b)) models, respectively. The width of electrodes for both designs is 4 mm with 200 μm aperture at its center. Pyrex having circular aperture of 3 mm in diameter is used. Total simulation area is a rectangle of size 5 mm × 8 mm.

### 2.3.1 Simulation method

AC/DC model of COMSOL 4.3 multiphysics simulation environment is used for calculating electric field and potential. Two properties of material are essential: (a) relative permittivity (11.7 and 2.09 for Si and Pyrex), (b) electrical conductivity ($1\times10^{5}$ and $1\times10^{-24}$ S/m for Si and Pyrex) for simulation. Other properties are as follows:

1. Equations: $\nabla \cdot (\epsilon_0 \epsilon_r E) = \rho_v \; and \; E = -\nabla V$ were used to relate electric field E, potential (V), and volume charge density ($\rho_v$) in electrostatic section.
2. Charge conservation, zero initial charge, and zero initial potential were set by default for all the domains and boundaries.
3. All the boundaries were grounded except the middle electrode of lens structure.
4. The middle electrode (E2) was applied potential of -500 to 500 V in 100 V intervals.
5. The meshing of the model is done by predefined extremely fine for general physics which is free triangle in shape with maximum and minimum element size 80 and 0.16 μm, respectively (Fig. 2.5).

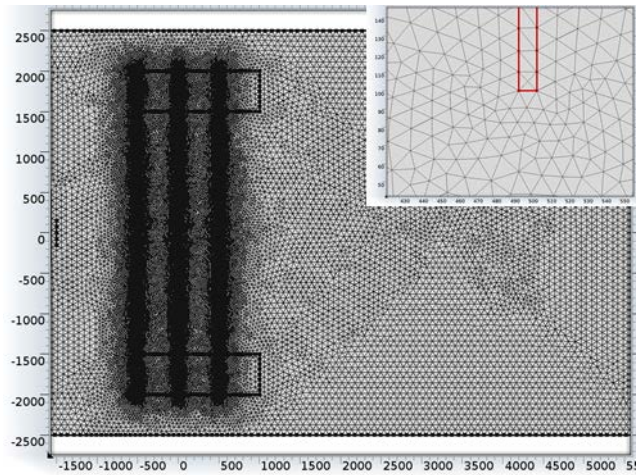


**Fig. 2.5** The mesh pattern of the model. Magnified view of an edge of the electrode (Inset).

### 2.3.2 Simulation results

Electric potential distributions with contour plot on the surface is shown in Fig. 2.6. The rainbow color shows variation of electric potential with ascending form blue (0 V) to red (500 V) and contour plot represents equipotential curves at 15 V intervals. Fig. 2.6 (a) illustrates surface plot of electric potential distribution. Fig. 2.6 (b) and (c) are the magnified pictures of the region at the central electrode showing contour plots of equipotential curves. The contour plots are with the interval of 15 V. The equipotential lines appear almost straight at the aperture side. Importantly, the equipotential curves obtrude at the apertures of both grounded electrodes. In both types, the potential is higher at the electrode side and gradually decreases moving out from electrode.

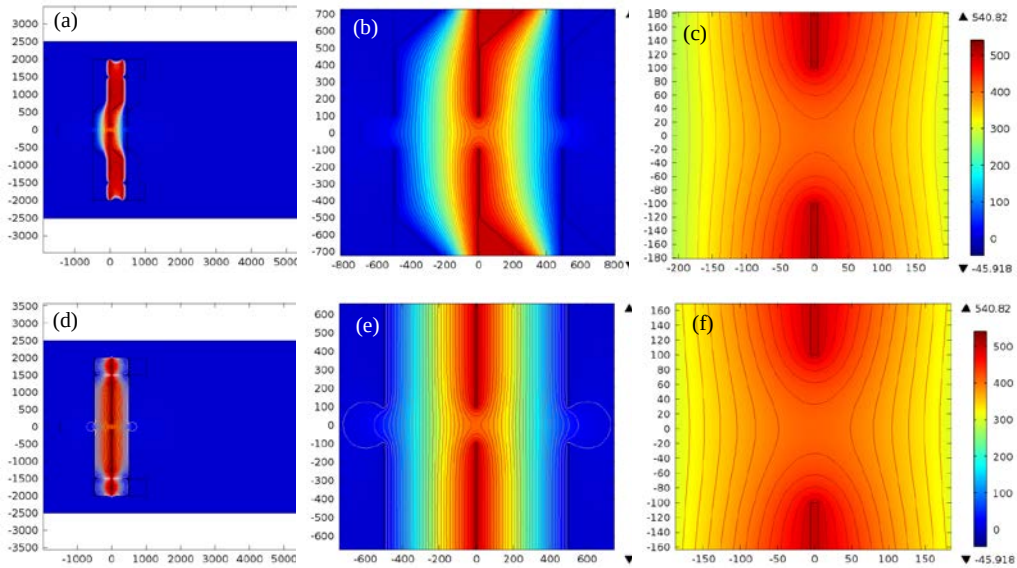


**Fig. 2.6** Electric potential distributions on surface of electrostatic lens system. (a-c) Distribution due to Si supported lens-electrode. (a) Entire area. (b) Magnified at the center of lens system. (c) Magnified image of the central aperture. (d-f) Distribution due to Pyrex supported lens-electrode. (d) Entire area. (e) Magnified at the center of lens system. (f) Magnified image of the central aperture region. The rainbow color from blue to red represents lower to higher electric potential. The counter plot represents equipotential lines with interval of 15 V.

Line plots along an optical axis for electric potential and field variation are shown in Fig. 2.7. The plots for both the models are appeared identical, so only one plot is presented in the figures. The identical nature of potential/field distribution indicate that the potential variation along the optical axis is not affected by the geometry of supporting structure. Fig. 2.7 (a) is electric potential variation along the x-axis passing through center of the aperture when E2 is biased with 0-500 V. The curves are appeared as Gaussian distribution curve showing the uniform variation of potential from the mid-electrodes outward to the two grounded electrodes. The potential gradually increases from near to the

aperture at first electrode and reaches an extreme potential at center of middle electrode, however, the peak value is nearly 82% of the applied potential.

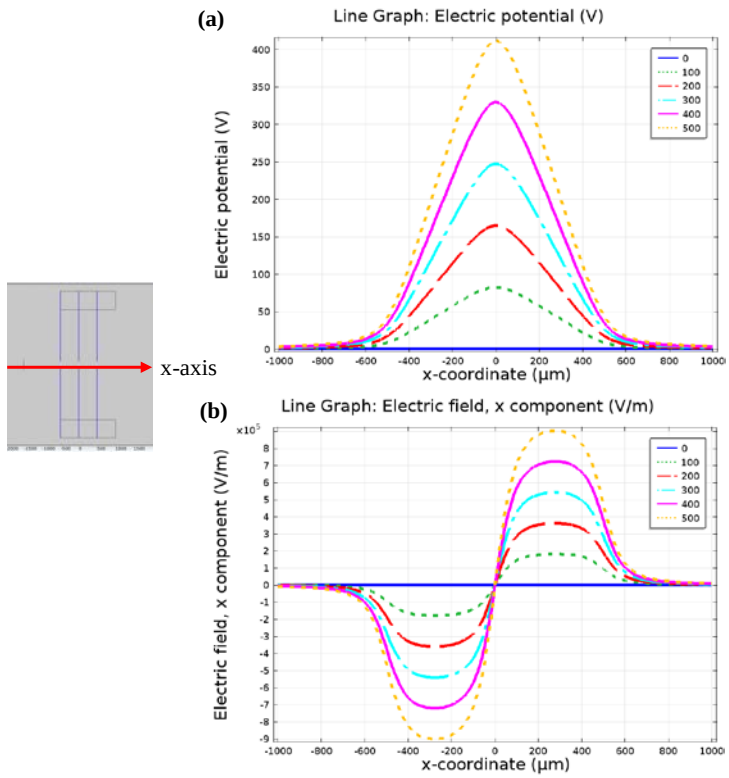


**Fig. 2.7** Electric potential and field distribution along an optical axis. (a) Electric potential and (b) Electric field, x component variation for E2 voltages 0-500 V.

In similar to electric potential curve, the electric field distribution along the optical axis is also identical as illustrated in Fig. 2.7 (b). The electric field gradually increases from near to the first aperture and reaches two extreme positions at left and right side of the middle electrode. The peak value lies nearly mid of two electrodes which is equal to $1.83\times10^{-5}$ V/m for 100 V and it increases with increase in potential with same fold change.

The electric potential distributions along perpendicular to the optical axis on the surface of E2 and middle line between two electrodes are plot as indicated in Fig. 2.8 (a) for both models. The results are identical as presented in Fig. 2.8 (b) along the E2. The electric potential sags down at the aperture region and reaches minimum value at the center of aperture which is approximately 82% of the surface potential. Interestingly, the electric potential distributions through middle of Pyrex are quite different for those two lens structures. Fig. 2.8 (c) and (d) illustrate the line plot along the perpendicular to the optical axis at the middle of two electrodes. The potential distribution appeared up and down for the Si supported lens structure where the potential goes up at Pyrex region but lower down at the air. But in the case of thin lens structure, the potential remains almost at the higher value at the aperture region though its less than half of the applied potential at the middle electrode of the Pyrex supported structure. This variation of potential at the insulator zone may contribute in focusing nature of the electron beam.

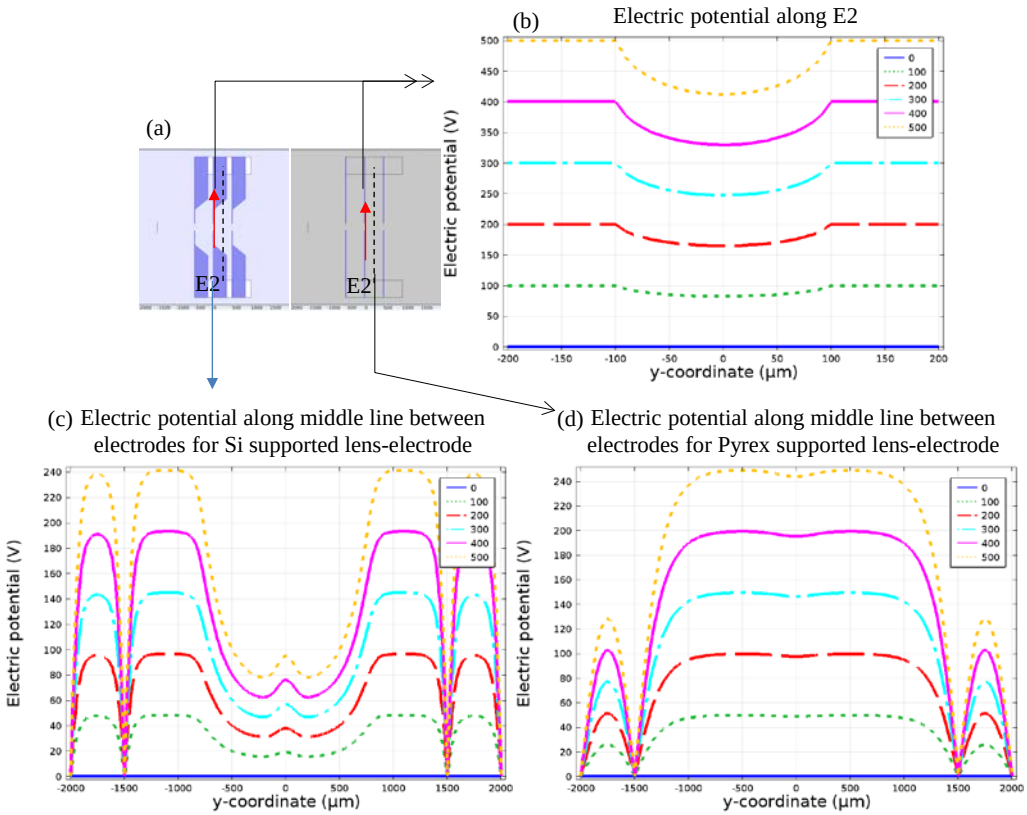


**Fig. 2.8** Electric potential distribution along y-axis on E2 and middle line between two electrodes. (a) Solid red line with arrow and broken black lines indicate the line and direction of plot for both model. (b) Electric potential along the E2 line for both models. Electric potential along middle line between two electrodes for (c) Si supported and (d) Pyrex supported lens-electrode.

## 2.4 Effect of gap between lens-electrode in electric potential/field distribution

An electrostatic lens model was designed with three circular Si discs with 200 μm apertures coaxially aligned along an optical axis inside a cylindrical air environment (Fig. 2.9 (a)). Tetrahedral meshes were created with maximum and minimum element sizes of 1 and 0.1 μm for lens structures and 30 and 0.3 μm

for rest of the domains (Fig. 2.9 (b)). Fig. 2.9 (c) presents a zoomed picture of mesh structures at the lens electrode region. The middle electrode was applied with electric potential whereas two outer electrodes were grounded so that the structure worked as a standard equipotential lens.

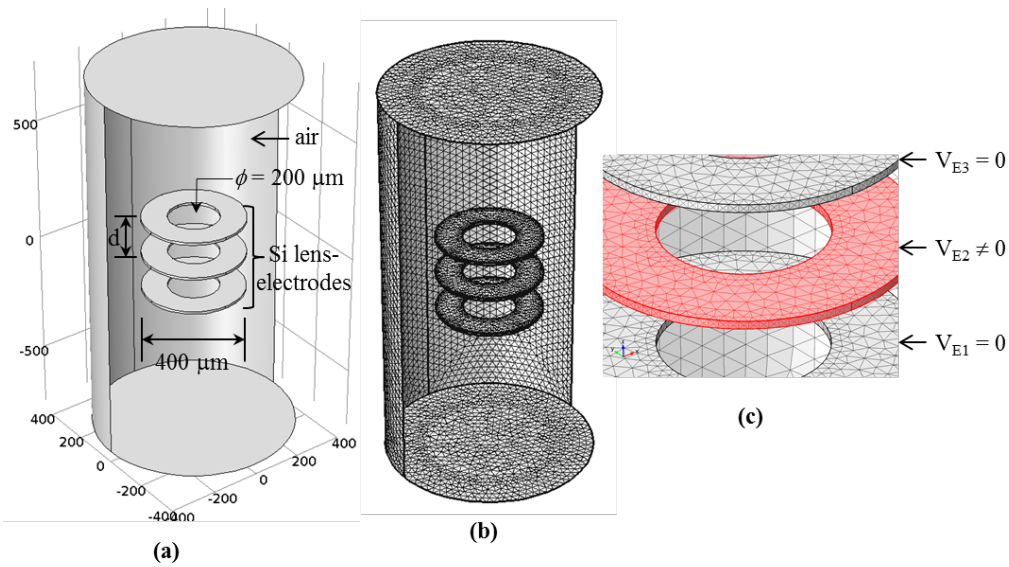


**Fig. 2.9** An electrostatic lens module and tetrahedral meshes for electric potential and field simulation. (a) Geometry of module. (b) Tetrahedral meshes for all domains. (c) Magnified picture of meshes at lens-electrodes showing unipotential lens.

Electrostatics (es) AC/DC module of COMSOL 4.3 was used to calculate the electric potential distribution as described in section 5.1.1. An electric potential of 100 V was applied to all the boundaries of E2 domain and rest of the domains were grounded.

To analyze the effect of gap between lens-electrodes, the distance (d) between them were swept from 100 to 500 µm in 100 µm step. Fig. 2.10 presents surface plots of electric potential distribution for distance 100 and 500 µm. The rainbow

color from blue to red shows low to high voltage regions with minimum 0 and maximum 100 V. Fig. 2.10 (a) shows a multi-slice surface plot of electric potential distribution at all the three electrode planes for electrode distance 100 μm. The red color at center electrode illustrates maximum potential but lower potential at the aperture region. Outer electrodes illustrate electric potential distribution opposite of the center electrode showing minimum potential at electrode region but higher at the aperture region.

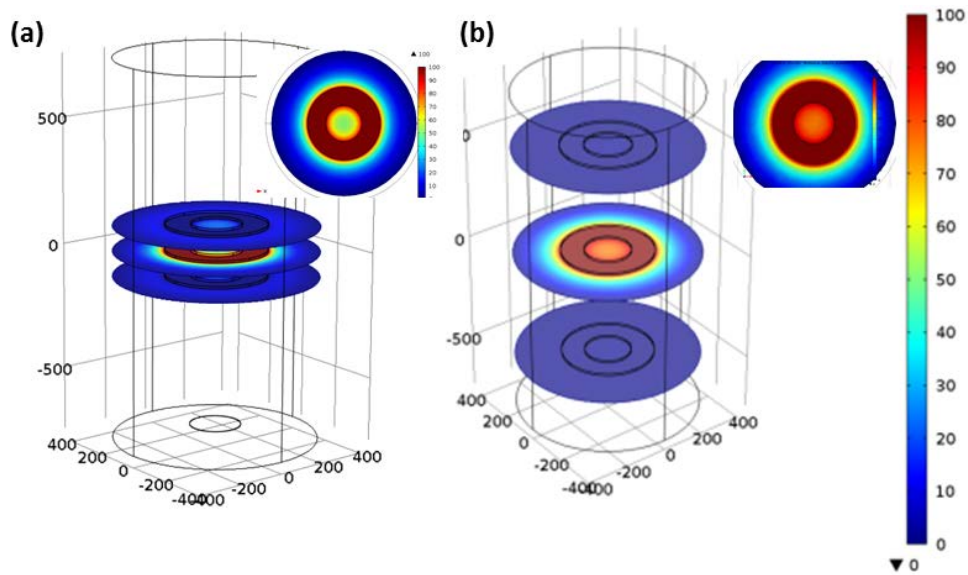


**Fig. 2.10** Surface plots of electric potential distribution at an electrostatic lens system for 100 and 500 μm spatial distance between electrodes. Surface plots at the plane of electrodes of potential distribution for (a) d = 100 μm, (b) d = 500 μm. Top view of surface plot at central electrode, E2, when d = 100 and 500 μm are shown in insets.

The nature of potential distribution is similar for electrode separation (d = 500 μm) but difference in its intensity as illustrate in Fig. 2.10 (b). A top view of electric potential distribution at the center electrode for separation 100 and 500 μm are shown in insets. It shows the highest potential at the electrode and

decreasing potential at the aperture region making minimum potential at center of aperture. The outer circular blue region shows the grounded boundary with gradual potential increase towards the electrode. The plot shows that the potential gradually decreases outward from the central electrode and reaches zero at the grounded boundaries. From the potential variation as presented in surface plots, it can be attributed that when an electron or charged particle travel through this sort of environment, the electron or charged particle is forced to pass through the center of aperture because of minimum potential at that region.

Line plots of electric potential and electric field along an axis passing through center of apertures of lens-electrodes for d = 100 to 500 μm with 100 μm interval are shown in Fig. 2.11 (a) and (b). The plot shows the uniform variation of electric potential which begins from far distance of outer first electrode and reaches maximum at the central electrode and decreases symmetrically till it vanishes. However, the maximum potentials are 50 to 75 % of applied potential at the central electrode depending upon the distance between the electrodes (Fig. 2.11 (a)). The plot depicts that the peak value is lowest for the 100 μm and highest for the 500 μm indicating sharp variation of potential for lower distance between electrodes. Similar to potential distribution, z component of electric field intensity along the axis passes through center of apertures has been plotted in Fig. 2.11 (b). The plot shows electric field intensity also increases towards the central electrodes and reaches a peak at positive or negative direction near to the central electrode. The peak value is highest for lowest gap between electrodes which shows the sharp electrical field variation for lower gap.

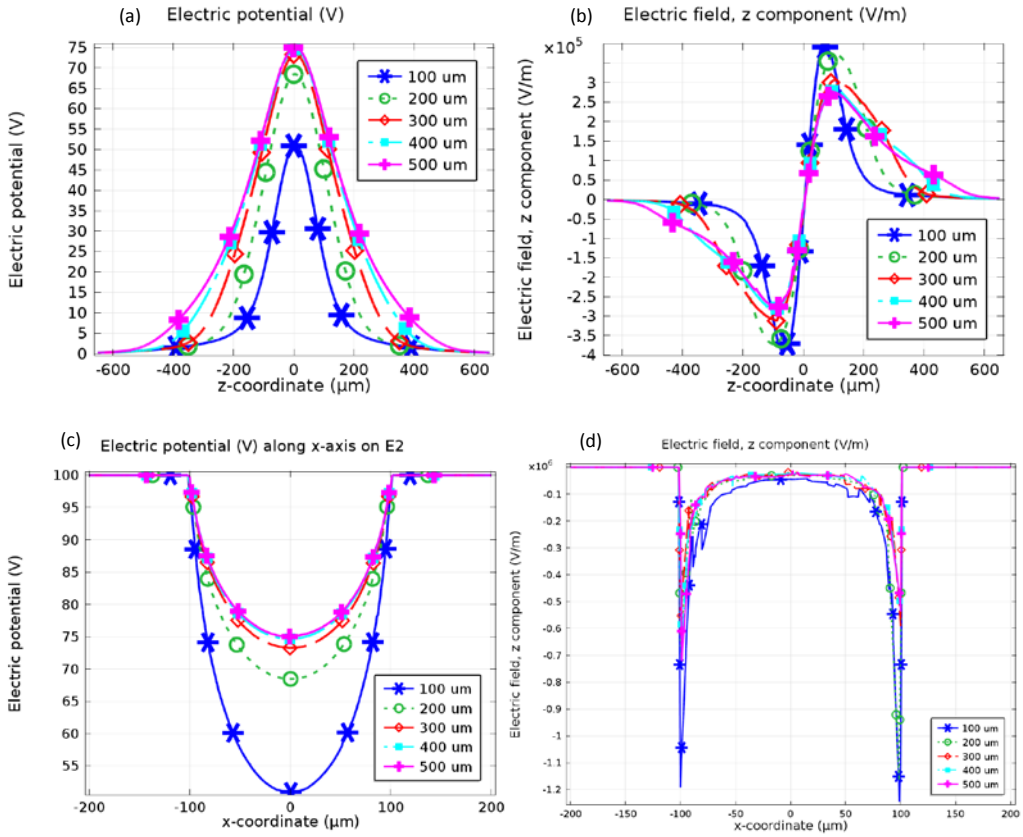


**Fig. 2.11** Line plots of electric potential and field along and perpendicular to the axis passing through the apertures. (a) Electric potential distribution along an axis. (b) z component of electric field along the optical axis.

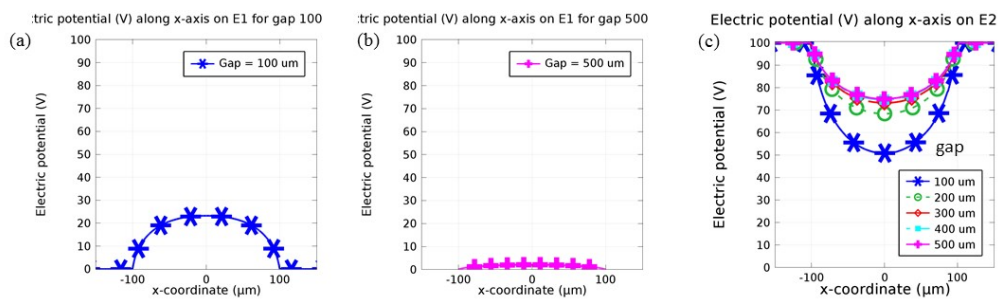


**Fig. 2.12** Line plots of electric potential along x-axis on the plane of electrodes. On E1 plane for gap between electrodes (a) 100 μm and (b) 500 μm. (c) On E2 for gap between electrodes 100 – 500 μm.

Fig. 2.11 (c) and (d) illustrate a line plot of electric potential and electric field on the central electrode along perpendicular to the axis passing through its center. The first plot shows the decrease in electric potential after the edges of electrode and reaches minimum value at its center. The minimum value is lowest for the 100-μm gap between electrodes which is just 50% of the applied potential on the central electrode whereas it is 75% for d = 500 μm. Fig. 2.11 (d) shows the electric field strength is highest at edges of the aperture and sharply diminishes to lowest level at the center of aperture. It indicates that an electron or charged particle near to edges of aperture get strong electric force radially inwards and forced to pass through the center of aperture where minimum electric field strength is located.

In contrary to central electrode, the electric potential distribution on the plane of outer electrodes along a perpendicular line to the axis passing through apertures, the potential increases towards the center of aperture as presented in Fig. 2.12 (a) and (b) for d = 100 and 500 μm. Surface plots of electric potential distribution on the plane of outer electrode are also shown in insets. The color difference for the d = 100 μm is noticeable but it is undistinguishable for d = 500 μm (Fig. 2.10). It implies an interesting nature of potential variation dependency on the separation between lens-electrodes. From the plot, it can be referred that the peak values of electric potential at the center of outer aperture are largely difference despite the similar nature of curve (Fig. 2.12). The peak value for d = 100 μm is ~24 V but it is only 2.2 V for d = 500 μm. It implies that when the distance is 5 times increased the electric potential decreases by more than 10 times at the center of aperture of the outer electrodes.

## 2.5 Simulation of electron beam trajectories for various gap between Einzel lens-electrodes in one-lens focusing mode

A microcolumn module was designed in Opera simulation environment [57] as shown in Fig. 2.13 to simulate the electron beam trajectories for various gap between Einzel lens-electrodes. Three configurations of microcolumn with varying gap between Einzel lens-electrodes are presented. The gaps are 150 μm (Fig. 2.13 (a)), 250 μm (Fig. 2.13 (b)), and 500 μm (Fig. 2.13 (c)). The aperture sizes and position of source lenses are 50 μm (S1), 100 μm (S2), and 20 μm (S3) at 100, 320, and 540 μm from tip, respectively. The Einzel lens is consists for three identical electrodes with aperture 200 μm in diameter. Deflector and sample grid are positioned at 1200 and 4200 μm from the end of the tip. The electrode thickness of source and Einzel lens are 20 um and 2 um, respectively. The tip voltage is set to -300 V for all the calculation which emits e-beam with velocity ~ $1 \times 10^7$ m/s along the S1.

Fig. 2.14 displays electron beam trajectories in a column with Einzel lens of 150-, 250-, and 500 μm gap between electrodes. The positions of source and Einzel lens-electrodes are shown by broken black lines and solid blue lines, respectively. The position of deflector with its biasing voltage is shown by red solid line.

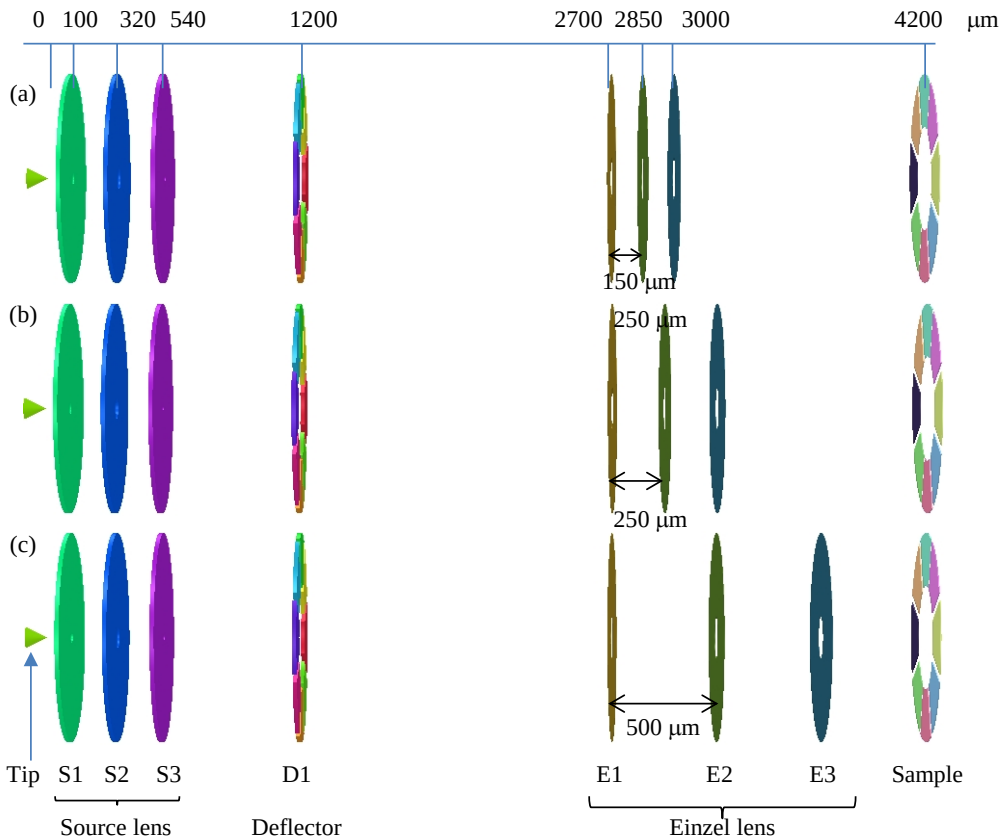


**Fig. 2.13** Microcolumn modules to simulate e-beam trajectories for various gap between Einzel lens-electrodes. Gap between Einzel lens-electrodes are (a) 150 µm (b) 250 µm, and (c) 500 µm. Rests of configurations are set to same for all the three modules.

The e-beam trajectories are obtained at tip voltage -300 V and S2 voltage -245 V. The deflector voltages are adjusted so that the trajectories are deflected up to the edge of E3 but not exceeded. The adjusted deflected voltages are ± 38 V, ± 35 V, and ± 28 V for gap between electrodes 150, 250, and 500 µm, respectively. The trajectories show that the deflection is highest for the 150 µm gap and lowest for 500 µm gap. The deflection measurement from the axis are 175, 155, and 135 µm resembling scan range value double of its.

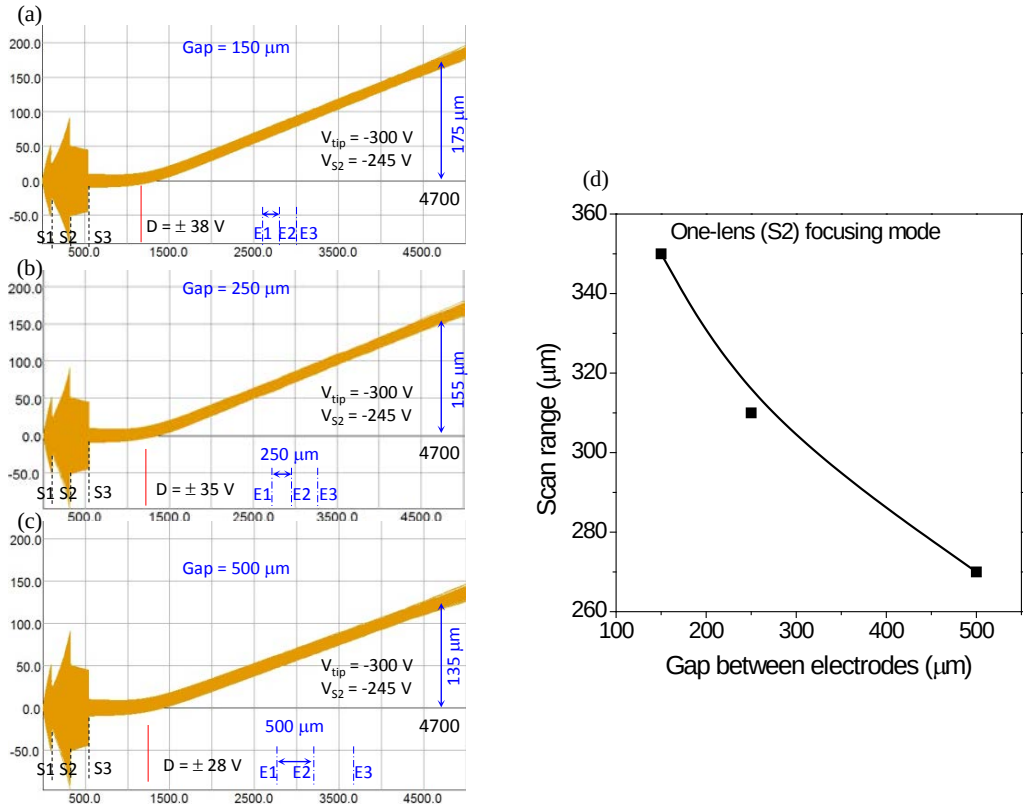


**Fig. 2.14** Electrodynamics simulation of e-beam trajectories inside microcolumn with various gaps between electrodes of Einzel lens in source lens focusing mode for gap between lens-electrodes (a) 150, (b) 250, and (c) 500 µm. (d) Plot for scan range versus gap between lens-electrodes.

## 2.6 Simulation of electron beam trajectories for various gap between Einzel lens-electrodes in two-lens focusing mode

In the two-lens focusing mode, the e-beam trajectories are first simulated without application of deflector voltages for gap between electrodes 150, 250, and 500 µm as presented in Fig. 2.15. The positions of source and Einzel lens-

electrodes are shown by broken black lines and solid blue lines, respectively. The position of deflector with its biasing voltage is shown by red solid line.

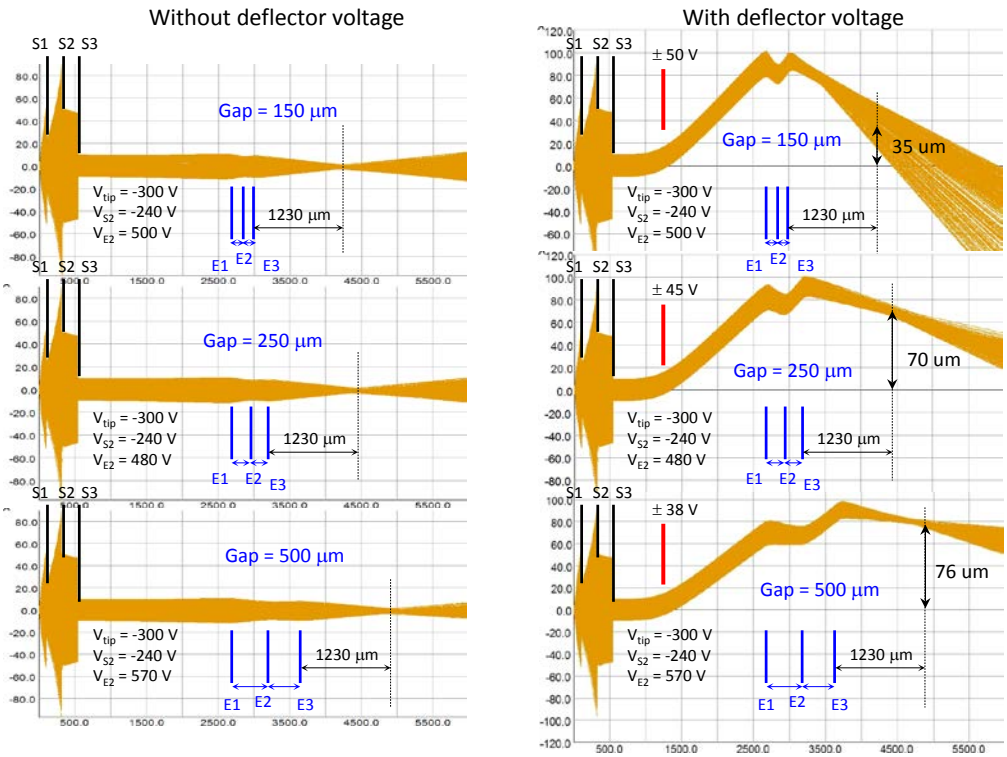


**Fig. 2.15** Electrodynamics simulation of e-beam trajectories inside microcolumn with various gaps between electrodes of Einzel lens in two-lens focusing mode. e-beam trajectories without applications of any deflector voltages (Left panel) and with deflector voltage (Right panel). The gaps between lens-electrodes are 150, 250, and 500 µm.

The trajectories are obtained at tip voltage -300 V, S2 voltage -240 V, and E2 voltages are adjusted so that the focal point is fixed from the third electrode of an Einzel lens. The required E2 voltages to focused the beam at same working distance (1230 µm) are 500, 480, and 570 V for gap between electrodes 150, 250, and 500 µm (left panel of Fig. 2.15).

When the deflector voltages are applied, the beam shifted as shown in right panel of Fig. 2.15. The deflector voltages are adjusted to keep the beam at the edge of third lens-electrode of Einzel lens. The required deflector voltages are ± 50 V, ± 45 V, and ± 38 V for gap between electrodes 150, 250, and 500 μm, respectively. Because of the E2 voltage, the beams are deflected back to the axis. The beam is cross over prior to the sample location (that is focal point when deflector voltage is not applied) and beam is spread and inclined at the sample position. The simulation results show that bending and spreading is larger for the narrow gap. The deflections of beam from the axis at the focal point are measured as 35, 70, and 76 μm. The simulation results of variation of scan range with gap between lens-electrodes is plotted in Fig. 2.16. In contrary to the one-lens focusing mode, here scan range increases with the increase in gap between lens-electrodes.

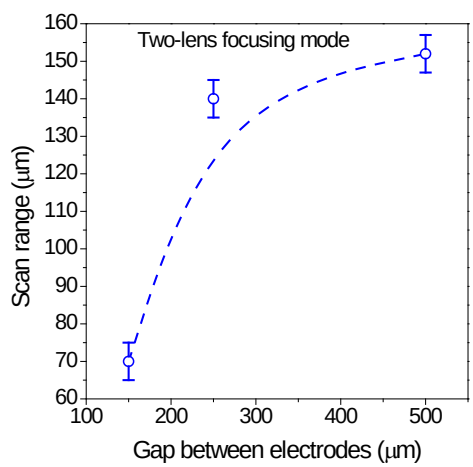


**Fig. 2.16** Scan range versus gap between electrodes in two-lens focusing mode.

In summary, two designs of an Einzel lens structure is presented. The major modification is the geometrical structure of lens-electrode. In the first model, it

is consists of a Si membrane with bulk Si as a mechanical supports but second model excludes bulk Si and Pyrex itself supports the membrane. The simulation of the electric field and beam trajectories inside the microcolumn indicates that the field distribution at the aperture region is barely affected by geometrical structure of the supporting material. However, the gap between lens-electrodes highly influence in the nature of lens. Thus the second design is modified for high flexible of gap between lens-electrode. For example, if a 100 μm Pyrex is used in between the lens-electrode the overall lens thickness will be <500 μm which can be safely used in low voltage operation. For the high voltage operation and the optimizing the gap between lens-electrodes, the Pyrex thickness can be selected accordingly.

For the experimental verification of the design and the simulation results, the lens is fabricated and microcolumn is characterized with the fabricated lens structure. Details are presented in the following chapters.

# 3 CHAPTER III: LENS FABRICATION AND MICROCOLUMN ASSEMBLY

An interest to fabricate suitable microlenses for a microcolumn is being fulfilled by robust MEMS fabrication technology despite of several technical limitations. This chapter investigates the implementation of MEMS technology in order to fabricate electrostatic lenses design presented in chapter II for an e-beam microcolumn. The MEMS technology is a top-down process which follows several steps of additive and subtractive processes such as lithography, oxidation, etching, and deposition.

Electrostatic lens design described in chapter II was fabricated following an approach given in flow chart (Fig. 3.1). The process is analogous to drill then bond technology as described in introduction chapter. It is possible to start with any of the Si substrate such as standard single crystal growth Si wafer, epitaxial growth Si wafer, and SOI wafer. According to the substrate selection, the fabrication process needs to be slightly amended. The key fabrication processes are photolithography, anisotropic deep Si etching, back side window etching, anodic bonding, and alignment of multiple lens-electrodes. Other processes may vary with the approaches and device availability. This chapter thoroughly describes the fabrication of lens.

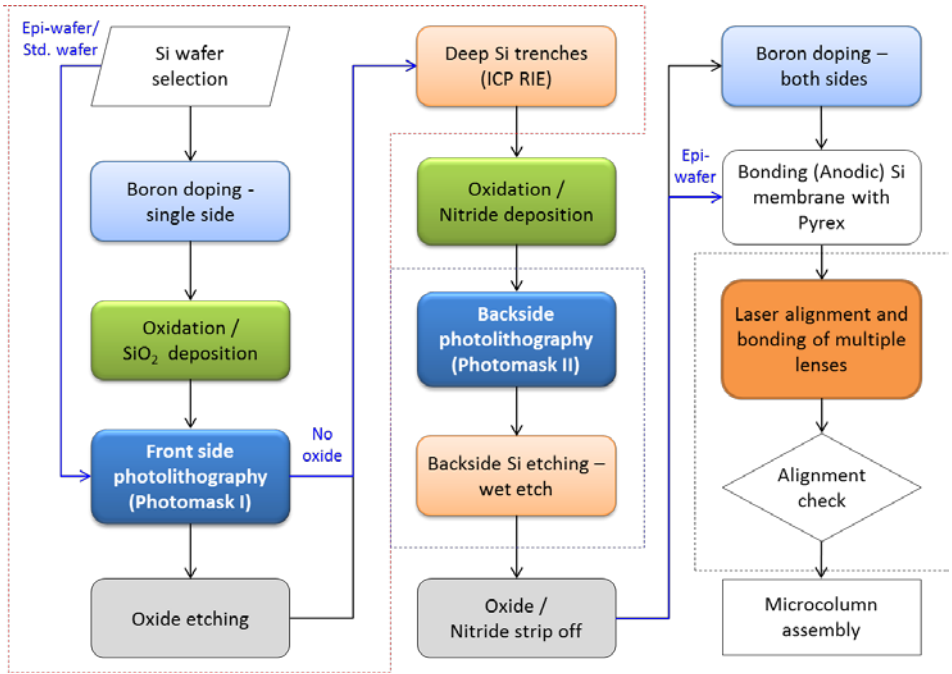


**Fig. 3.1** A flow chart for fabrication of a thin electrostatic lens using standard wafer. The process flow is almost same for both types of lens designs except alteration in the photomask II, anodic bonding, and detachment of Si membrane.

## 3.1 Photomask design

Several 2D photomasks with geometrically well-defined patterns have been designed to use them as a stencil to regenerate patterns on photoresist coated wafer. The photomasks are either made of soda lime glass coated with an optically thick chromium or thin transparent polymer sheet printed with optically opaque carbon. In either of types, computer aided design (CAD) was used to create patterns following e-beam lithography for Cr mask and offset printing for polymer mask. As a matter of fact, polymer mask was used for preliminary design test and then later Cr mask is used for a micrometer resolution.

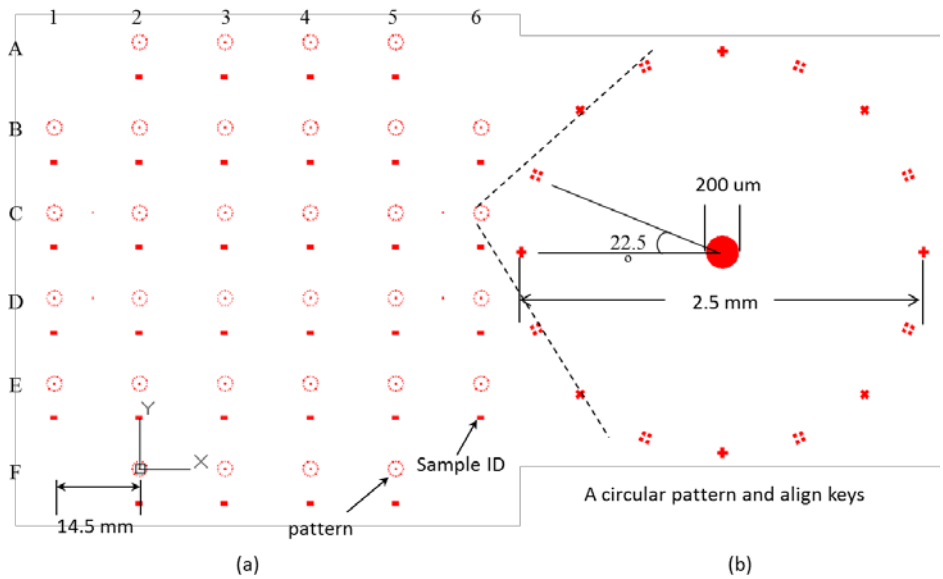


**Fig. 3.2** A photomask layouts for circular patterns. (a) A whole mask layout. (b) A sample die. 32 identical or different dies are arranged for 100 mm wafer. 16 align keys are arranged around a circular pattern of diameter 200 μm.

In this research, concave circular patterns of various sizes from 10 to 200 μm are designed in CAD software and grouped into various photomasks. For instance, Fig. 3.2 illustrates a CAD layout of a photomask designs used in this research. The designs include several sizes of circular patterns arranged for a 100 mm Si wafers. The sizes are 10, 20, 50, 100, and 200 μm; importantly, there are 16 align keys around the circle at radius 1.25 mm (Fig. 3.2 (b)). The align keys have two folds purposes: (i) to locate a micron size circular aperture on a big size (~ 15 mm × 15 mm) sample die and (ii) to align the multiple lens-apertures following the align keys positions. The alternate plus and square dots align keys are separated with radial angle of 22.5$^{o}$. The sizes of a square dot and

plus type are measured as 20 μm and 60 μm in width and length. At a single printing, it can be released 32 dies on a 100 mm wafer (Fig. 3.2 (a)).

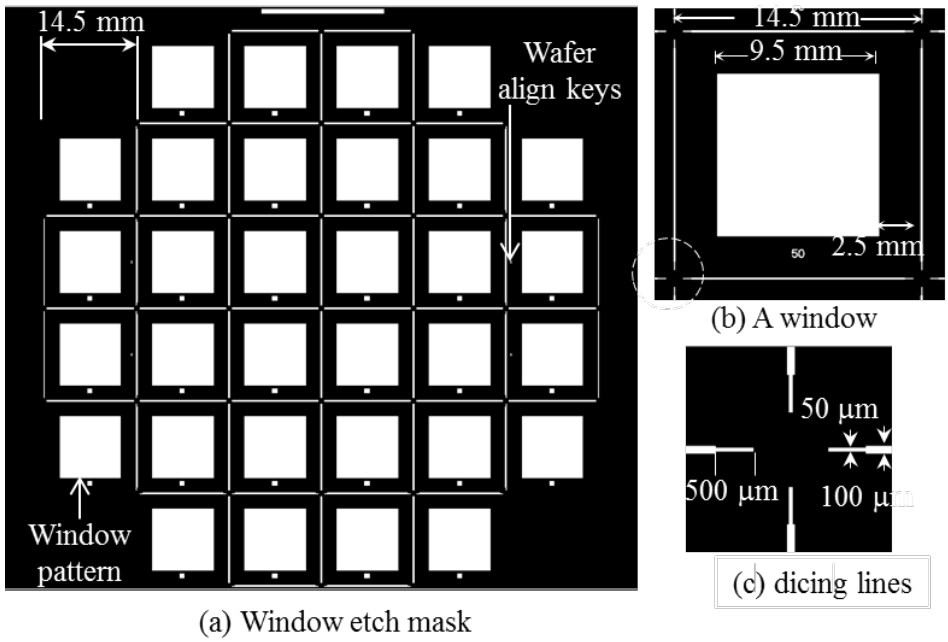


**Fig. 3.3** A photomask layout for back side window. (a) Whole window mask. (b) A window mask for a die. (c) Dicing lines. 32 dies are arranged in a mask for 100 mm wafer. Die and window sizes are 14.5 and 9.5 mm. The large size pattern is used to define the Si membrane area.

To define a membrane size, a back side photomask was designed as shown in Fig. 3.3. The size are measured as 9.5 mm × 9.5 mm and 11 mm × 11 mm which is quite big for micrometer thick Si membrane but it provides high freedom in selecting lens size. The membrane size is later defined by bonding a mechanical supports Pyrex and dicing out that specific area. While making thinner electrodes, the supporting Pyrex is bonded earlier before the Si membrane released out. In case, if the individual dies needs to be treated separately before

lens is released, dicing lines can be used to die the sample without damaging other samples. Of note, at the edges of dicing lines of width 100 μm, it is narrow down to 50 μm for 500 μm in length and another 500 μm is kept free for undercutting compensation (Fig. 3.3 (c)). Around the dies at four corner of the wafer, dicing lines are removed to prevent the wafer from breaking due to edge line grooves (Fig. 3.3 (a)).

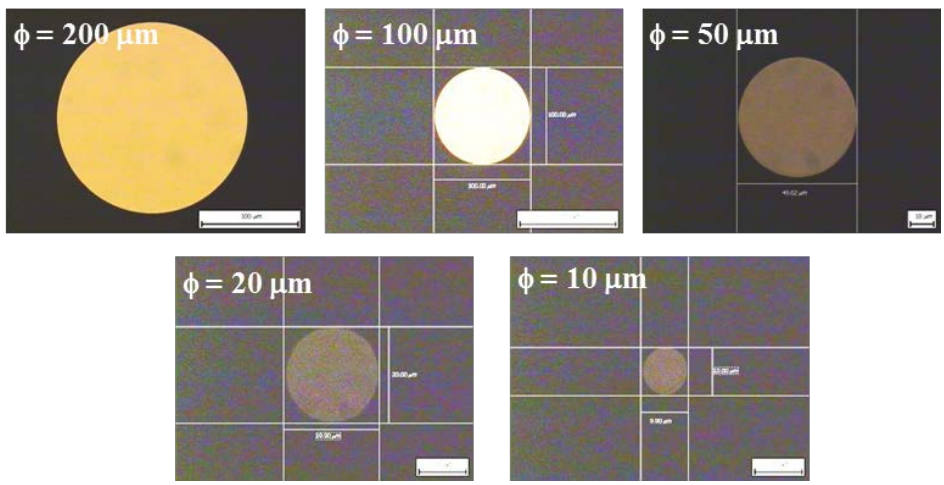


**Fig. 3.4** Optical images of circular patterns on printed photomask. The circle diameters are 200, 100, 50, 20, and 10 μm. The photographs resembled that circularity and edges are patterned on Cr-mask with sub-micrometer resolution.

After printing the photomask as designed above was inspected by optical microscope for fidelity test. The optical images of patterns with diameters 200, 100, 50, 20, and 10 μm are presented in Fig. 3.4. The direct measurement using the imaging software on some of images shows that the diameters of the circles are same as the design layout with measurement error less than ± 1 μm.

In the lens structure, circularity of aperture is crucial otherwise, the beam aberration may be a serious hurdle, thus, eccentricity of the least diameter (i.e.

10 μm) was also measured using optical images as shown in Fig. 3.5. Three randomly selected patterns of 10 μm circles were inspected along 0° and 90° orientations. The mean eccentricity was calculated as 0.004945 ± 0.001959 (Table 3.1). The measurement shows that the circular patterns on the Cr-photomask are circular with the resolution of sub-micrometer.

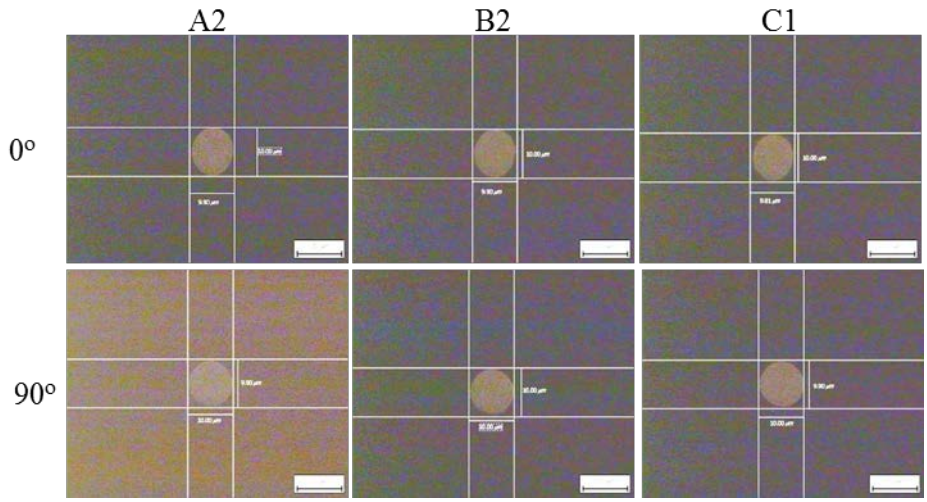


**Fig. 3.5** Optical images of randomly selected 10-μm circular patterns on a printed photomask at 0° and 90° orientation. The images shows that photomask is fabricated with resolution of sub-micrometer size.

**Table 3.1** Circularity measurement of 10-μm circular patterns on a photomask.

| | A2 | | B2 | | C1 | |
|---|---|---|---|---|---|---|
| position | $d_1$ (μm) | $d_2$ (μm) | $d_1$ (μm) | $d_2$ (μm) | $d_1$ (μm) | $d_2$ (μm) |
| 0° | 9.9 | 10.0 | 9.9 | 10.0 | 9.8 | 10.0 |
| 90° Rotation | 9.9 | 10.0 | 10.0 | 10.0 | 9.9 | 10.0 |
| Mean | 9.9 | 10.0 | 9.9 | 10.0 | 9.9 | 10.0 |
| Eccentricity | 0.005025126 | | 0.002506266 | | 0.007302946 | |

## 3.2 Patterning

Photolithography is the first and critical process for fabricating geometrically well-defined structures which resolution is determined by the photomask aligner, photoresist (PR), and developing and etching processes. It ideally transfers the patterns with resolution down to diffraction limit of wavelength of light used. But in practical, there are several limitations, such as alignment accuracy, resist sensitivity, refraction of the transparent material used in photomask, and user capability in handing the processes. With the optimization of etch steps in photolithography process, the aperture can be well-fabricated with the resolution of 1 μm. Most of the resists is sensitive to particular wavelength but stable at normal day-light. Commonly used light source is ultra violet light (Hg i- line, 365 nm) which changes the structure of the PR either chemically or physically so that it either dissolves or resists with developer. For the better resolution, the lower wavelengths like extreme UV, or X- ray has been practiced but required extra cost and sophisticate equipment.

Resist may be either positive or negative tone on the basis of reaction with light. The former gets dissolved in developer when exposed to light hence applicable to transfer the exact patterns on wafer. But, the later gets harden and developer can dissolve only the unexposed resist so it is used to transfer reverse of the photomask patterns. Positive resist is better in resolution and step coverage than its counterpart but negative resist is good in adhesion and chemical resistance. In this research, positive tone resist was used because of its reliability, step coverage, and high resolution.

The photolithography process is illustrated in Fig. 3.6. The process was carried out on a standard double side polished (dsp) Si wafers (Fig. 3.6 (a)) beginning with coating of photoresist on a cleaned substrate (Fig. 3.6 (b)). Adhesive promoter was first coated on the substrate for adhesion of photoresist on Si wafer. Especially, adhesive layer is required for thick and positive resist; otherwise resist may swell resulting low resolution. Baking the resist in an oven or hot plate at lower temperature (e.g., 90 $^{o}$C) was endorsed prior to expose which removes moist and make resist stable. UV was exposed through photomask on PR coated substrate (Fig. 3.6 (c)) which weakened the resist at the pattern region. While developing, the exposed region (pattern) got dissolved into developer (Fig. 3.6 (d)) retaining PR on other region revealing the patterns on the PR coated substrate. The remaining PR firmed as etch mask for further wet or dry etching process of Si or other material. Deep Si etching process was carried out in this research after lithography (Fig. 3.6 (e)) and then the PR was strip off (Fig. 3.6 (f)) as its service had been completed. This completes a transfer a pattern on Si wafer. Details of each steps is explained in following sections with experimental results.

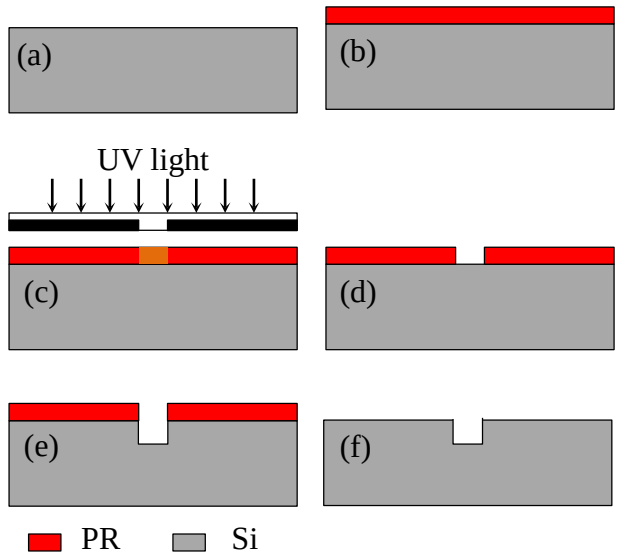


**Fig. 3.6** Photolithography process (schematic representation). (a) Si wafer, (b) HMDS and PR coating, (c) mask alignment and UV light expose, (d) development, (e) Si etching, and (f) PR strip off.

### 3.2.1 Photoresist spinning

Photoresist is a sacrificial layer used in microfabrication for various purposes such as to transfer the patterns on a substrate, to provide masking layer during etching process, to provide various three dimensional structures etc. Here, the photoresist was used for transferring patterns on substrate and etch mask for etching Si, $SiO_2$, and $Si_3N_4$. The main components of photoresist are: a polymer (a base resin), a sensitizer, and a casting solvent. The polymer changes structure when exposed to radiation; the solvent allows spin application and formation of thin layer on the wafer; sensitizers control the photochemical reaction in the polymeric phase. For a better resolution, it is required to select possibly high sensitive and thin layer of photoresist.

An illustration of PR coating process is presented in Fig. 3.7. The wafer was first coated with Hexamethyldisilazane (HMDS) as an adhesion promoter. It was coated by spinning the HMDS with low (500 rpm) and high (2000 rpm) speed for 5 and 10 s, respectively; however the recipe can be adjusted as required without any adverse effects.

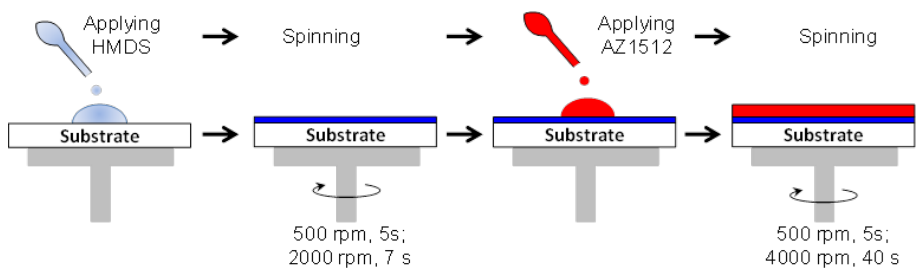


**Fig. 3.7** An illustration of HMDS and PR coating on a Si wafer. The recipe is an example to coat ~1.2-μm-thick PR (AZ 1512) on Si wafer. The recipe is subject to change with nature of PR and thickness required.

The surface layer of silicon dioxide (~20 Å $SiO_2$ is always present on wafer exposed to atmosphere) on the wafer reacts with HMDS to form tri-methylated silicon-dioxide, a highly water repellent layer. This hydrophobic layer prevents the aqueous developer from penetrating between the photoresist layer and the wafer's surface, thus preventing so-called lifting of small photoresist structures in the (developing) pattern. Photoresist (e.g., AZ1512), a viscous liquid, was then dispensed on HMDS layer and first spun at low speed (e.g., 500 rpm) for a few seconds (e.g., 5 s) to uniformly spray the PR on whole wafer and then spun with high speed (e.g., 4000 rpm) for several seconds (e.g., 35 s) to produce a thin uniform layer. The thickness of PR highly depends upon the spinning speed; the recipe given as example coats ~1.2 μm.

The actual thickness, T, of the resist depends upon its viscosity, η, solution concentration, C, and spinning speed, ω. The empirical expression of PR thickness is given as [58]:

$$T = \frac{KC^{\beta}\eta^{\gamma}}{\omega^{\alpha}} \qquad 3.1$$

where, K = overall calibration constant. The exponential factors α, β, and γ have to be experimentally determined. The equation 3.1 can be used to estimate PR thickness on the wafer. The spin coated wafer is required to be baked at low temperature (e.g., 95 $^{o}$C) at hot plate for short time (e.g., 90 s) or convection oven (e.g., 30 min). It is called soft bake or pre-bake because it does not make resist hard instead it helps in removing solvents and stress and promoting better adhesion of the resist layer on wafer. It is required to care that the exposure time for the particular thickness has to be increased if the baking is done at higher temperature. Longer exposure time sometime damages the edges of patterns due to the reflection of UV ray from silicon surface. Anti-reflection coating (e.g $SiO_2$ or $Si_3N_4$) on Si surface reduces the UV scattering. As the edge roughness is important, it is better to perform soft baking at lower temperature (e.g., 85 $^{o}$C) for a minute for thinner PR so that low dose of UV is enough. Without soft baking process, the edges of patterns may not be well defined due to flow of solvent. Hence, soft bake is mandatory for contact lithography. When thick PR is required, AZ 7220 was used instead of AZ 1512 because the thickness coated by former PR is ~2.7 μm that is more than double thickness coated by later one. Double layer coating of PR was also sometime practiced for PR thickness >3 μm. Double layer coating was required to resist it as etch mask for etching >1

μm $SiO_2$ or $Si_3N_4$ etching in oxford RIE because selectivity over PR was almost 2:1.

For Deep Si etching, either PR or $SiO_2$ can be used as an etch mask which selectivity is roughly 1:100 and 1:600, respectively. Some processes have been forwarded with just PR as the etch mask but some are performed with oxide as etch mask. There is no such remarkable difference in their results for low etching depth. In some cases, PR got damaged while etching over 25 μm. So, thick PR or double layer coating was safely used for deeper trenches (>25 μm). Otherwise oxide etch mask was used for well protection although it added two more steps and cost in fabrication.

### 3.2.2 Mask alignment and exposure

After soft baking, PR coated wafer is ready for ultraviolet exposure through a photomask. The purpose of illumination is to transfer or printing of the mask image onto the resist in the form of a latent image perfectly. It is performed delivering light energy of appropriate dose (e.g., 60 - 80 mJ/cm$^2$ for 1.2-μm-thick-AZ 1512 and 250 - 275 mJ/cm$^2$ for AZ 7220), intensity (e.g., 10 – 20 mW/cm$^2$ from Hg lamp), direction (e.g., divergence <5$^o$), spectral characteristics (e.g., wavelength of 365-nm from Hg-i-line), and uniformity (e.g., <5%) across the wafer. A conventional mask aligner MA-6 (Karl Suss MA-6 Mid/Deep UV Mask Aligner) was used to align photomask (Fig. 3.6 (c)). The exposure was performed in three different modes namely, vacuum (low and high), contact (soft and hard), and proximity providing resolution from 0.5-5 μm.

The resolution depends upon the choice of photoresist (higher sensitive to particular wavelength gives better resolution), PR thickness (thinner the PR better the resolution), mode of contact (high vacuum has better resolution), mode of alignment (bottom side alignment has lower resolution), gap between photomask and wafer (smaller the gap better the resolution), and wavelength of radiation (smaller the wavelength better the resolution) [59]. In this research, high vacuum mode was used for front side circular patterns (feature size: 10 μm) and contact or proximity printing for back side window patterns. The life time of photomask increases if the photomask is out of contact with PR during exposure, hence proximity printing can be used where high resolution is not required.

However, either vacuum contact or hard contact was used for the circular pattern because the resolution is important for it. But for the case of large area back side mask patterning, proximity patterning does work as it avoid contact with PR which extends the life time of photomask. the expose time for single coated AZ 1512 and AZ 7220 were 5 and 17 s if the power intensity was set to 15 $mW/cm^2$, and for double coating, 7 and 20 s were enough.

### 3.2.3 Development

Development is a chemical process in which an alkaline or organic developer washes out either uv exposed PR (for positive tone resist) or non-illuminated PR (for negative tone resist) by dissolving selective resist into it and revealing latent images (Fig. 3.6 (d)). A dry development processes using $O_2$-$SO_2$ plasma etching has been developed [60-63]. It transforms the latent resist image into a relief

image that will serve as a mask for further subtractive (*e.g.*, oxide etching) and additive (*e.g.*, deposition and lift off process) steps. Wet development exploits at least three different types of exposure-induced changes: variation in molecular weight or the polymers, reactivity change, and polarity change. Dry development uses differential etch rate to $O_2$-RIE of exposed and non-exposed resist. The commonly used developers are AZ MIF 300 for AZ 1512, CD 30 for AZ 7220, and 400 K for AZ 5412. The developing time varies with expose time and PR thickness nevertheless the time is no more than 1 or 2 min. Moderated shaking of the wafer improves uniformity and helps in complete development.

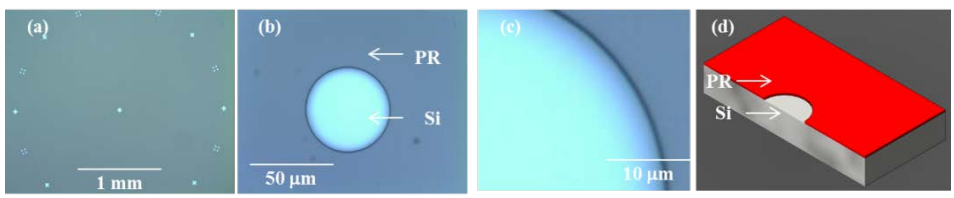


**Fig. 3.8** Optical images and schematic of patterns after development. (a) Optical image of patterns at lowest magnification (50×). (b) A circular pattern at higher magnification (1000×). (c) Zoom in of image (b). (d) Cross section illustration of substrate after PR development. The images resembled that the photolithography was carried out with sub-micrometer resolution.

To remove unwanted and waste materials or to stop overdevelopment, rinsing in deionized water (DIW) was performed. Before further process, the process wafer is mandatory to be inspected by optical microscope to confirm the transfer of patterns accurately. If the transferred patterns are undesirable because of bad expose, or bad development, or dirty surface etc, the lithography process can be re-started without any damage in wafer. Fig. 3.8 shows optical images and schematic of patterns after development process. The images resembled high

fidelity of photolithography. Of note, Align keys are well seen around the circle (Fig. 3.8 (a)), a circularity of the patterns is well defined (Fig. 3.8 (b)), and edges are smooth (Fig. 3.8 (c)). The schematic illustrates a substrate status after development (Fig. 3.8 (d). Beside the above example, some more circular patterns have been transferred on oxidized wafer as presented in Fig. 3.9. The diameters of circular patterns transferred on PR are (a) 10 μm, (b) 20 μm, (c) 50 μm, (d) 100 μm, and (e) 200 μm. Fig. 3.9 (d) illustrates a cross section of silicon oxide substrate after development. Although there are no remarkable difference in patterns transferring on oxidized wafer and bare wafers, photoresist adhesion on oxide is better and damages due to UV reflection is negligible in oxidized wafer.

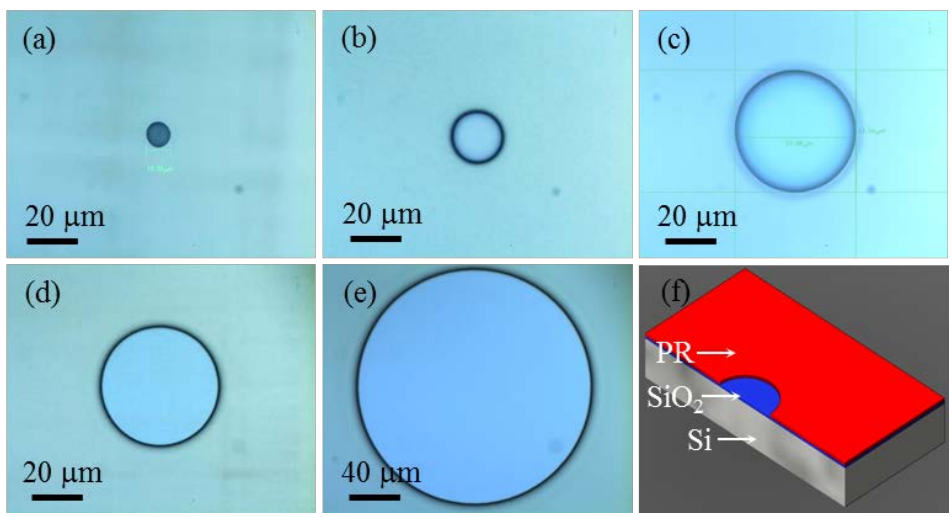


**Fig. 3.9** Optical images of various circular patterns after the development process. (a) $\phi$ = 10 μm, (b) $\phi$ = 20 μm, (c) $\phi$ = 50 μm, (d) $\phi$ = 100 μm, (e) $\phi$ = 200 μm, (g) cross section diagram after development.

Post baking (or hard baking) is an important not only to cure the PR stability on the Si substrate but also to resist strongly during plasma etching. The wafer

### 3.2.4 Post baking

was post baked at higher temperature (e.g., 110 $^{o}$C) and for longer times (e.g., 2 min in hot plate or 30 min in oven). Post baking is required to be carried out prior to etching process because resist gets weakened adhesion to substrate due to penetration of developer into resist (in worse case, swelling of resist due to solvent penetration at interface). Post-baking or hard baking process removes residual solvents and anneals the film to promote interfacial adhesion of the resist. It also hardens the film which increases the resistance of the resist to subsequent etching steps.

Hard baking is a mandatory process prior to dry or wet etching to make the resist hard, strong, and resistive. Higher the temperature and longer the baking time, the resist becomes harder and strongly adhesive to the substrate. It is important to select the baking temperature and time so that it could resist during the etching process and could be removed by standard strip off process. If the resist is baked in higher temperature (>150 $^{o}$C) for longer time, it may not be removed even by piranha solution and ashing. In this research, hard baking was done at 110 $^{o}$C for 60 to 90 s on hot plate.

## 3.3 Oxide and Si etching

Oxide etching was done in Oxford RIE chamber using PR as an etch mask. Fig. 3.10 shows an optical images and a cross section view after oxide dry etched. The completion of oxide etching can be easily tested by noticing a bright shining surface of Si. The etched surface of circle (Fig. 3.10 (a) and (b)) looks

bright and shining as compared to the surface before oxide etching (Fig. 3.9 (a) – (e)).

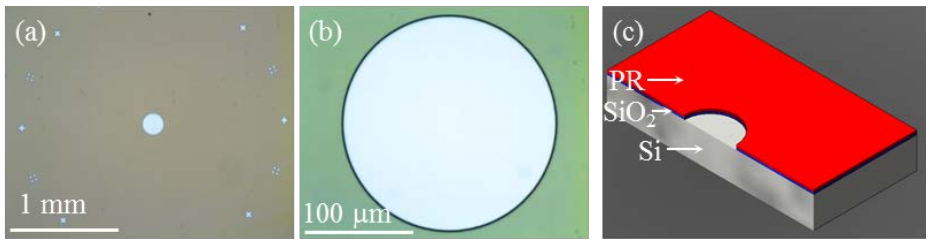


**Fig. 3.10** Optical images and cross section view after oxide dry etching process. (a) Circular pattern with align keys. (b) A 200-μm circular pattern on Si surface. (c) A cross section view after oxide dry etching following the lithography process.

In RIE chamber, RF glow discharge produces etchants by dissociating and ionizing $CF_4$ gas. $CF_4 + e = CF_3^+ + F + 2e$. The ion F does etch $SiO_2$ by liberating Si atoms and forming $SiF_4$. It etches oxide ~ 300 Å/min with selectivity over PR ~2:1. Alternatively, buffer hydrofluoric acid (mixture of 49% HF and $NH_4F$ (1:5)) also can be used for oxide etching for larger pattern size. But smaller pattern size could not withstand this sort of isotropic oxide etching, so for circular pattern, dry etching was always followed. In both cases, the exposed oxide is etched away without attacking resist and silicon substrate.

Deep Si trenches were made on Si substrate using inductively coupled plasma deep reactive ion etcher (ICP- DRIE). Either photoresist or $SiO_2$ was used as an etch mask for DRIE because of their high selectivity, roughly, 1:100 and 1:600 for PR and $SiO_2$. The detail of deep Si etching mechanism is discussed in section 3.4 and one of typical results is presented in Fig. 3.11.

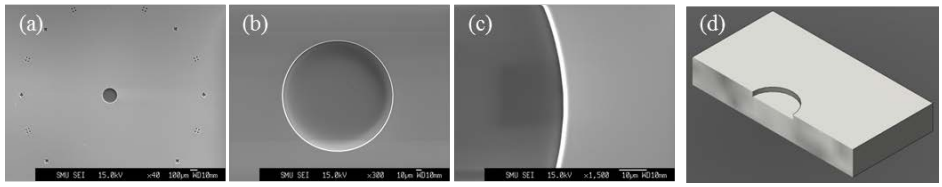


**Fig. 3.11** SEM images of circular patterns made for e-beam aperture after DRIE process. (a) Circular pattern with align keys. (b) A circular pattern imprinted on Si substrate. (c) Magnified SEM of an edge. (d) Cross section view of imprinted pattern on Si substrate.

## 3.4 Deep reactive ion etching (DRIE)

There are two main established technologies for high-rate deep anisotropic plasma etching of silicon: cryogenic [64-66] and Bosch [67-69]. In cryogenic process, the etching takes place at -110 $^{o}$C, in order to slow down spontaneous chemical etching by radicals that isotropic in nature and only vertically accelerated ions drive the etching process making vertical ($90 \pm 2^{o}$) etching [70]. No commercial cryogenic etcher has been available because of extra cost in lowering down the temperature.

The Bosch is a standardized industrial anisotropic deep Si etching process which follows time-multiplexed or pulsed etching method in a cycle of passivation and etching. First, it etches the exposed Si and then deposit passivation layer to protect the vertical wall. The process returns to the etching cycle where vertically accelerated ions bombard the bottom of the previously etched trench removing the passivation layer and then etching Si which is isotropic in nature. With the shallow etch cycle, the overall etching appeared vertical (Fig. 3.12).

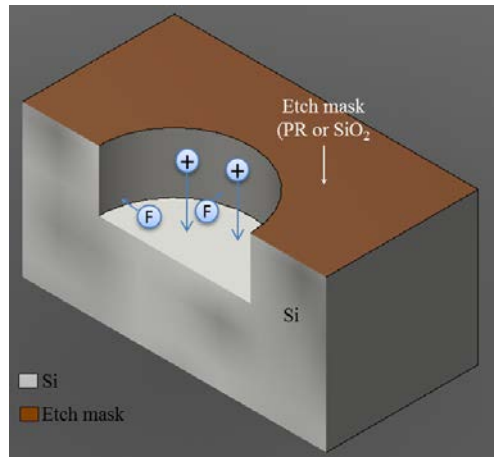


**Fig. 3.12** Passivation and etch cycle in typical DRIE step. Cycles of isotropic etch of silicon in exposed region on the wafer and deposition of polymer CFn. The etchings of polymer as well as silicon take place at the bottom of the trench by vertically directed positive ions.

Unlike anisotropic wet etching, RIE is not limited by the crystal planes in the silicon. A very-high aspect-ratio silicon etching method referred to as deep (D)RIE relies on a high-density (inductively coupled) plasma source and an alternating process of etching and protective polymer deposition [71] to achieve anisotropy in order of 30:1 (side-wall angles 90 ± 2°, with photoresist selectivity of 50-100:1, silicon dioxide selectivity of 200–600:1, and etch rates in order of 2–3 μm/min [72, 73].

For building high-aspect-ratio micromachines with dry etching, high-density plasma ($>10^{11}/cm^3$) is directed towards the silicon surface by protecting its sidewalls. The typical DRIE system consists an inductively coupled power (ICP) source to provide a high density plasma and an independent substrate power biased to provide directional ion bombardment during the etch step. For the protective layer of polymer deposition, a Plasma Enhanced Chemical Vapor

Deposition (PECVD) is incorporated in the chamber. Passivation layer is first deposited by passing $C_4F_8$ (Octofluorocyclobutane), and then etching is simultaneously carried out by substrate bias and flow of $SF_6$ (Sulfur Hexafluoride). During the etching step, the sidewalls of the silicon trench are relatively protected by the $C_4F_8$ induced polymer layer. Although polymer is also coated at the bottom, it is pierced by the directional ion bombardment and the bottom silicon is then "etched" by means of physical and chemical phenomena. The iteration of these passivation/etch cycles allows the desired anisotropic features to be achieved.

The etching mechanism is attributed by both the physical and chemical etching phenomena as explained below [74-77].

$$SF_6 + e^- \rightarrow SF_x^+ + SF_y^- + SF_x^* + F^+ + F_z^- + F^* \qquad 3.2$$

Where x = {0,1,2,3,4,5}, y = {4,5,6}, z = {1,2}.

The Si etching reactions are

$$Si_{solid} + 4F \rightarrow SiF_{4_{gas}} \qquad 3.3$$

$$Si_{solid} + 2F \rightarrow SiF_{2_{gas}} \qquad 3.4$$

The vertical sidewalls or anisotropic etching is achieved by passivation covered with CF or $F_x$ monomer which is generated by plasma dissociation of $C_nF_{n+2}$. The $SF_x$ reacts with $CF_X$ deposited on the polymer, forming non-volatile reaction products which guard the sidewall from etching.[78, 79]

$$C_4F_8 \rightarrow CF_x \rightarrow (CF_x)_n \text{ ,}\{x= 1,2,3\}$$

In all the 32 circular patterns on a 100 mm Si wafer, uniformity of the etch depth (15 μm) and edge looks quite satisfactory (Fig. 3.13). The etching was down on a SOI wafer which has 15-μm device layer on 2-μm buried oxide. After fabricating deep Si trenches on a Si wafer, the photoresist was stripped off by $O_2$-Plasma ashing process. This process burn out the organic photoresist as well as polymer residue remains during the RIE process.

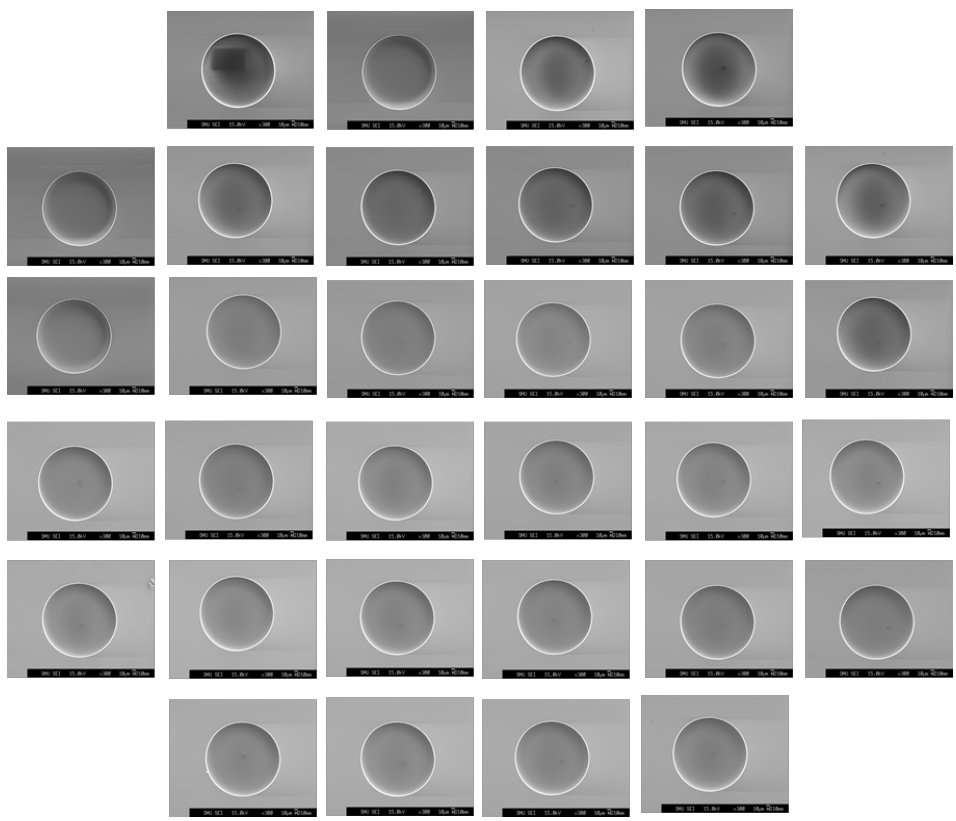

**Fig. 3.13** SEM images of circular patterns on a 100 mm wafer after vertical etched down to 15 μm using DRIE process. Photoresist AZ 7220 was used as etch mask. The etch uniformity is quite satisfactory.

## 3.5 Photoresist strip off

The function of PR in our research is to use it as a sacrificial layer to transfer patterns on the substrate. Once the function of PR is over, the sacrificial layer is striped off (Fig. 3.6 (f)). Oxygen plasma ashing was carried out to strip off the PR. Alternatively, PR can be intensively removed by immersing the wafer into sulfuric acid and hydrogen peroxide mixture ($4H_2SO_4$:$1H_2O_2$ at 120 $^oC$) (SPM) for 10 – 20 min. Other commercial liquid strippers such as $H_2SO_4$-$Cr_2O_3$, $1NH_4OH$:$5H_2O$:$1H_2O_2$ (RCA1), ACT-690, ACT-140 etc are also useful in PR stripping. If the PR is not baked at high temperature (<120 $^oC$), simply the acetone does remove the PR with the aid of ultrasonic cleaning.

## 3.6 Deposition/oxidation of an etch mask

To protect Si substrate except in the region to be etched, etch mask is required on the Si surface (Fig. 3.14). $SiO_2$, $Si_3N_4$, and metals (e.g.,, Cr, Au, Al etc.) can be used as an etch mask during the chemical wet etching process because the etch selectivity of those materials over Si is 1:>1000. Deposition and oxidation are two generic processes for addition of etch mask on surface. Low pressure chemical vapor deposition (LPCVD) and thermal wet or dry oxidation are used for $Si_3N_4$ deposition and $SiO_2$ growth, respectively. PECVD deposition of $SiO_2$ also can be used as etch mask however the resistivity is quite lowered than oxidized $SiO_2$. Thus thicker oxide is required.

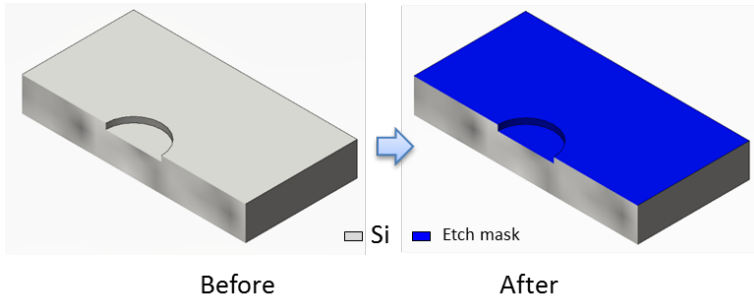


**Fig. 3.14** A schematic illustration of etch mask addition on the Si surface. Etch mask is required to protect Si surface while back side wet Si etching.

## 3.7 Wet Si etching

Anisotropic wet chemical etching, a well-known orientation dependent etching mechanism, of Si was followed using tetramethyl ammonium hydroxide (TMAH) to etch out back side bulk Si. An illustration of back side patterning and wet Si etching process is shown in Fig. 3.15 with schematic (a) and cross section (b) representing diagrams. Wet etching is inherently an electrochemical process in which electron transfer process occurs between etchant and the etching materials. The TMAH etching gives almost smooth surfaces of well-known Si planes (*e.g.*, (111), (100), (101), (311) etc.). Moreover, it is easy and cheap method as compared to dry etching method. Seidel *et al*. (1990) presents mechanism of Si etching in alkaline solution as [80]:

$$Si + 2OH^- + 2H_2O \rightarrow SiO_2(OH)_2^{--} + 2H_2$$

Two essential reactions take place in silicon etching phenomena: (a) $OH^-$ oxidizes the Si producing soluble silicon compound ($SiO_2(OH)_2$) and (b) electronic charge reduces the water producing $H_2$ gas.

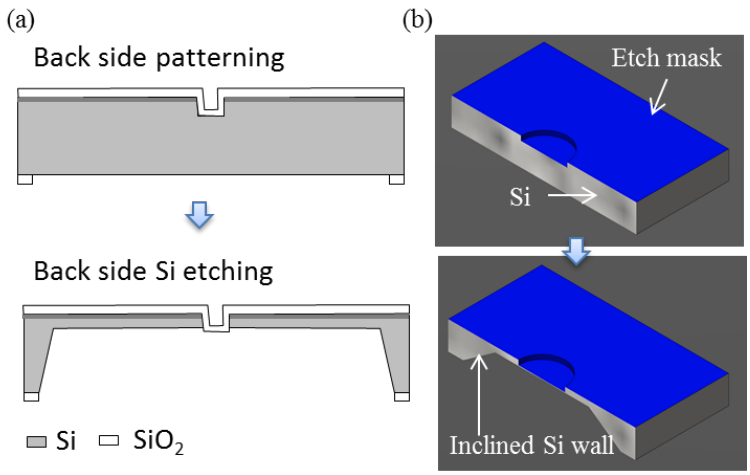


**Fig. 3.15** Schematic representation and cross section of back side patterning and wet Si etching. (a) Schematic of back side patterning and wet Si etching process. (b) Cross section of the substrate before and after wet Si etching process. The Si etching process should be stopped as soon as the pattern observed from the back side of etched window.

The experimental results after the completion of back side Si etching are illustrated in Fig. 3.16. The Fig. 3.16 (a) is a photograph of a 100 mm Si wafer at back side of the circular patterns transferred after the pattern released at back side Si etched region. The etched region looks shining Si color and top layer appears greenish/reddish color because of the presence of oxide layer which was used as an etch mask during etching process. Fig. 3.16 (b) is the SEM images of the circular patterns revealed at the back side Si etched region after the completion of the wet etching process. The wet etch process was stopped by etching time required to be etched for the target thickness. The first row shows Si surface with align keys around the circular pattern. Second row shows protruded oxide circular pattern of various aperture sizes of diameters (i) 20 μm (ii) 50 μm, (iii) 100 μm, and (iv) 200 μm. Bulged circular patterns are seen on the SEM pictures due to protrusion of the oxidized circular trenches. If we

further etched down, the protrusion part will be more exposed. For making circular lens-aperture, the amount of protrusion does not matter as long as the symmetric smooth circular Si edges exist.

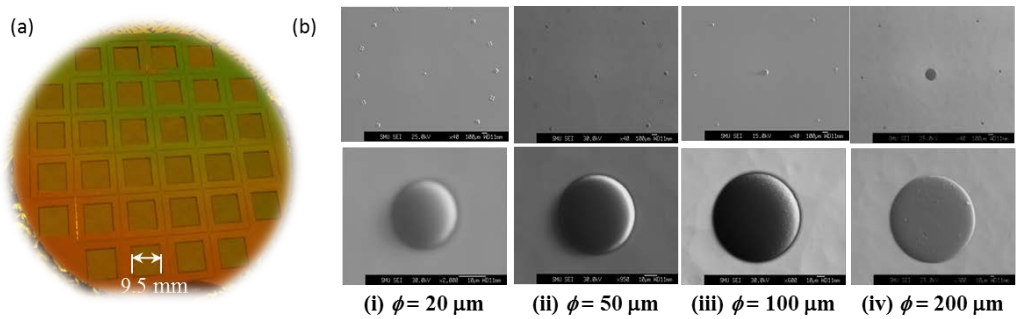


**Fig. 3.16** Photograph and SEM images at back side Si etched region. (a) A photograph of backside wet Si etched region. (b) SEM images of various circular patterns revealed at back side Si etched region. Diameters of the circular patterns are (i) 20 µm, (ii) 50 µm, (iii) 100 µm, and (iv) 200 µm. The protruded height of oxide/nitride does not differ the geometry of aperture as long as the edges are smooth and membrane is mechanically survived.

Some of the important issues are to be considered when selecting a bulk micromachining process and Si etchant.

Etch rate: The rate of removal of selective amounts for silicon from a substrate. It depends upon the orientation, concentration, mixture of silicon or other components with the etchant, pH of the etchant, temperature etc. [81].

Etch rate selectivity: Selectivity is defined as the ratio between the etch rate of the targeted material and that of non-intended materials, such as mask layers. The selectivity ratio should be as large as possible.

Processing temperature: TMAH etch rate of silicon increases exponentially with temperature [82].

Etch uniformity across a wafer: Etch uniformity depends upon the uniform distribution of dopant (*e.g.*, Boron in p-type wafer), Si impurity, uniformity of thickness etc. [83].

Sensitivity to overtime etch: Patterns on a wafer should be designed in such a way that some of the patterns should have tolerance with over etch. It is normally required because of non-uniform etching, non-uniform thickness throughout the entire wafer.

Safety and cost of etchants: TMAH is highly controllable, contaminant free etching, CMOS compatible, higher selectivity over oxide or nitride, and cheaper though hazardous for health if inhaled [84].

Surface finish and defects: The smoothness is important for many devices and material performance. TMAH concentration (>20 wt.%) gives smooth etching for almost all Si orientation. Lower concentration normally produces hillocks. Use of surfactant or IPA improves the surface smoothness [85, 86].

## 3.8 Passivation layer ($SiO_2$ / $Si_3N_4$) strip off

Etching is a subtractive process in which unwanted materials are removed from a substrate either by chemical reaction or physical method. There are two types of etching: dry and wet etching. In both type of etching, both isotropic and anisotropic etchings are possible for various materials. Circular Si apertures were released after the passivation layer stripped off. Fig. 3.17 illustrates a schematic (a) and cross section (b) representation of etch mask strip off following the back side Si etching process.

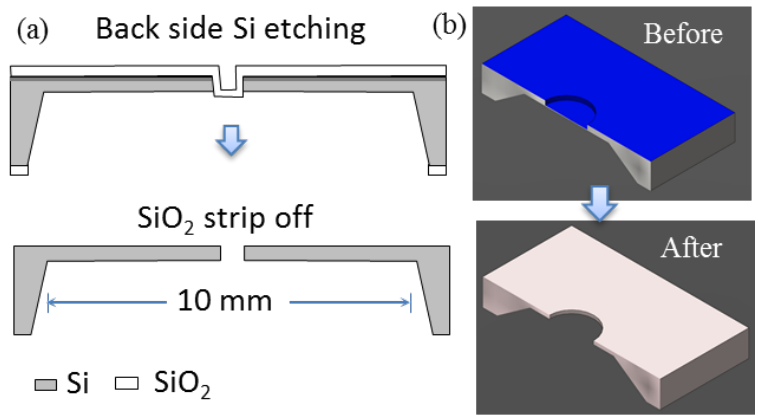


**Fig. 3.17** Schematics and cross section representations of before and after oxide strip off. (a) A schematic of back side Si etching and $SiO_2$ strip off. (b) Cross section of substrate before and after oxide strip off showing revealed of Si aperture.

The experimental results of oxide striped off that revealed the circular Si apertures on the Si membrane are shown in Fig. 3.18. The SEM images are of circular aperture at low and high magnification. The circular holes provide path of electron beam as well as electrostatic force on electron which define the electron trajectories inside the column.

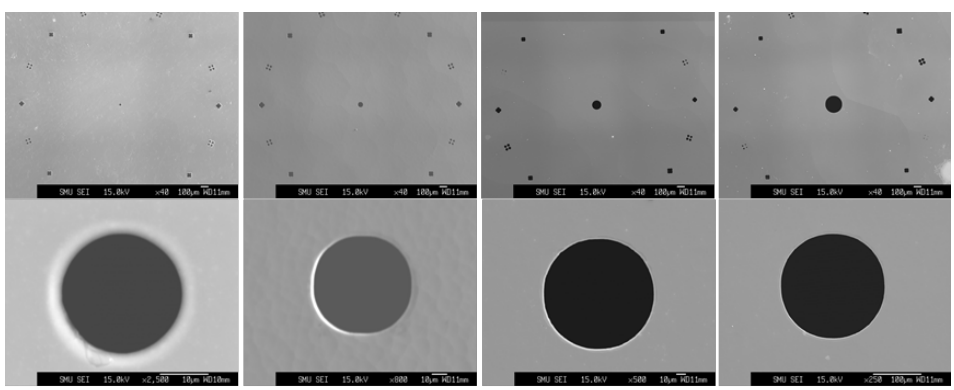


**Fig. 3.18** SEM micrographs of circular Si aperture released after oxide/nitride striped off. First row is Si surfaces with align keys around the circular aperture. Second row is

magnified image of circular apertures. Diameters of the circular patterns are (i) 20 μm, (ii) 50 μm, (iii) 100 μm, and (iv) 200 μm

## 3.9 Boron Doping

An ideal electrostatic lens electrode should be perfect conductor; however, microcolumn components are being fabricated on Si based microfabrication technique. The Si based electrostatic components surrogates the conductor because the conductivity of Si can be increased by doping electron acceptor (or donor) impurities like boron (or arsenic). With boron doping, the carrier concentration can be increased from intrinsic silicon $1.08\times10^{10}$ $cm^{-3}$ [87] to $\sim1.0\times10^{20}$ $cm^{-3}$ [88] at room temperature which conductivity is comparable to metals and boron doped Si can be used in microcolumn as a replacement of metal.

The doping in single crystal growth silicon is performed in many ways. Some of the well-established methods are: (i) solid diffusion method, (ii) reflow process of dopant gases such as diborane ($B_2H_6$), boron tribromide ($BBr_3$), boron trimethyl ($B(CH_3)_3$), and boron trichloride ($BCL_3)_3$) (iii) spinning on dopants, and (iv) ion implantation such as diborane ($B_2H_6$) and trifluoride (BF3). The first method is simple, easy, safe, and high wafer load capacity. For purity of dopants, reflow process does work better but health hazardness and non-uniformity are negative part. Spinning on dopants method is simplest method but high surface damages. Ion implantation method is uniform and safe process beside some silicon damages and expensive process.

Electrostatic lens-electrodes used in this research were either made of highly boron doped single growth crystal device layer or an epitaxial layer formed with high temperature solid diffusion method. A solid BoronPlus dopant source was used to dope the silicon with boron at a surface.

**Doping process**

Boron doping on a standard Si wafer used in this research was performed using high temperature solid diffusion method. The doping process was carried out either at the first stage of fabrication process or after release of Si aperture. The boron doping at first step of fabrication is useful for conductivity increment of electrode as well as wet etch stop application. Boron doping after release of aperture makes the silicon membrane a good conductor as compared to the metal. The doping process is same for both the cases and performed in a quartz tube furnace.

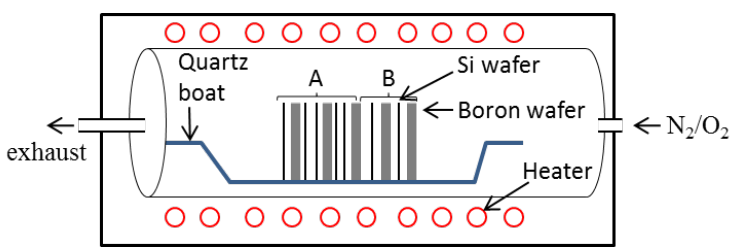


**Fig. 3.19** A layout of boron doping process in a quartz tube furnace. Boron get diffused into nearby Si wafer at high temperature which make the Si surface conductive.

An experimental setup for the boron doping process is illustrated in Fig. 3.19. Si wafers to be doped at single face were loaded as in A in a quartz boat by facing boron source at only one surface of Si wafer. For both side doping, an alternate

Si and boron wafers were loaded as in B facing both surfaces of Si towards the boron sources.

Fig. 3.20 presents photographs of quartz tube furnace and wafer loading on a boat with cross sectional illustration of doping at single face and double faces of Si wafers. The photograph (Fig. 3.20 (a)) shows quartz tube on operating condition (temp. 1150 $^{o}$C), gas inlets for $N_2$ and $O_2$, and electronic heater controller. For single side boron doping (as in A) and double sides doping (as in B) wafers were loaded on quartz tube as shown in Fig. 3.20 (b). In this research, single side boron doping was carried out on bare standard p-Type wafer at the first step of fabrication (Fig. 3.20 (c) and both sides doping was done after release of Si aperture (Fig. 3.20 (d)).

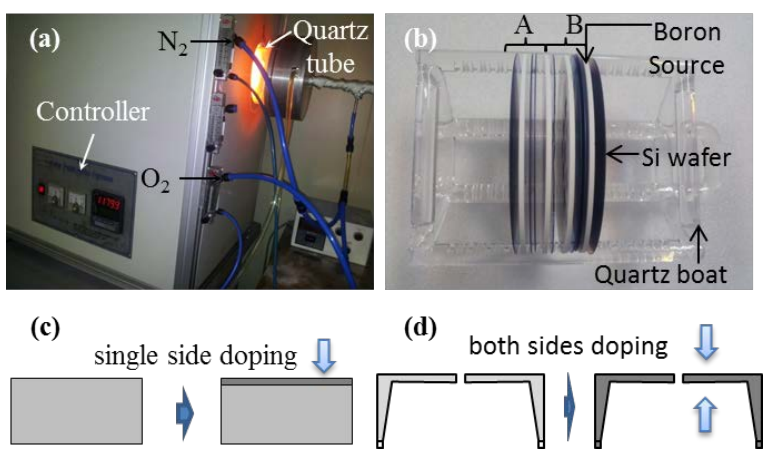


**Fig. 3.20** Photographs and schematics representation of boron doping process. (a) A photograph of furnace at operating condition. (b) A photograph of wafer loading for single side and double side boron doping. (c-d) Schematics of single side (c) and double sides (d) doping.

If the doping is done at the beginning of fabrication, the boron doped epilayer can be used as a wet etch stop too. But it is not beneficial for making relatively

thicker Si membrane because the boron doped layer is normally shallow (~1 μm). Hence, boron doping was carried out at the end of the aperture released so that the membrane can be truly used as an electrode with better electric conduction.

After proper inserting the quartz boat loaded with wafers to be doped, an electronic program set to control the furnace heater as given in recipe (Fig. 3.21) was run. The boron doping was done at high temperature 1150 $^{o}$C for 7 h, so that the boron diffusion depth in Si wafers would be several micrometers and the doping concentration would be as high as possible. An inert gas $N_2$ was supplied throughout the process so that dopant could be transported to the Si wafers steadily and uniformly. About 1% $O_2$ was also supplied to form a glassy layer $B_2O_3$ on the Si surface and enable deeper boron dopant diffusion. This sort of recipe would dope charge concentration ~ $1\times10^{20}$ $cm^{-3}$ giving resistivity ~0.001 ohm.cm.

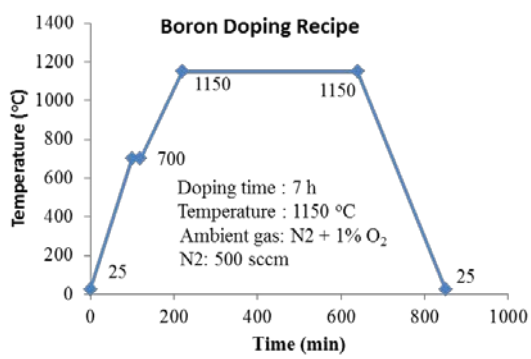


**Fig. 3.21** A recipe for boron doping. The graph shows the temperature variation with time and used of ambient gases.

## 3.10 Anodic Bonding

The bonding of MEMS substrates has been performed by three distinct techniques: direct, intermediate layer, and anodic bonding. Direct bonding requires stringent clean and flat surfaces to be bonded and high temperature annealing to establish high strength bonding [89, 90]. Intermediate layer bonding requires additional layer deposition on a substrate to be bonded that reduces the annealing temperature. The last technique bonds substrates with the application of moderate voltages (~200 – 1000 V) and temperature (~200 – 500 $^{o}$C) [91, 92]. It is also known as electrostatic bonding, field-assisted bonding or Mallory bonding [93, 94]. This bonding technique is applicable to many MEMS substrates, for instant, Si-glass, Si-Si, glass-glass, Si-Al, $SiN_x$-$SiO_2$ etc [92, 95-97]. The quality of anodic bonding depends upon voltage, temperature, nature of surfaces to be bonded, cleanness, nature of material, and the bonding time [98-101].

This research presents an anodic bonding of heavily boron doped p-type silicon membrane with borosilicate Pyrex chip. The bonding process was performed for bare Si, thermal oxidized and PECVD deposited $SiO_2$, and LPCVD deposited $Si_3N_4$ with Pyrex glass at atmospheric pressure. With the slight amendment of the bonding parameters, quite satisfactory results were obtained with all the substrate. For example, the voltage should be high enough (~1000 V) for Si substrate with oxide and nitride coated surface at a relatively higher temperature (~450 $^{o}$C). The lower voltage and lower temperature were sufficient for bare Si substrate. In another words, if the temperature and voltages are kept same, the bonding time increases in ascending orders from Si (p-type)

< poly Si < $Si_3N_4$ < $SiO_2$ in order of approximately 1:5:12:20 for the borosilicate Pyrex glass substrate [99].

### 3.10.1 Bonding mechanism

Anodic bonding is a physico-chemical process in which $NaO_2$ excited and dissociated at high temperature and the positive ($Na^+$) and negative ($O^{2-}$) ions moves towards the cathode and anode with the application of electric filed (Fig. 3.22). The ions cross the interfaces of the substrates to be bonded and undergo the chemical reaction. The reaction forms a sandwich layer of thin $SiO_2$ (~10 nm) [99] which permanently bonds the substrates together. It is irreversible process which bond strength is as high as ~25 MPa which is comparable to the bonding of glass itself [91].

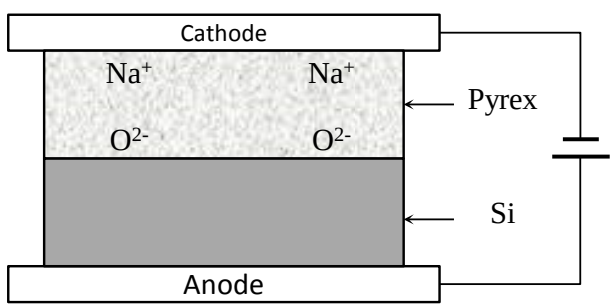


**Fig. 3.22** A schematic of anodic bonding circuit connection and direction of flow of ions. The accumulation of ions near to the interface produce strong electric field that bonds the Pyrex and Si due to formation of thin layer of $SiO_2$ at their interface.

This phenomenon can be further explained as the image charge formation mechanism. When $Na^+$ ion drifts to the cathode, $O^{2-}$ ions remains at the glass side of the Si-glass at which a space charge region is formed. This in turn creates an equivalent positive charge (image charge) on the Si side of the Si-glass

interface, resulting high electric field (~1 MV/cm) across the Si-glass interface. Under the high electric field the $O^{2-}$ ions are drifted away from the $Na^{+}$ depletion region to the Si surface. When $O^{2-}$ ions meet Si atoms, an electrochemical reaction is occurred and a thin silicon oxide layer is formed at the interface. The oxidation rate depends upon the availability of $O^{2-}$ ions and strength of electric field at the interface. Stronger electric field enhances the oxidation rate reducing bonding time. Surface cleanness and smoothness contribute higher oxidation rate by increasing the contact area between two surfaces to be bonded. As a consequence of formation of oxide layer at the interface, both the substrates get permanently bonded.

### 3.10.2 Bonding setup and method

The bonding system is comprised of a hot plate with temperature controller, a DC power supply together with electrodes, micropositioner, and a load controller spring (Fig. 3.23 (a)). Pre-cleaned fabricated thin membrane lens-electrode was gently positioned on the hot plate before heating the plate avoiding the thermal and mechanical stress on the Si membrane. The small mechanical force or little thermal stress may break the membrane. Then, pre-fabricated Pyrex chip was placed on top of membrane and aligned as shown in Fig. 3.23 (b)). 16 align keys in a circle of diameter 2.5 mm were used to align the Pyrex with an aperture diameter 3 mm. Then, a cathode connected with a spring was positioned just above the Pyrex chip and gently down till it slightly press the Pyrex on the Si surface. The intensive care is required while bringing down the cathode considering tolerance level of Si membrane. The electric circuit was

connected as shown in Fig. 3.23 (c) and the assembly was heated to 400 $^{o}$C. The hot plate temperature almost exponentially (fitting line) increases and remains steady to the temperature (Fig. 3.23 (d)) set in the controller. A DC voltage was applied to the electrodes (Fig. 3.23 (c)), ensuring a negative electrode potential on the Pyrex side with respect to the Si surface.

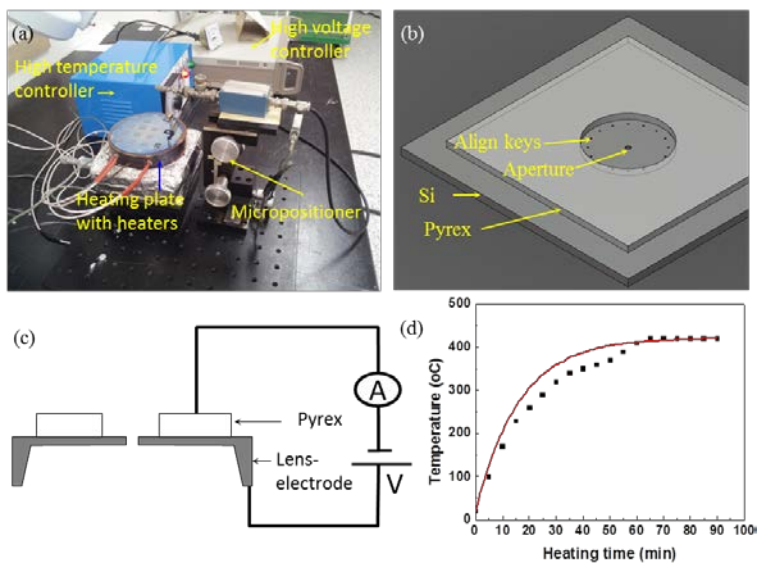


**Fig. 3.23** Experimental setup for anodic bonding. (a) A photograph of bonding setup. A fabricated lens-membrane wafer on a hot plate, micropositioner, and temperature and voltage controllers are seen. (b) A schematic drawing of Pyrex chip aligned on lens-membrane sample. (c) An electric circuit for anodic bonding of Pyrex and lens-electrode. (d) Temperature rises of hot plate with heating time at room environment.

The potential was increased gradually till the ammeter reading shows a few mA. The potential required to show the current flow depends upon the conductivity between bonding surfaces. For instance, higher potential is required for the oxide or nitride deposited silicon surface than bare silicon surface. Impurities in Pyrex chip increases the conductivity which lowers the potential required for bonding, however bad insulator are not good to use as spacer

between lens-electrodes. The electric potential was applied till the bonding completed. There are two immediate indicators which confirm the bonding. First, the bonding current drastically drops down and remains constant or zero. Second, the interface between Si and Pyrex looks like filled with wet layer. The bonding process normally completed within 5 to 20 minutes depending upon the applied voltage, temperature, surface cleanness, and material between bonding surfaces.

### 3.10.3 Bonding results

Anodic bonding between Si and Pyrex glass has been performed for several samples fabricated in a wafer (Fig. 3.24 (a)). The Pyrex chip lying on the Si wafers are anodically bonded lens-electrodes. The interface of the Si-Pyrex looks paper-wet-color which is significant of the complete bonding. Pyrex chip were degreased in acetone, methanol, and DI water for several minutes before proceeding the bonding. The bonding current as a function of time is illustrated in Fig. 3.24 (b). A drastic current drop was observed in a first minute of bonding start. Most of the cases, bonding current down to zero or reaches a steady within 1-2 minute indicating the completion of bonding. The higher current in beginning is due to surge of $Na^+$ ions drifted to the cathode. As the migration of $Na^+$ ions continues, the accumulation of positive charge repels the incoming ions and the current reaches a steady state or zero at a completion of bonding. For the assurance of bonding, electric potential was supplied for at least 5 minute though the interface looks bonded and current became steady or zero. The peak current

and drop down rate not only depend upon the applied potential but also depend on temperature and nature of bonding surfaces.

Fig. 3.24 (c) and (d) illustrate Si-Pyrex bonding interfaces at complete bonding and partial bonding cases. The bonded Pyrex appeared wet on the surface as no air remains at the interface between the surfaces (Fig. 3.24 (c)). The bonding was done at 400 $^{o}$C, with application of 600 V for 5 min.

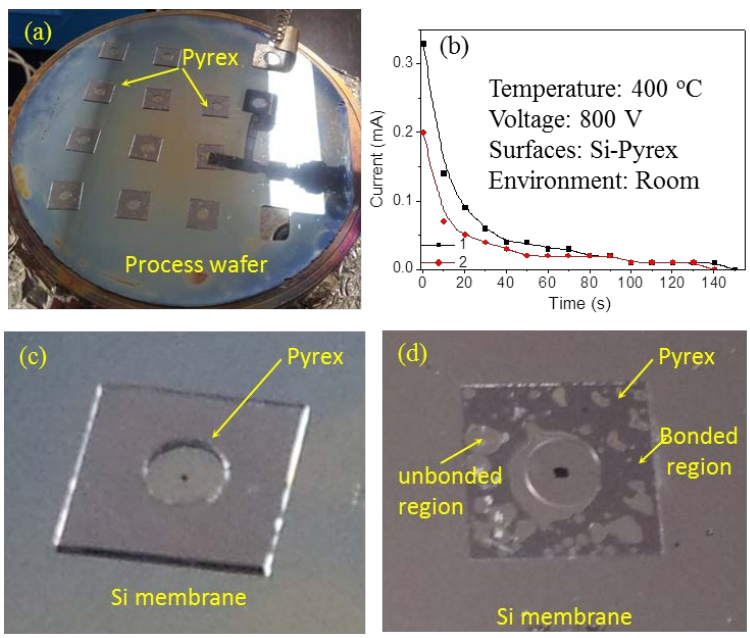


**Fig. 3.24** Si-Pyrex anodic bonding. (a) A photograph of process wafer of which several membrane samples have been bonded with Pyrex chip. (b) Pot of current as a function of time during bonding process. Photographs of Si-Pyrex (c) complete bonding and (d) incomplete bonding.

The photograph resembles the completed anodic bonding of Si-Pyrex. Another photograph (Fig. 3.24 (d)) shows the incomplete bonding of Si-Pyrex. There are several transparent white spots resembling unbonded regions. This process was done same as before but temperature down to 200 $^{o}$C. The

temperature seemed to be not sufficient to mobilize the $Na^+$ ions at Pyrex zone, that lower the bonding current and oxidation rate, consequently, incomplete bonding. Even after 2 hr of bonding process, there were still several unbounded voids indicating heat is one of the essential requisites for anodic bonding. Hence, all the bonding process was carried out at temperature ~400 $^oC$ and bonding voltage >500 V for bonding satisfactory.

The quality of Pyrex-Si bonding is important for two purposes: first, to hold the thin Si membrane with the support of Pyrex chip, second, to provide void-free separation between conducting and insulating media. Fig. 3.25 presents SEM images of cross section of a lens-electrode and Si-Pyrex bonding interface.

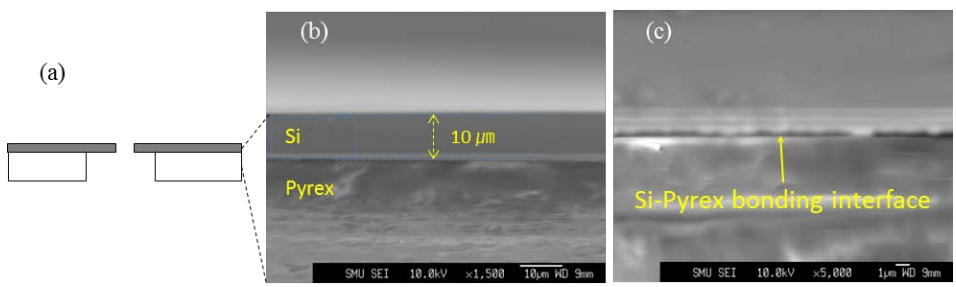


**Fig. 3.25** Schematic and SEM images of cross section of Si-Pyrex bonding interface. (a) Schematic of a lens-electrode. (b) SEM image of cross section of Si membrane and Si-Pyrex interface. (c) Magnified SEM image of Si-Pyrex bonding interface.

The Si membrane thickness was measured to be ~10 μm (Fig. 3.25 (b)) and length/width 8/8 mm equal to the size of Pyrex chip. The SEM image of interface of Si-Pyrex bonding revealed that the contact between the Si and Pyrex is in sub micrometer range (Fig. 3.25 (c)). The bonding results seems to be satisfactory to use the Pyrex bonded Si membrane as a lens-electrode for source/Einzel lens assembly.

## 3.11 Release of lens-electrode

The lens-electrode fabrication process was completed with the safe separation of Si-membrane bonded with Pyrex chip. Although the Si membrane thickness is very thin (~10 μm) and large (10 mm × 10 mm), it is first supported with bulk Si later Pyrex chip holds the membrane after bonding of Pyrex chip on it. Fig. 3.26 illustrates a schematic diagram of a Si membrane with Pyrex bonding before and after detachment of lens-electrode from wafer. A slight force was applied using a pointed tweezers at the two edges of Pyrex as shown by broken lines around the edges of Pyrex in Fig. 3.26 (a). With the slight mechanical force, the Si membrane got broken along the <100> orientation revealing an individual lens-electrode. This process is not required for lens-electrode made of Si membrane supported by bulk Si itself because the membrane area is too small for this type of lens electrode.

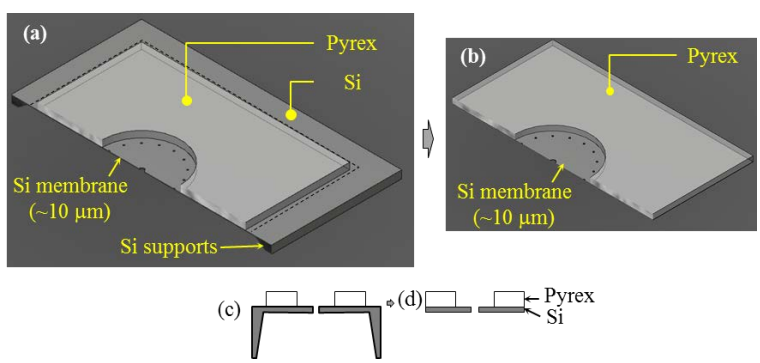


**Fig. 3.26** A cross section views of lens-electrode before and after detachment from wafer. (a) Bonding of Pyrex on Si membrane. (b) An individual lens-electrode. (c-d) schematics of lens before (c) and after (d) detachment. It releases the lens-electrode of thin Si membrane supported by Pyrex.

## 3.12 Multiple lens-electrodes alignment

The precise alignment of multiple lens-electrodes is one of the most critical factors that determine overall performance of the microcolumn system including the e-beam aberration and resolution. The major source of beam aberration is thought to be origin from the lens especially due to misalignment of apertures. In an attempt to precise alignment of multiple apertures with sub-micrometer accuracy, expensive and complicated aligner is being used; however still difficulty to carry out the precious alignment.

Optical alignment technique (e.g., mask aligner) is probably widely used technique. But its alignment accuracy is limited to 1–2 μm because of limits in micrometer screws used to position the stages although the theoretical limit is half of wavelength of the light.

Self-aligned field emitter-scanning tunneling microscopy (SAFE-STM) [102] is regarded as a precious alignment technique in which STM is used to align a field emission tip with respect to a microlenses. An electronic feedback circuit control the emission stability and piezo electric transducer (PZT) control the precious alignment of lens-aperture with the emitter (Fig. 3.27) [17]. This system needs to be performed in ultra-high vacuum with the electron emitter and monitoring the electron beam with the help of Faraday cage. The alignment system is based on the maximum current flow which may sometime mislead to the aperture alignment if the emission is not stable.

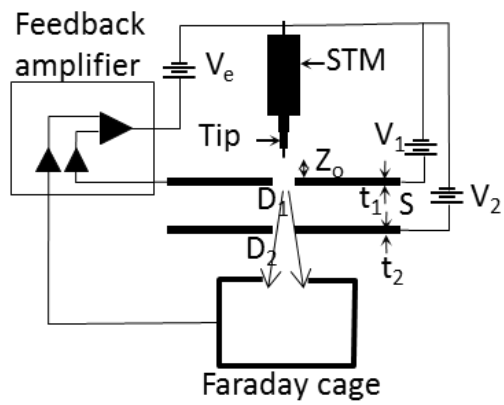


**Fig. 3.27** A schematic diagram showing microlenses alignment using SAFE-STM.

Laser diffraction alignment technology is newly developed alignment method that promise to align sub-micrometer precision [50]. Importantly, this technique is simple and can be performed at atmospheric dark room without any aid of other sophisticated expensive apparatus. Fig. 3.28 illustrates a schematic concept of multiple lenses alignment using laser diffraction technique. The circular diffraction pattern remains symmetry in shape and light intensity if multiple apertures are aligned along the optical axis. The Fig. 3.28 shows two lens-apertures alignment passing the laser beam through them and producing a circular diffraction patterns indicating good alignment of the apertures along the optical axis. This research follows the laser diffraction alignment method for aligning multiple lenses.

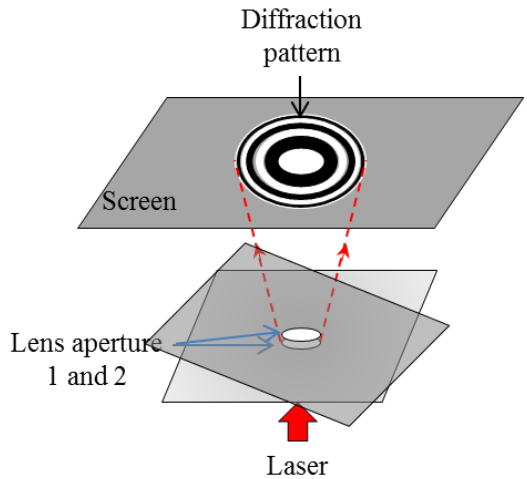


**Fig. 3.28** An illustration of laser diffraction multiple lenses alignment technique. A symmetric circular diffraction patterns is observed if multiple circular apertures are coaxially aligned.

### 3.12.1 Principle of laser alignment technique

When light passes through a smaller circular aperture comparable to the wavelength of light, the light diffracts forming circular airy patterns. Alternate bright and dark circular patterns are formed as given by the well-known diffraction formula:

$$sin\theta = \frac{m\lambda}{d} \qquad 2.3$$

Where, d is diameter of aperture, m is given as 1.220, 2.233, 3.238 …. for dark pattern and 1.635, 2.679, 3.69…. for bright pattern and λ is wavelength.

When two apertures are in parallel along the optical axis, the circular symmetry of the diffraction pattern retains only if they are perfectly aligned, otherwise

distorted patterns are observed. By observing the pattern symmetry, one can judge the alignment of two apertures.

### 3.12.2 Lens alignment process

An s-polarized He-Ne laser (λ = 633 nm) and a set of precision (100 nm resolution) linear stage is used to align multiple lens-electrodes. The first diffraction pattern was observed with an aperture of the first lens and second lens was positioned in parallel to the first with the help of 3D stage positioner (Fig. 3.29). When both the aperture was coaxially aligned along the optical axis, similar diffraction pattern was re-observed.

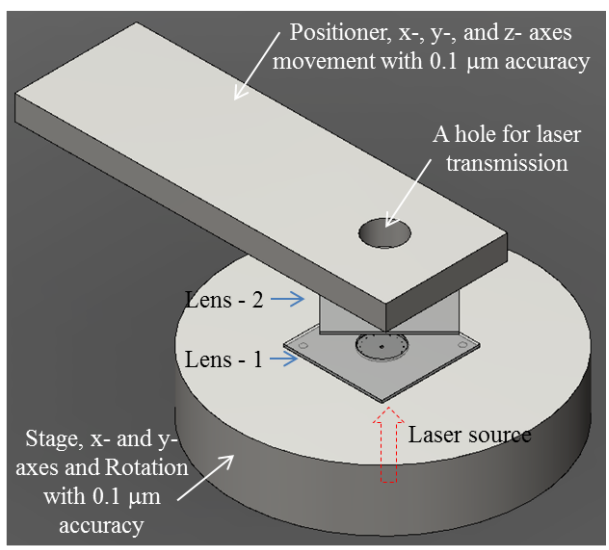


**Fig. 3.29** A schematic illustration of lens alignment using laser diffraction technique. A stage with micropositioner enables to align the micron size apertures with precision of 0.1 um.

If the alignment is perfect, the pattern appeared symmetric and same as in the first pattern. A little misalignment gives the distortion in the patterns. The

distorted patterns look non-circular, non-symmetric, non- uniform distribution of light intensity, and overlapping of bright and dark patterns. The second lens was positioned with the help of stage micropositioner till the symmetric circular diffraction patterns are re-observed. Then, the second lens was lower down till it get contact with first one and gently pressed it over other, ensuring no extra force and just contact each other. A non-conducting carbon free epoxy was put at three corners of joints between lenses which take around an hour to bond them permanently.

Without disturbing the alignment setting, another lens was aligned along the optical axis and by observing the similar diffraction pattern and bond them. Fig. 3.30 illustrates a schematic view of three lens-electrodes alignment for source or Einzel lens structure. With the multiple lens alignment, the diffraction pattern may appear faint than before especially when the aperture dimensions different due to diffracted energy loss while travelling from one lens to another.

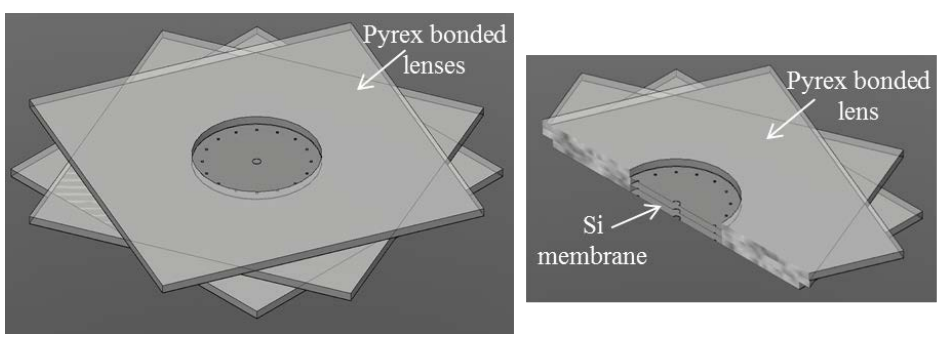


**Fig. 3.30** Schematic diagrams of lens alignment. (a) 3D view of alignment of three lenses. (b) A cross section view of an aligned lens structure.

The accuracy of diffraction is very crucial which accuracy should be checked. A transmission optical microscopy was used for the alignment test. Individual

image of the lens-apertures was taken by focusing one by one along the same vertical axis. For it, stage or sample should be fixed and only the vertical motion of the objective lens should be moved up and down to focus the individual apertures. The images were compared putting together along an axis for the misalignment calculation. For it, one of the lens apertures was taken as reference and others are calculated for the misaligned from the optical axis.

### 3.12.3 Alignment results

Lenses in electron optical system are mainly categorized into two types according as their functions. A lens is used near to the electron source which function is to extract, accelerate, and limit the beam waist, hence commonly known as source lens. The source lens is mainly composed of two or more lens-electrodes having different apertures size. In this research, source lenses having three or four lens-electrodes were fabricated and their performances were evaluated. The apertures used in the source lens are asymmetry in size. For instant, lens aperture size of an electrode near to emitter, called extractor in case of field emission tip, is maintained around a few micrometer to a few tens of micrometer; middle electrode, called accelerator, has wide aperture (few tens to hundred micrometer); and last electrode through which e-beam exits limits the beam waist therefore called limiting aperture and has only a few micrometer in size.

In case of Einzel lens, multiple lens-electrodes of symmetric apertures in size are used for focusing an e-beam. If the Einzel lens is made of three electrodes, the outer two electrodes are normally kept in same electric potential so that e-

beam experiences antagonistic force at entering and exiting side. However, the middle electrode is biased either positively or negatively that are named as an accelerating and a decelerating focusing mode, respectively. Hence, this lens is also called, a unipotential or an objective lens.

According to lens applications, both source and Einzel lenses have been assembled following the method described in previous sub-section.

#### *3.12.3.1 Einzel Lens Alignment*

An Einzel lens composed of three lens-electrodes with symmetric apertures were aligned following the laser diffraction technique. The first lens-electrode was placed on aligner stage facing upside down and observed a diffraction patterns through an aperture, ensuring that the laser beam focused at the center of the aperture. Second lens-electrode was then placed facing upside down and rotating ~22$^{o}$ on the top of the first and it was aligned along the optical axis with the help of a vacuum positioner. When both the apertures were coaxially aligned similar diffraction patterns could be observed without any distortion in circular pattern.

As the apertures are symmetric and same size, the intensity and pattern size remains same. After gluing them third lens also similarly aligned and then glued (Fig. 3.30). The diffraction patterns observed through single, double and triple symmetric lens-apertures aligned along the optical axis is shown in Fig. 3.31. The photographs were captured with some angle with the direction of laser. The position and orientation of three lenses L1, L2, and L3 were as shown in Fig. 3.31.

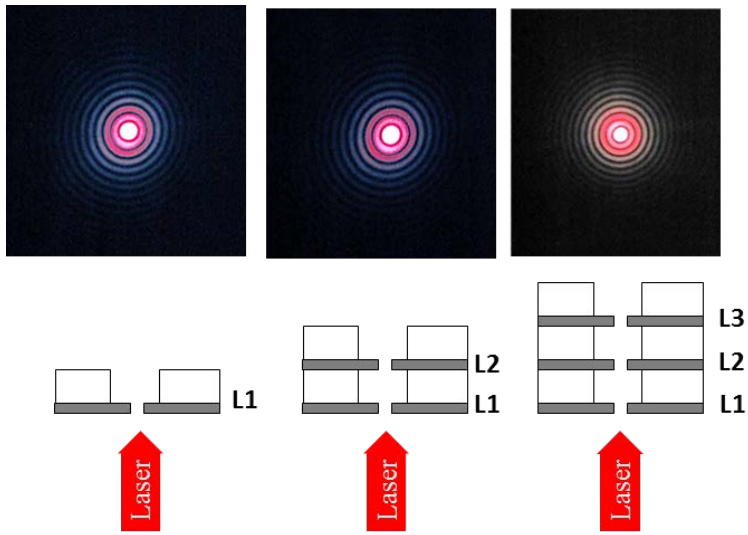


**Fig. 3.31** Diffraction patterns acquired through single, double and triple coaxially aligned symmetric circular lens-apertures. The diameters were measured as 200 μm. L1, L2, and L3 are first, second and third lenses.

The schematic of Einzel lens structure completed by alignment of three lens-electrodes is shown in Fig. 3.32 (a). The overall thickness of lens structure is ~0.5 mm if 150-μm Pyrex is bonded with the thin Si membrane lens-electrode. A schematic top view of lens structure with the glue positions is presented in Fig. 3.32 (b). The Schematic represents the possible rotation of the lenses with respect to each other. The lenses are rotated so that corner of each lens-electrodes can be used for wire bonding. Fig. 3.32 (c) shows a photograph of completed Einzel lens.

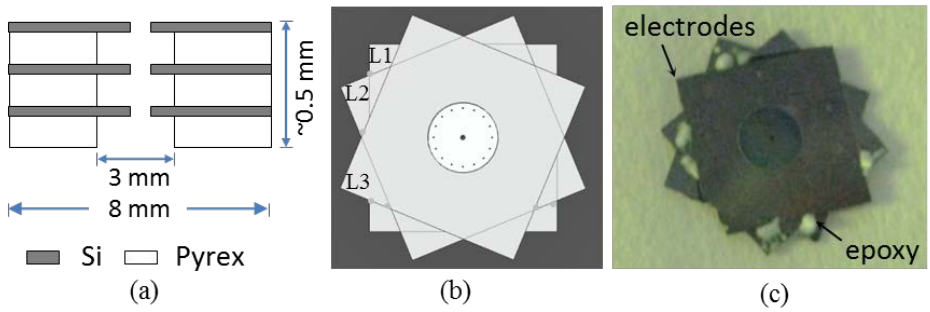


**Fig. 3.32** Cross section, schematic, and photograph of Einzel lens alignments. (a) Cross section (b) A schematic of Einzel lens alignment. (c) A photograph of Einzel lens aligned using laser diffraction technique

Optical images were taken as explained in previous section and presented in Fig. 3.33. The optical images are aligned horizontally and vertically (Fig. 3.33) to calculate misalignment of the aperture from the optical axis. Two apertures L2 and L3 seemed to be aligned perfectly, however, due to misalignment of L1 the overall misalignment is measured as 1.67 μm. The detail of misalignment calculation (table of Fig. 3.33) shows that the axial deviation of L1/L2, L1/L3, and L2/L3 are 2.51, 2.51 and 0.0 μm. The overall misalignment seems to be at the range of the resolution of optical microscopy at the optical magnification 200× at which images are observed. For the comparison, SEM images of the corresponding lens-apertures are also presented in Fig. 3.33 which shows the circularity of the aperture.

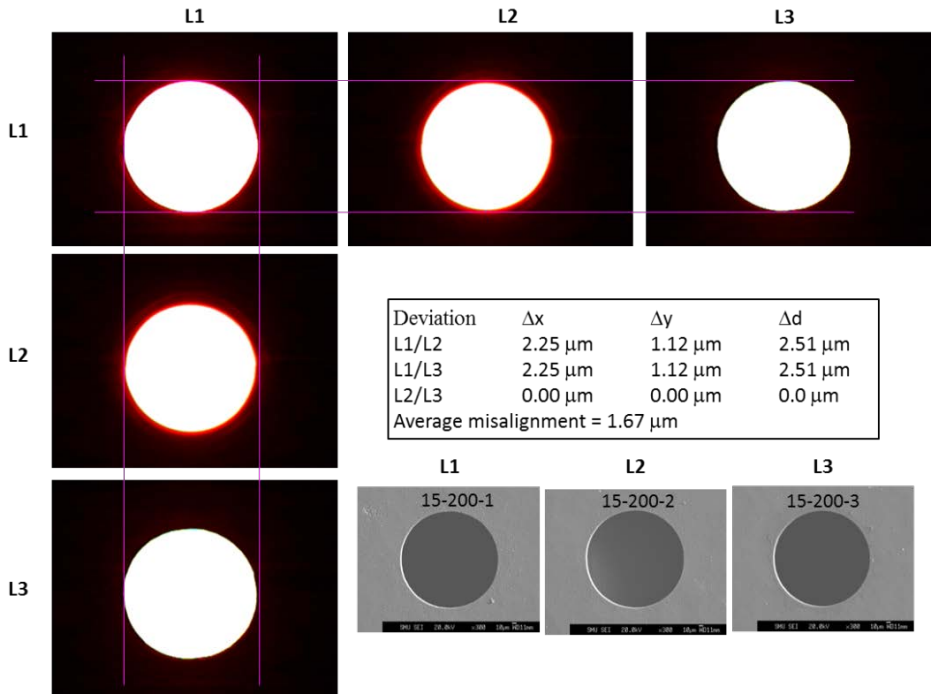


**Fig. 3.33** Transmission optical images of Einzel lens aligned using diffraction patterns technology for alignment precision test. L2 and L3 are accurately aligned but L1 seemed a bit misaligned that results average misalignment ~1.67 µm. SEM images of corresponding lens-aperture also presented.

### *3.12.3.2 Source lens alignment*

The source lens, 100-100-20 µm were aligned and its misalignment was calculated as explained below. Similar to Einzel lens alignment, the first source lens, S1, was positioned on the laser path and diffraction pattern was observed as in the first image of Fig. 3.34 (c). The second lens, S2, was positioned with rotation of ~ 22$^{o}$ and then aligned the aperture parallel to first along the optical axis and observed the diffraction pattern as in second image of Fig. 3.34 (c). Here, the second photograph was taken at nearby screen (~50 cm) whereas the first one was taken at far distance screen (~300 cm). So, more patterns are seen

along with some noise. After bonding them, third lens, S3, was position by rotating 45$^{o}$ to the first, and aligned its aperture along the optical axis and the diffraction pattern was observed as in third image of Fig. 3.34 (c). The third image could not cover large number of patterns as in before and the intensity was sharply reduced because of the smaller aperture size (20 μm). It is a consequence of high diffraction ($\theta \propto d^{-1}$) and low intensity ($I \propto d^{-4}$) of light through small aperture [103].

To test the alignment precision, transmission optical images of lens-apertures were obtained by focusing individual lens-electrodes and presented in Fig. 3.34 (a). Two identical aperture of size 100 μm seemed to be aligned well but the smaller aperture (20 μm) seemed to be shifted out of axis giving overall misalignment ~12 μm. The detail of misalignment calculation is presented in Fig. 3.34 (b). This sort of higher misalignment was occurred due to poor judgment in locating highest intensity of laser beam passing through uneven aperture size. When uneven sized apertures are aligned, observing only the diffraction pattern is not sufficient. If the smaller aperture is inside the optical field of bigger aperture, the diffraction patterns are clearly seen and not affected by the position of the smaller aperture. But the beam intensity is slightly changes with the position. Maximum intensity is observed when the smaller aperture is exactly at the optical axis. Thus, the alignment should be performed on the basis of the maximum intensity and shape of diffraction pattern in case of uneven apertures.

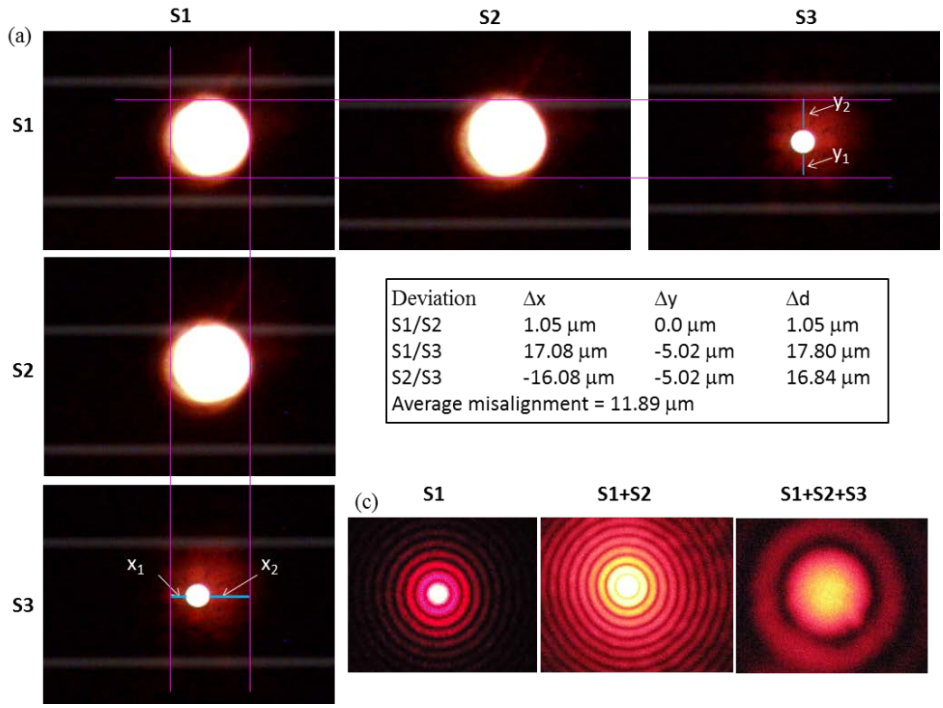


**Fig. 3.34** Transmission optical images of a source lens aligned following the diffraction pattern technology. (a) Optical images of source lenses, S1, S2, and S3 arranged vertically and horizontally to calculate misalignments. (b) A table of misalignment calculation. (c) Diffraction patterns observed through single S1 aperture, double, S1 + S2 apertures, and triple, S1 + S2 + S3.

### *3.12.3.3 Four lenses alignment*

Following the same technique as explained in previous sub-sections, four lenses of aperture sizes 50, 50, 50, and 10 µm have been aligned. First, three identical apertures were aligned and then smallest one was aligned. The schematic of the lens structure is shown in Fig. 3.35 (c).

First, three identical lenses have been aligned following the similar method as described in previous sub-sections. The photographs of diffraction patterns obtained from the lens L1, L1+L2, and L1+L2+L3 are almost similar except

decrease in intensity. When fourth lens of aperture size 10 μm was aligned on top of them, the intensity of diffraction pattern was highly reduced though the diffraction patterns were observable. The fourth lens was aligned allowing for the maximum light intensity and symmetric diffraction pattern (Fig. 3.35 (d)).

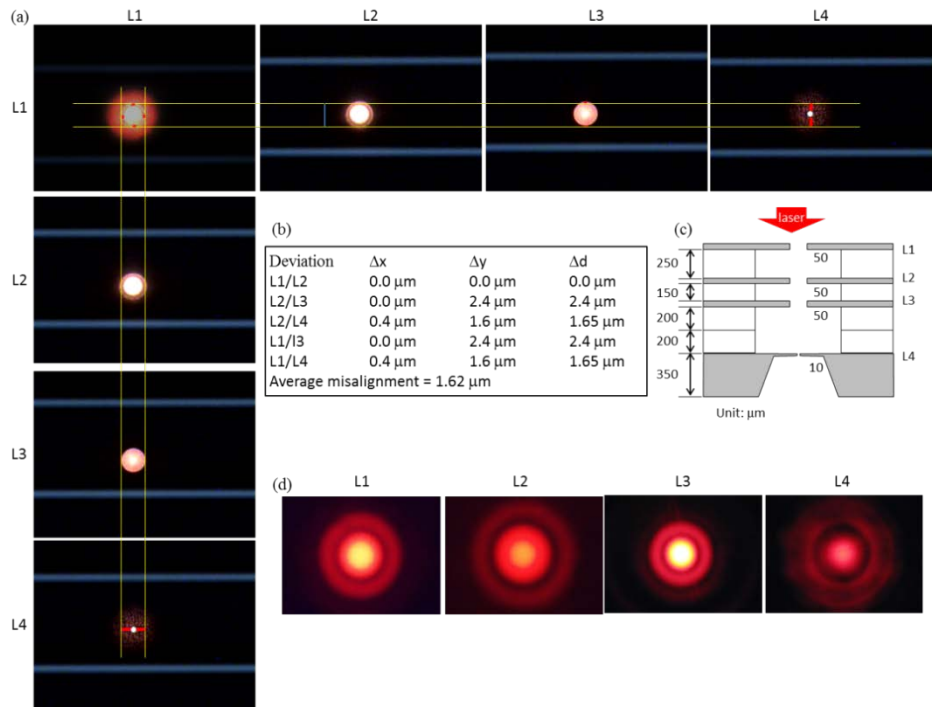


**Fig. 3.35** Four lenses alignment following diffraction technology and the misalignment check using transmission optical microscopy. (a) Optical images of four lenses along an optical axis. Horizontal and vertical arrangements of images for misalignment calculation. (b) Misalignment calculation results. (c) A schematic of lens structure. (d) Diffraction patterns formation when laser passes through single, double, triple and quarter lenses.

After the completion of bonding all of the four lenses, transmission optical images were taken for individual lenses as presented in Fig. 3.35 (a). The images are arranged along the horizontal and vertical direction in order to calculate the

misalignment. The results are tabulated in Fig. 3.35 (b). The results show that all the four lenses are almost precisely aligned with the accuracy ~1.6 μm.

## 3.13 Microcolumn assembly

An assembly of full microcolumn is one of miniaturized job which is performed with series of processes such as alignment of tip and source lens, source lens and Einzel lens, and positioning deflectors in symmetry. Following subsections described step wise processes of an assembly of a full microcolumn.

### 3.13.1 Tip and source lens assembly

A field emitter tip and an electrostatic source lens were aligned using optical alignment method. The source lens was first mounted in a cylindrical holder and then a tip was gently screw down by aligning its position along the optical axis. For the three dimensional alignment, two optical microscopes positioned perpendicular to each other are used in imaging the tip distance as well as the position of tip. Typical optical images of tungsten tip and source lens aligning along x- and y-axes are shown in Fig. 3.36 (a). Mirror images of the tip are also seen at the bottom of the picture. The image presents tip - lens distance 44.4 μm and mismatch of axes of tip and optical axis of lens by 2.5 μm. Fig. 3.36 (b) and (c) show the SEM image of typical field emission tungsten tip showing tip diameter ~100 nm.

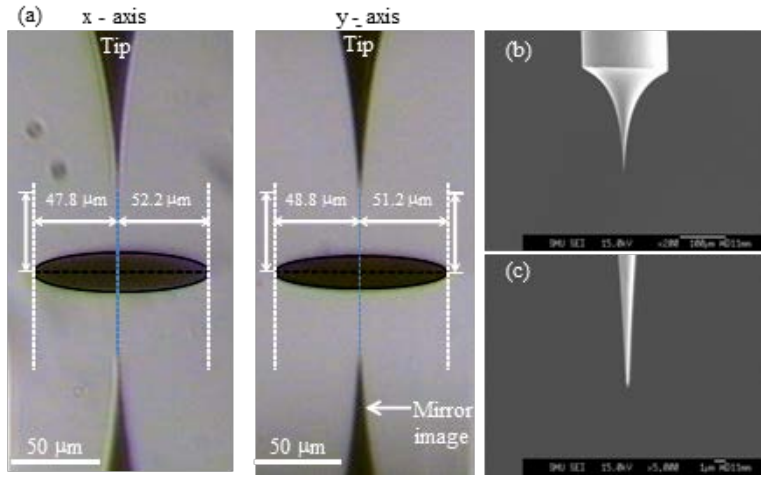


**Fig. 3.36** Tip source lens alignment. (a) Optical images of tip and source alignment view from x- and y- axes. (b) SEM image of a typical tungsten tip. (c) Magnified view of the tip.

### 3.13.2 Einzel lens and deflector assembly

Source lens and Einzel lenses were aligned following the line of sight method, however the accuracy of alignment is lower than laser diffraction technique. A photograph of aligned source and Einzel lenses mounted in a cylinder is shown in Fig. 3.37 with wire connections.

**Fig. 3.37** A photograph of deflector and Einzel lens alignment with wire connections.

### 3.13.3 A complete column assembly

Afore mentioned sets of aligned tip-source lens and deflector-Einzel lens were aligned and assembled with the help of optical microscopy. Then, a sample of Cu grid was positioned under the Einzel lens. All of the components were aligned along an optical axis and rotational symmetry. A schematic and a photograph of a microcolumn assembly is shown in Fig. 3.38. The length of column is measured to be ~ 6 – 10 mm excluding the wire connections.

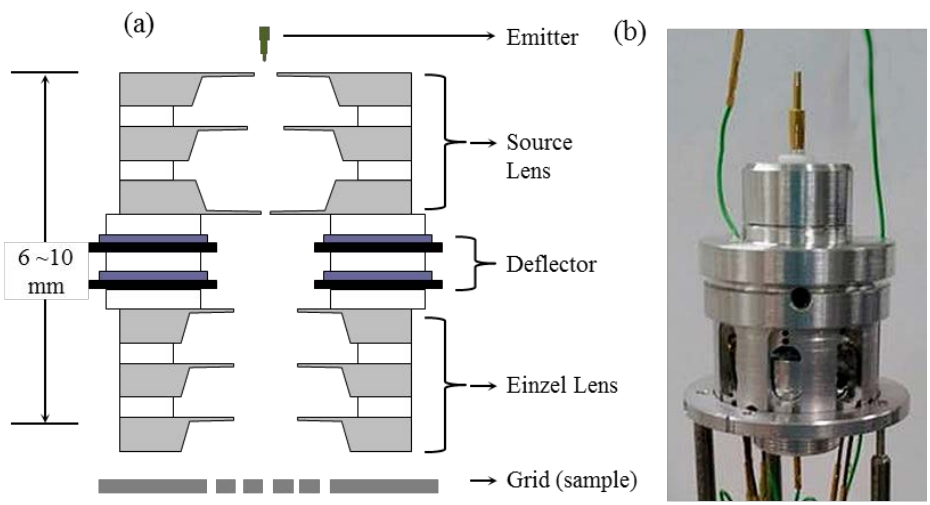


**Fig. 3.38** A complete microcolumn assembly. (a) A schematic of complete microcolumn. (b) A photograph of fully assembled microcolumn.

# 4 CHAPTER IV: CHARACTERIZATION OF A MICROCOLUMN HAVING DIFFERENT EINZEL LENS STRUCTURES

An electrostatic lens system designed and fabricated in this research was assembled with electron beam emitter and deflectors. The microcolumn here presented is two lenses systems: source lens and objective lens, however the operation mode may be one-lens or two-lenses focusing mode. Mode of microcolumn operation is illustrated in Fig. 4.1. One-lens focusing mode may be either source lens (Fig. 4.1 (a)) or Einzel lens focusing mode (Fig. 4.1 (b). In case of Einzel lens focusing mode, the electric potential is applied either positive or negative to the center lens-electrode with respect to the two equipotential outer lens electrodes. The positive electric field enhances the speed of an e-beam hence called accelerating mode and opposite of it is called decelerating mode. Both modes are equally useful in focusing e-beam at a particular point however the aberration of the beam is different. In two-lenses focusing mode, both the source and Einzel lenses are applied to designated electric potentials to bring an e-beam at a focal point (Fig. 4.1 (c)). In addition, deflectors or scanner can be used for a beam stigmation, wide field of view, and image magnification. It is notable that (field emission) tip voltage is always negative and normally ranges from -100 to -2000 V.

The performance of two sets of microcolumn assembled with two different Einzel lens structures were evaluated and analyzed their influence on scan ranges. The two sets are identical except the Einzel lens structures. Type-W

microcolumn has a set of an Einzel lens with gap between electrodes 500 μm whereas the Type-N has only 150 μm.

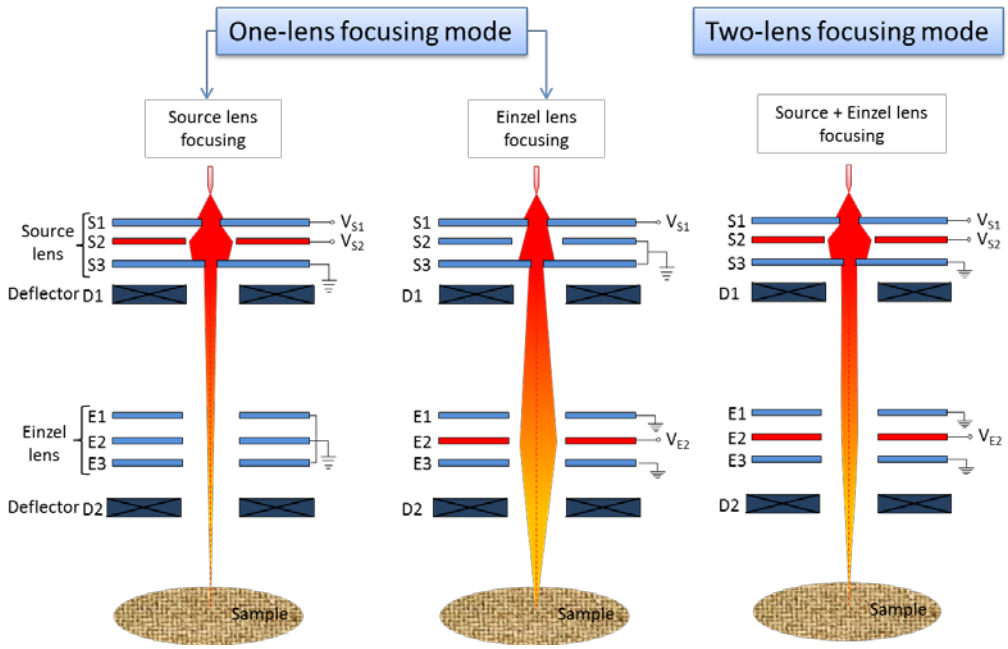


**Fig. 4.1** Microcolumn mode of operations. One-lens focusing mode (a) Source lens focusing mode, (b) Einzel lens focusing mode. Two-lens focusing mode (c) combined source and Einzel lens focusing mode.

## 4.1 One-lens focusing mode

### 4.1.1 Source lens focusing mode

Electron beam emitted from emitter can be focused on a sample without any additional potential on objective lens. All the electrodes of Einzel lens is grounded here and the e-beam is manipulated or focused by potential applied on source lens especially on S2. A typical example of source lens focusing mode is

illustrated in Fig. 4.1 (a) where potentials are applied on tip, S1, and S2. Rests of electrodes are grounded as shown in Fig. 4.1 (a).

The microcolumn assembled for characterization is described in brief as follows: It is assembled with source lens with identical aperture sizes of 100 μm with gap between S1-S2 and S2-S3 are 500 μm and 850 μm, respectively. In case of the Einzel lens structure, all the electrodes are identical with aperture size 200 μm and gap 500 μm (Type-W) and 150 μm (Type-N). For scanning the beam over the sample, and correct the stigmation, one or two quadrupole deflector was used. A series of experiments were performed at three tip voltages: -200, -300, and -400 V and four sample positions: 2, 3, 4, 5, and 7 mm from last lens-electrode of the Einzel lens. Setting particular deflector voltages, sample current electron micrographs of a Cu grid were acquired by optimizing source voltages for the best imaging condition. For safe operation, compiler current for S1 lens-electrode was set to 100 nA and current at other electrodes were also recorded for example tip, S2 and E1 currents.

**Tip voltage -200 V**

Surface current electron micrographs of Cu grid sample were acquired at tip voltage -200 V as presented in Fig. 4.2 for Type-N microcolumn. Note that S2 voltage was unaltered at -175 V and the best imaging condition were acquired with the adjustment of S1 voltage, however S1 current was set to compiler current -100 nA. It was noticed that tip current fluctuated about 9 nA with average 134 nA. Extractor voltage S1 needed to be set at -118 ± 4.7 V which fluctuated the S2 current 26.5 ± 6.26 nA. Because of the scattering of electron beam, some of the beam was just bombarded on the first Einzel lens which was

observed by the E1 current measurement, however it was low. The measured current was 0.14 ± 0.17 nA. The E1 current was higher when deflector voltage was high which made the beam oscillate far and more beam strike on the E1. When deflector voltage was set to low potential difference, the beam would not oscillate with large amplitude and the E1 current read almost zero.

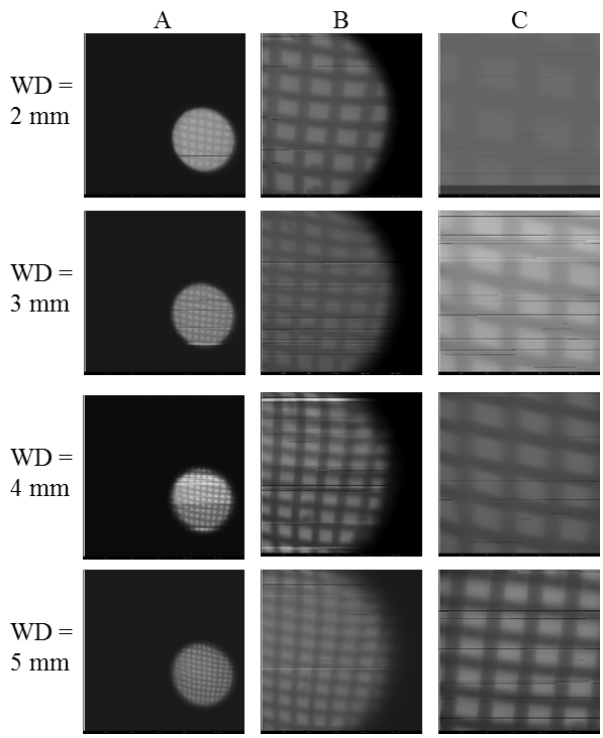


**Fig. 4.2** Sample current electron micrographs acquired at tip voltage -200 V. Rows represent micrographs at magnification defined by deflector voltage condition given in Table 4.1. Columns represent micrographs at working distances 2, 3, 4, and 5 mm.

Images appeared clear at lower magnification but unclear at high magnification with limiting the beam deflections. It indicates that beam aberration increases with higher magnification. To find the scan range for a particular working distance and magnification at fixed tip voltages, the visible

mesh were counted and plotted as scan range versus working distance as presented in Fig. 4.3.

**Table 4.1** Deflectors conditions. D1-D4 are four poles of a deflector.

| Deflector range | D1 | D2 | D3 | D4 | Range (V) |
|---|---|---|---|---|---|
| A | 10 | -10 | 10 | -10 | ± 100 |
| B | 4 | 10 | -6 | 0 | ± 30 |
| C | 3 | 6 | -4 | -1 | ± 15 |

The plot shows that the scan range increases with the increasing working distance. A-C represents image magnification in ascending order which deflector voltage conditions are as described in Table 4.1. Scan range is higher at the low magnification for a particular working distance.

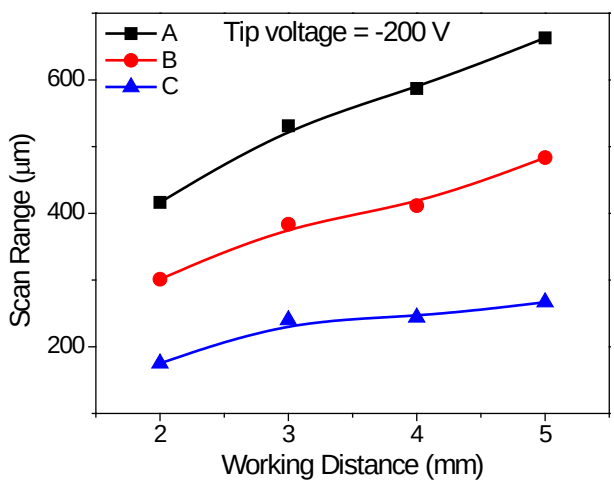


**Fig. 4.3** Scan range versus working distance at tip voltage -200 V. Scan range increases with working distance for all sort of the magnification. The increment trend is almost linear.

**Tip voltage -300 V**

Surface current electron micrographs were acquired at different working distances adjusting S2 voltages at tip voltage -300 V. S2 is set to -269 V for all the operations. The electron micrographs are presented in Fig. 4.4.

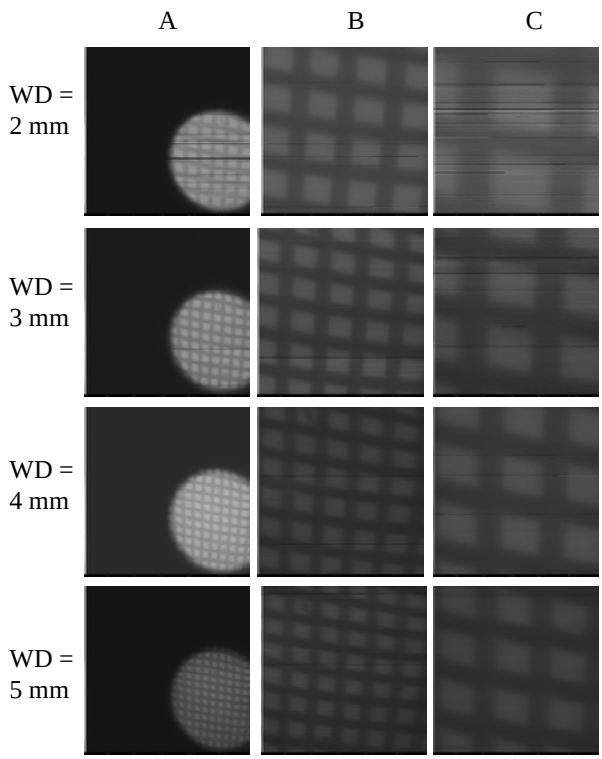


**Fig. 4.4** Sample current electron micrographs acquired at tip voltage -300 V. Rows represent micrographs at magnification defined by deflector voltage condition given in Table 4.1. Columns represent micrographs at working distances 2, 3, 4, and 5 mm.

Electron micrographs in rows were acquired with different deflector setting as described in Table 4.1 and in column were with working distances fixed at 2, 3, 4, and 5 mm. The meshes are clearly distinguishable when deflection ranges are large that is at low magnification. With increasing magnification, the images of meshes became blurred. It can be attributed as the results of high aberration

with the increasing magnification. Of important, the no of meshes appears more when the working distance increases. It is plotted in a graph of the scan ranges versus working distance presented in Fig. 4.5. It shows that the scan range is almost linearly increases with the working distance. It indicates linear path of e-beam when the beam is outside of external field.

The image quality seems to be improved and clear resolved images were observed. Mesh number increases with increasing working distance.

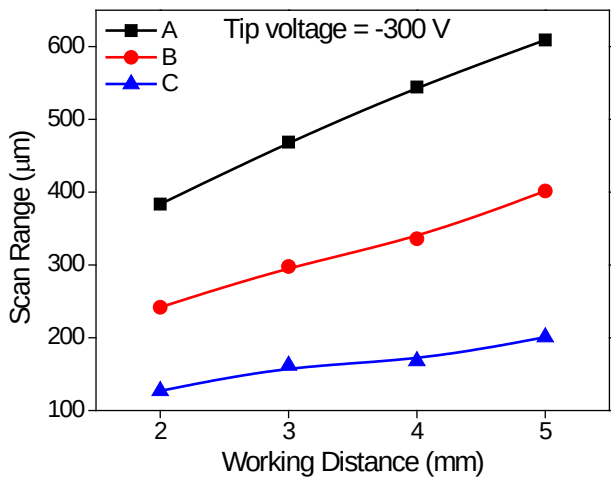


**Fig. 4.5** Scan range versus working distance for tip voltage -300 V.

### Tip voltage -400 V

The microcolumn was also operated at tip voltage -400 V as described in previous section. The surface current electron micrographs are presented in Fig. 4.6. The images were acquired at working distance 2, 3, 4, and 5 mm and at image magnification given by quadrupole deflector's potential difference as described in Table 4.1. The row (A-C) represents the increasing magnification of the image and column show the increasing working distance.

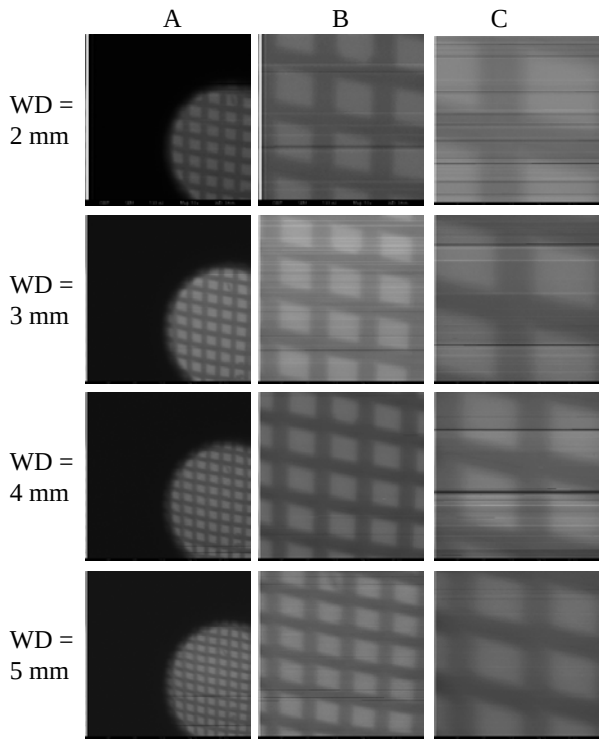


**Fig. 4.6** Sample current electron micrographs acquired at tip voltage -400 V. Rows represent micrographs at magnification defined by deflector voltage condition given in Table 4.1. Columns represent micrographs at working distances 2, 3, 4, and 5 mm.

At tip voltage -400 V, the images appeared clear and well resolved than previous lower tip voltage images. The images were acquired at S2 voltage -361 V with S1 voltages -322 ± 8.69 V. Tip current was measured as 122 ± 2.46 nA which is lowest in compared with the operation at previous tip voltages. The current reading at S2 and E1 are also lowest among the previous given as 13.7 ± 1.8 nA and 0.09 ± 0.15 nA.

Scan range appeared almost linearly increased with working distance for all the magnification.

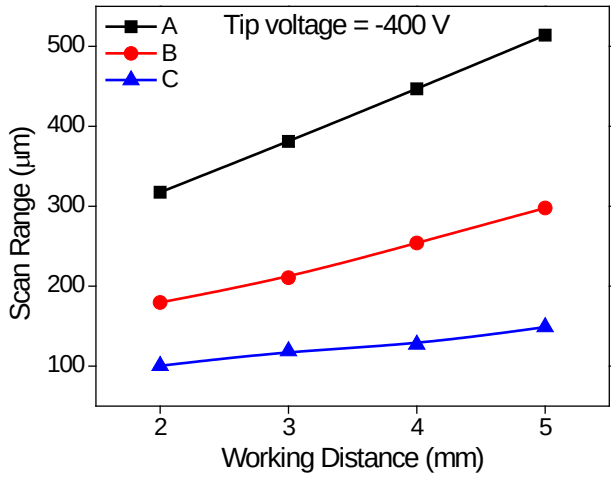


**Fig. 4.7** Scan range versus working distance at tip voltage -400 V.

A noticeable thing about a scan range is: it goes decreasing with the increasing tip voltages. It seems that with the increased tip voltage, lower the scattering of e-beam, hence, we see sharp image though the field of view is small at higher tip voltages.

Type-W microcolumn was also operated with at tip voltages -200, -300, and -400 V in source lens focusing mode. The surface current micrographs were acquired with full deflection voltages at working distance 7 mm (Fig. 4.8). The images shows that magnification occurred at higher tip voltage however the visible meshes are almost same as depicted in plot Fig. 4.8 (d). The variation of the scan range with the tip voltages is almost negligible.

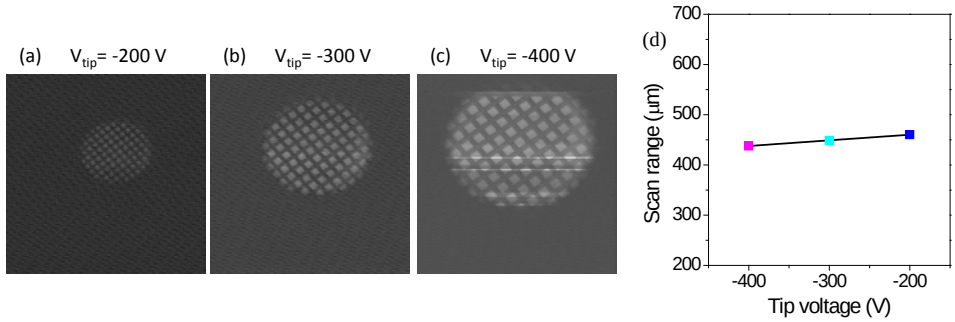


**Fig. 4.8** Sample current electron micrographs and a plot of scan range versus tip voltage from Type-W microcolumn. The deflector voltage was set to 100 V. Images acquired at tip voltages (a) -200 V, (b) -300 V, and (c) -400 V. (d) A plot for scan range versus tip voltages.

### 4.1.2 Einzel lens focusing mode

Microcolumn was also operated by applying potential on middle electrode (E2) of Einzel lens and rests of the electrodes were grounded except the e-beam extractor. As the focusing of beam is done by only the Einzel lens, the mode of focusing is called Einzel lens focusing mode (Fig. 4.1 (b)). A surface current electron micrograph acquired at Einzel lens focusing mode is shown in Fig. 4.9. The image was acquired at tip voltage -300 V, E2 = 411 V while S1 = -79 V. Even we tried for different focusing voltage; the image looks fuggy as in figure. It seems that Einzel lens alone could not focus the e-beam on the sample. Thus, combined source and Einzel lens focusing mode was executed and the results are presented in the preceding section.

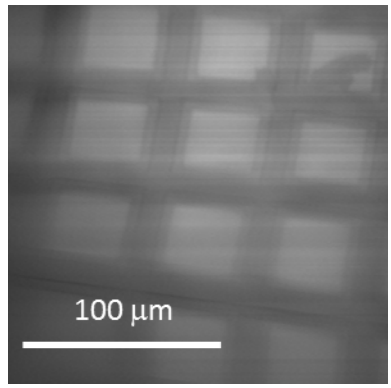


**Fig. 4.9** An electron micrograph acquired at Einzel lens focusing mode.

Type-W microcolumn gave sample current electron micrographs as presented in Fig. 4.11 when operated in Einzel lens focusing mode. The images are cleared and well-focused. The images (a) to (d) are acquired at same deflection voltage but at different tip voltages. A plot for scan range versus tip voltage shows that the scan range linearly increases with the reduction of tip voltages (Fig. 4.10). The increment of scan range at low voltage can be attributed as the higher deflection of lower speed e-beam with application of same electric force.

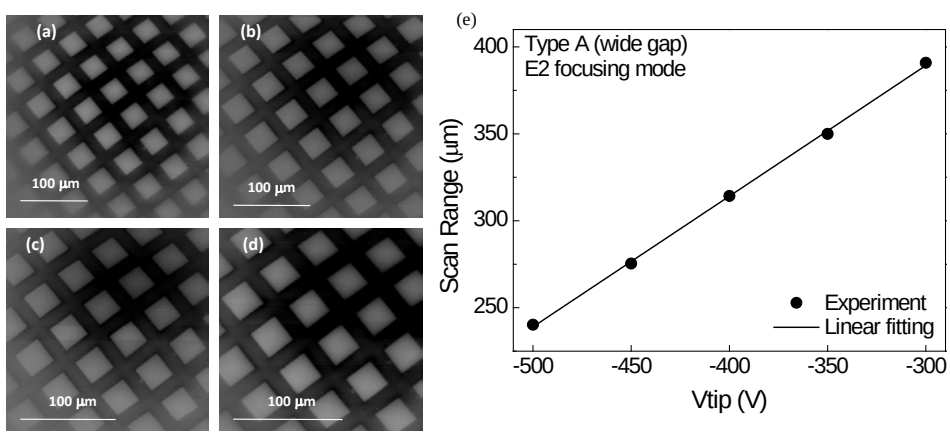


**Fig. 4.10** Sample current electron micrographs acquired using Type-W microcolumn at different tip voltages in E2 focusing mode and a plot of scan range versus tip voltages.

The images (a-d) were acquired at tip voltages -300, -350, -400, and -500 V. (e) A plot of scan range versus tip voltages. The line is linear fitting line.

## 4.2 Two-lenses focusing mode

A schematic representation of two-lenses (combined source and Einzel lens) focusing mode is illustrated in Fig. 4.1 (c) where potentials are applied to both the source lens as well as Einzel lens in order to focus the beam on a sample. The e-beam is controlled by both the S2 and E2 voltages and their combined efforts on bringing the beam at a single point. Surface current electron micrographs were acquired by adjusting both the S2 and E2 along with S1 voltages for the better resolution.

### E2 optimization

The microcolumn was operated at tip voltage -300 V and S2 voltage was fixed to -267 V, E2 voltage was optimized for best imaging for two deflector conditions. The deflector conditions are (a) +10, -10, +10, and -10 V and (b) -0.5, +8.5, -1.5, and +7.5 V on the quadrupole deflector. The surface current electron micrographs acquired at those conditions are presented in Fig. 4.11. Here, E2 voltage was step wise increased from 0 V to 247 V in deflector condition first (Fig. 4.11 (a)) and 0 V to 250 V by 50 V per step in condition second (Fig. 4.11 (b)). The image acquired at 30 V and 50 V seems to be better than other in case of deflector condition (a). It means, the optimized image may be at E2 = 40 ± 10 V for S2 = -267 V for deflector condition (a). In case of next deflector condition (b), the image looks sharp and clear when E2 = 100 V or 150

V. It shows that the optimized E2 voltage may be 125 ± 25 V for S2 = -267 V for deflector condition (b).

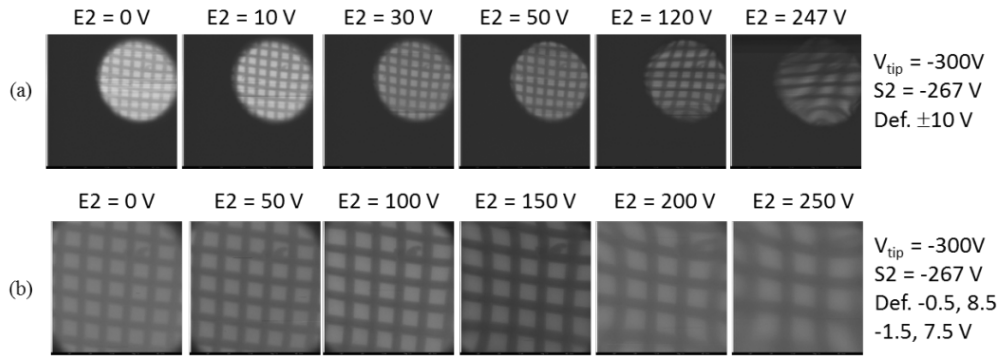


**Fig. 4.11** E2 optimization for the best surface current electron micrograph for fixed S2 voltage.

### S2 optimization

For the S2 optimization, two E2 voltages were selected, 250 and 300 V. The electron micrographs were acquired with tip voltage -300 V at quadrupole deflector condition (-0.5, 8.5, -1.5, and 7.5 V). The S2 potential is very sensitive that ~1V variation changes the image quality as presented in Fig. 4.12. Here, S2 voltages increased from -263 V to -267.1 V at E2 voltage fixed to 250 V. some spherical aberration was observed when beam seems to be focused at sample surface at S2 voltages -264 to -265. With further increase in S2 voltage made beam out of focus. The optimized beam seems to be 264.5 ± 0.5 V. But for the case of higher E2 voltage (300V), most of the image shows large aberration (Fig. 4.12). It is noted that the E2 voltage here is same as the tip voltage. It seems that the column should be operated with lower E2 voltage than tip voltage.

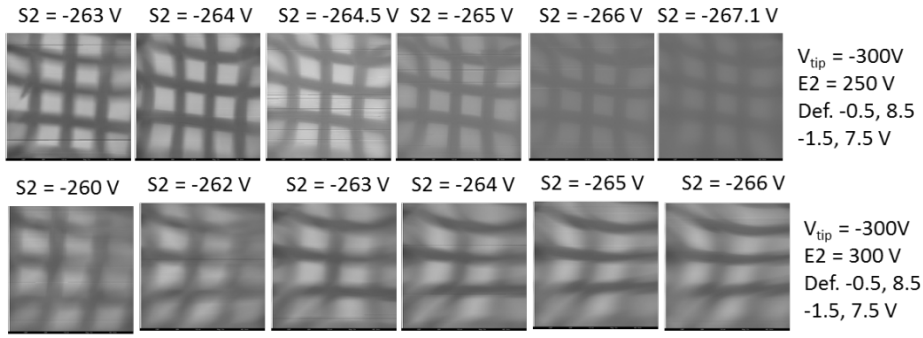


**Fig. 4.12** S2 optimization for the best surface current electron micrograph for fixed E2 voltage.

### S1 variation

From the experiments described in previous section, it seems that the optimized value of S2 and E2 lies in between -264 V and 250 V respectively. To notice the variation in S1 voltage with the optimized S2 and E2 voltages, while adjusting complier current is fixed for S1. Here, S2 and E2 were selected at -264 V and 250 V, respectively. The S1 voltage varied from -220 V to -233 V with the step of ~2 V. The deflector condition was selected as in previous S2 and E2 optimization case. The surface current electron micrographs are presented in Fig. 4.13. The effect of S1 is not as sensitive as S2 variation, the image quality seems to be almost same.

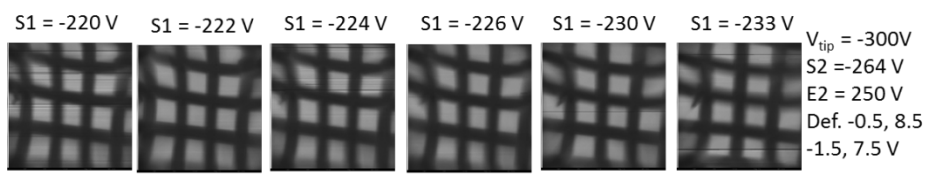


**Fig. 4.13** S1 variation for the best surface current electron micrograph for fixed E2 and S2 voltages.

This chapter discussed about the three focusing modes of microcolumn operation: Source lens, Einzel lens, and combined Source and Einzel lens focusing modes. At source lens focusing mode, potential is applied to S2 electrode to control the e-beam inside the microcolumn keeping rests of electrodes grounded except the extractor. At this mode, the column was operated at three tip voltages: -200, -300, and -400 V for four working distances: 2, 3, 4, and 5 mm at five scanning ranges defined by deflector voltages. The surface current electron micrographs were acquired at different conditions of microcolumn operation and compared for the scan ranges. For all the cases, the scan range increases with the increase in working distance. The scan range also reduces with the increasing the negative tip voltages.

Einzel lens focusing mode seems to be not suited for this microcolumn because none of the Einzel lens voltage could give clear image. It may need to be further optimized the Einzel lens voltage with the source lens voltages or gap between the Einzel lens electrodes needs to be optimized.

Combined source lens and Einzel lens focusing mode seems to be best choice for the better image quality because both the source lens and Einzel lens can be optimized for the better image quality. The optimized source (S2) and Einzel (E2) lens voltage lies in ~-264 V and 250 V at the tip voltage -300 V. S2 voltage seems to be very sensitive, with the variation of ~1 V voltage changes the image quality significantly. The effect of S1 voltages in the case of optimized S2 and E2 has little influence in image quality.

# 5 CHAPTER V: RESULTS AND DISCUSSION

The performance of microcolumn is predominantly affected by the electron optical lenses; for example, for a fixed working distance, chromatic aberration decreases linearly with spacing between electrodes, whereas spherical aberration reaches an optimum value [17]. However, there are still several technical challenges in achieving larger field of view with better resolution.

I investigated the effects of gap between electrodes in Einzel lens structure on field of view and image quality. The image is precariously affected by perfectness of electrostatic lens which includes geometrical shape and perfectness of aperture, accurate alignment of multiple apertures, and optimization of electrode thickness and gap between electrodes [2]. Pyrex supported Si membrane lens design is presented in chapter II with computer simulation for electric field distribution and e-beam trajectories inside the microcolumn with modified lens structures. Successful fabrication of the lens design is presented in chapter III following MEMS fabrication technique. The fabricated lenses have been assembled in a microcolumn which performance evaluations have been discussed in chapter IV. The Pyrex supported Si membrane lens design allows choosing wide range of thickness in both electrode and Pyrex starting from few to several hundred micrometers. Two Einzel lenses with gap between electrodes 150 and 500 μm were assembled in two different identical microcolumns and representatively named, for simplicity, as Type-N and Type-W, respectively.

Using both types of microcolumn, sample current electron micrographs were acquired with emitter tip voltages -200, -300, and -400 V and deflector voltage up to ± 100 V at working distance from 2 to 7 mm in source lens (S2) focusing mode as described in chapter IV. The experimental data of scan ranges acquired from both types of columns is plotted in Fig. 5.1.

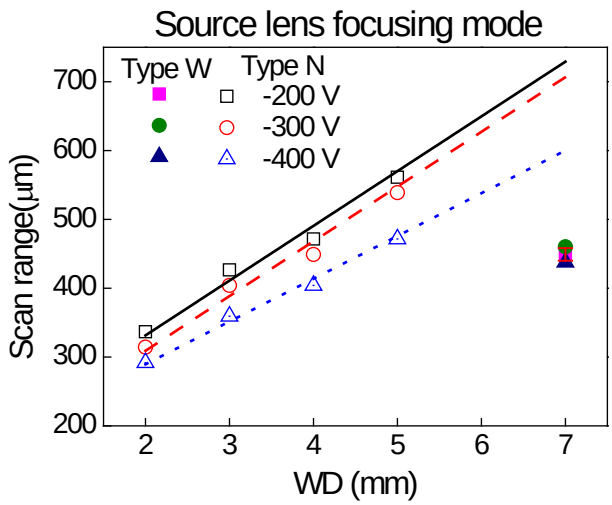


**Fig. 5.1** A plot of experimental data of scan range versus working distance (WD) at tip voltages -200, -300, and -400 V for Type-W and Type-N microcolumn system.

The open and solid symbols represent scan range acquired from Type-N and W, respectively. The solid lines represent linear fitting to the data points with corresponding color which is extrapolated up to 7 mm of working distance (WD). The slopes for linear fitting lines are measured as 71.84 ± 6.35, 71.84 ± 6.35, and 58.37 ± 3.17 μm/mm for -200, -300, and -400 V, respectively. The plot depicts that scan range increases almost linearly with WD in case of Type-N and also higher for lower negative tip voltage. For the case of Type-W, the scan ranges are not significantly different with variation of tip voltages. The extrapolated scan ranges of Type-N column based on linear fitting lines exhibit

that the Type-N column has larger scan range than the Type-W column at 7 mm of WD.

To compare the effects of gap in another mode of operation, both the columns are operated in Einzel lens focusing mode where electric field is applied on only E2 and rest of electrodes are grounded. The clear and resolved electron micrographs were acquired by the column with Type-W Einzel lens structure (Fig. 4.10 (a-d)) but images were not clear from other column (Fig. 4.9). The scan range increases linearly with the reducing the negative tip voltages as presented in plot Fig. 4.10 (e). The increment is measured as $0.704 \pm 0.036$ μm/V from linear fitting line. It means, larger scan range can be achieved at lower negative tip voltage though the image fades at edges.

In contrary, with the Type-N column at Einzel lens focusing mode, the electron micrograph looks fuzzy, and dragging out (Fig. 4.9). The micrograph was acquired with E2 at 411 V, allotting other electrodes grounded. The fuzzy image resembled that electron beam seems to be disturbed and could not be focused at the sample. To understand this undesired result, a computer simulation was re-performed with 2D model of Einzel lens system with varying gap between electrodes for evaluation of electric potential/field distribution inside the lens system (Ref. section 2.4 for details). The simulation results of electric potential distribution are presented in Fig. 5.2 (a-d) which illustrate the surface plot with contour of electric potential at Einzel lens system for gap between electrodes 150 (Type-N) and 500 μm (Type-W) with aperture size 200 μm. For simulation, 100 V was applied only on the central electrode (E2) and rests of electrodes (E1 and E3) were grounded.

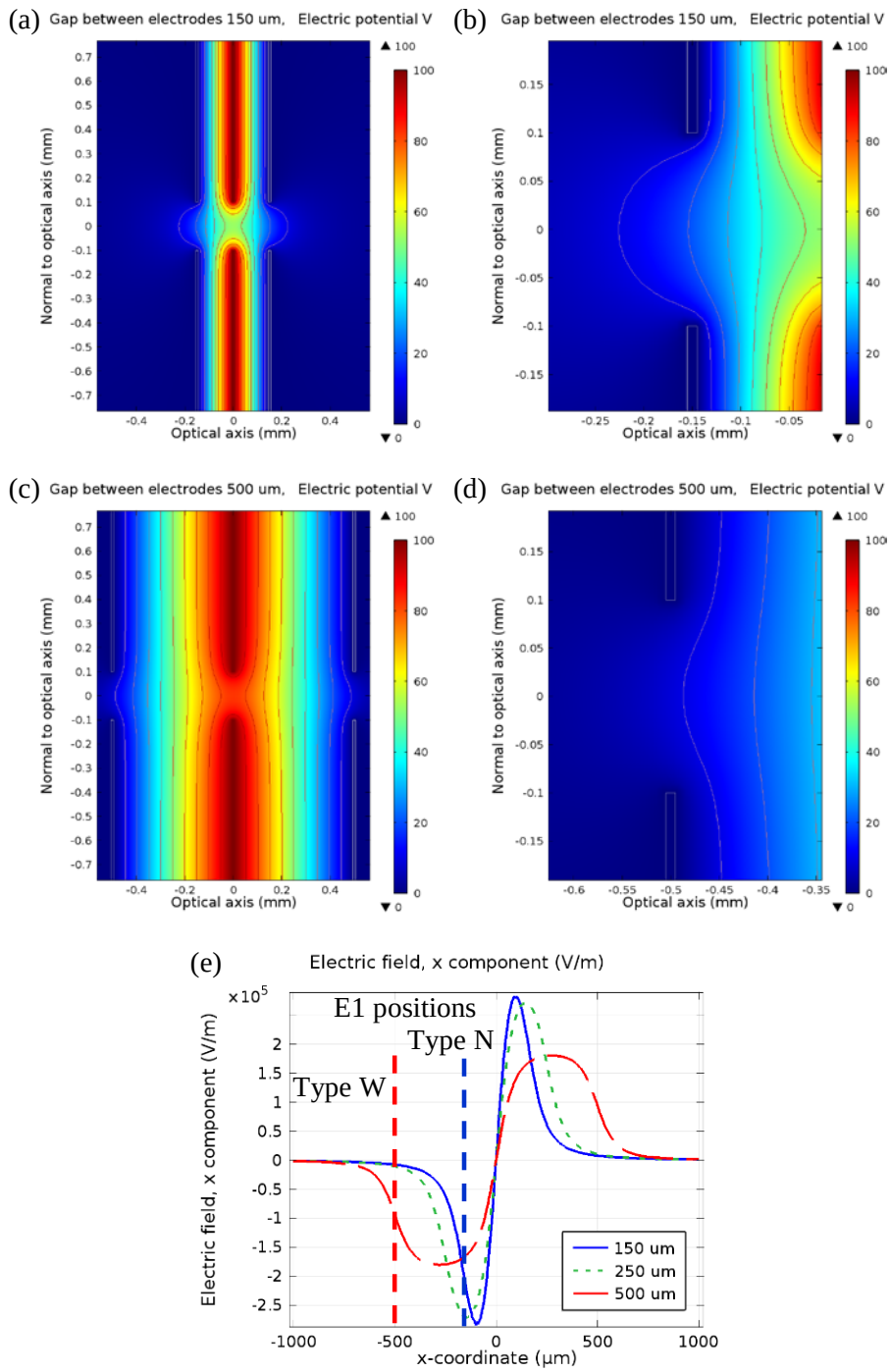


**Fig. 5.2** A surface plot of electric potential and line plot of electric field across optical axis on 2D modeling of Einzel lens system for varying gap between lens-electrodes. (a)

and (b) for gap 150 μm (Type-N). (c) and (d) for gap 500 μm (Type-W). (e) Line plot of x-component of electric field intensity along the optical axis (x-coordinate) passing through center of lens for gap between electrodes 150, 250, and 500 μm. Red and blue vertical broken lines show the position of E1 for Type-W and Type-N Einzel lens.

The plot displays that electric potential decreases outwards from central electrode (represented by contours lines at interval of 5 V) and there is a sharp decrease in 150 μm than 500 μm which is more noticeable at optical axis. Conspicuously, the electric potential prolongs out through nearby apertures beyond the first and third electrodes in Type-N (Fig. 5.2 (b)) whereas the electric potential is restrained inside the Einzel lens system in Type-W (Fig. 5.2 (d)). The variation in electric field distribution is evidently realized in the line plot along the optical axis (Fig. 5.2 (e)) with the variation of gaps. Electric field strength displays point symmetry with respect to the center position of E2: zero at E2 position and two extreme values nearly at the mid of two electrodes. Importantly, the extreme value becomes larger as the gap gets smaller. For example, the maximum electric field strength for d = 150 μm is 0.285 MV/m, while that for d = 500 μm is 0.180 MV/m. The electric field sharply increases quite far from E1 position and reach at peak in between E1 and E2 electrodes with Type-N whereas with the Type-W, it is steadily increases and the peak value remains around 60% of the Type-N. These results indicate that we can get strong electric field by narrowing the electrodes separation with the same lens voltage. The electric field beyond the E1 or E3 for Type-N is so strong which interferes with the field generated by nearby electrodes (e.g., deflector). Due to the interferences of fields, the beam focusing is difficult and could not make noise-free and results

blurry image. Hence, I performed the two-lens focusing mode for better image quality and larger scan range.

Combined source and Einzel lens focusing mode was conceded with Type-N Einzel lens structure. The electron micrographs acquired in this mode are presented in Fig. 4.11-Fig. 4.13. The Cu grid meshes appeared distinct at this mode and relatively better resolved images as compared with source lens focusing mode. It indicates that the off axis e-beam produced some sort of spherical aberration. The interference of electric field produced by Einzel lens and deflector probably makes distorted image at the corner side. It articulates that the microcolumn with Type-N Einzel lens can give clear and resolved images; nonetheless the optimized gap between electrodes is appreciated.

To find the scan ranges in both focusing modes, we measured the e-beam deflections from the optical axis (black arrow lines) at corresponding focal points of Fig. 2.14 and Fig. 2.15 and plotted in Fig. 5.3. The black solid square box in plot of Fig. 5.3 represent scan range in one-lens focusing mode and open blue circle represent scan range in two-lens focusing mode. The plot shows that scan range reduces with the increase in gap between electrodes in source lens focusing mode. The results is opposite for the two-lens focusing mode.

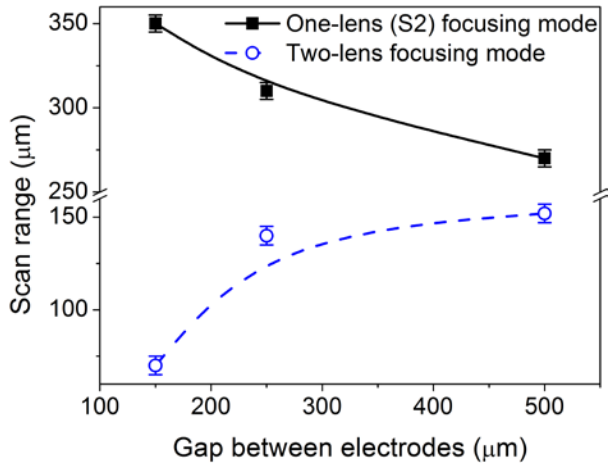


**Fig. 5.3** A simulation plot of scan range versus gap between electrodes in Einzel lens system.

These simulation and experimental results illustrate that scan range is larger for Type-N than Type-W Einzel lens structure in one-lens focusing mode whereas opposite in two-lens focusing mode. This phenomenon can be attributed by the variation in e-beam travelling distance and electric potential distribution in different Einzel lens structures. The total e-beam travelling path in Einzel lens region is shorter in Type-N which provides larger solid angle to e-beam at exit site. Because of larger solid angle, the beam could spread to larger area giving larger scan range. Electric field in Type-N Einzel lens structure leaks out from the first and third electrodes of Einzel lens which interferes electric field of neighboring components resulting noisy images.

Therefore, the gap between electrodes of Einzel lens structure plays an important role in microcolumn performance. From the simulation data, it is found that the electric field variation is highly influence by the gap between electrodes. Therefore, it is required to be considered the gap between lens-

electrode for better image quality and wide scan range. The plot depicts that the appropriate gap between lens electrode lies between 200 ~ 300 μm.

# 6 CONCLUSION AND PERSPECTIVES

This research has focused on design, fabrication and characterization of an Einzel lens for an e-beam microcolumn. I presented a research conducted for a Si based electrostatic lenses for Einzel lens system. The designed Einzel lens is consisted of flexible structures including aperture size, electrode thickness, gap between lens-electrode, and number of electrodes in a lens system. This design compiles the further miniaturization of electrostatic lens of which size is down to a few hundred micrometers in its thickness. Moreover, the choice of lens size is in control and can be optimized for the specific application according to necessity. The electrode thickness can be fabricated down to a few micrometers or several tens of micrometers. It excludes the bulk Si to support thin electrode rather Pyrex itself provides the mechanical supports. By selecting the appropriate Pyrex thickness the lens structure can be adjusted for the specific purpose. The lens structure can be useful for high voltage operation by using thick-Pyrex between lens-electrodes because of its high dielectric strength.

I did electrodynamics simulation of electrostatic lens structure with 2D and 3D models in AC/DC module of COMSOL multiphysics software. With this finite element analysis simulation tools, electric potential/field distributions have been calculated for different types of models. The simulation results show that the variation of electric field/potential distribution inside the lens structure depends upon geometrical shape and structure such as gap between lens electrodes. For instance, the variation of electric field intensity is sharp in case of narrow gap between lens electrodes; and the strong field distribution is

observed at the outside of the lens system too in Type-N. Hence, there is strong interaction of electric field applied on the Einzel lens with the electric filed produced by surrounding electrical components. Because of the strong interference of the electric field to the deflector and sample itself, it negatively affects the image quality and resolution. For the electron beam trajectories and scan range analysis with variation of gap between Einzel lens-electrodes, electrodynamics simulation was performed using vector field Opera software. The simulation results show that the scan range increases with decreasing gap between lens-electrodes in one-lens focusing mode but opposite in the two-lens focusing mode. These results were experimentally verified in chapter IV after successful fabrication of the lens designed in chapter II.

I designed several patterns in cadence drawing software and printed on Cr coated soda lime photomask following e-beam lithography maintaining a resolution better than 1 μm. The photomasks were used to define three dimensional (3D) structures on Si including lens-apertures and membrane thickness. I successfully fabricated electrostatic lenses following a set of MEMS fabrication processes such as lithography, wet and dry etching, deposition, oxidation, doping, and bonding. Photolithography, silicon DRIE, and wet etching are critical steps that determine the quality of lens-electrode.

I aligned multiple lens-electrodes along an axis passing through center of apertures in parallel using laser diffraction technique. The verification of the alignment accuracy using transmission optical microscopy shows that the misalignment of the identical lens-electrodes is ~ 1 μm which is within the limit

of microscopy itself; however, the probability of misalignment is a bit larger for asymmetric apertures.

I prepared different types of Einzel lens structures such as various gap between lens-electrodes, different sizes of apertures, and alignment of symmetric and asymmetric multiple apertures. The experimental results proved that the performance of microcolumn depends upon the Einzel lens structure. With the changes in gap between lens-electrodes, the image quality and scan ranges also changes, in addition, the performance depends on the mode of microcolumn operation too. For example, Type-N gives larger field of view (FOV) when column is operated in source lens focusing mode. Nonetheless, it is not useful in achieving good image quality in Einzel lens focusing mode. Whereas, Type-W provides better image quality in Einzel lens focusing mode and larger scan range in two-lens focusing mode.

After the series of experiments in obtaining improved image quality and scan ranges, it is concluded that combined source and Einzel lens focusing mode improved image quality by minimizing the influence of the electric field from the Einzel lens structure. From simulation data, the Type-W seems to be better for larger scan range than Type-N when the column is operated in two-lens focusing mode.

The design and fabrication techniques developed in this research opens the applications of flexible gap between lens-electrodes for a microcolumn. For larger scan range with good quality image, the gap between Einzel lens structures needs to be adjusted according to requirements. This problem is expected to be addressed in future researches. The effects of thickness of lens-electrodes is

expected to be studied in future. An alternate lens-electrode such as graphite/graphene may be useful for constructing extremely thin lens electrode and nanometer size apertures. The field emitter tip such as carbon nanotube can be integrated with the source lens for further miniaturization of microcolumn. Multi carbon nanotubes may be incorporated for higher beam energy because of its extremely small size.

# 7 REFERENCES


[1] T.H.P. Chang, D.P. Kern, M.A. Mccord.Electron-Optical Performance of a Scanning Tunneling Microscope Controlled Field-Emission Microlens System, J Vac Sci Technol B, **7** (1989) 1855-1861.

[2] T.H.P. Chang, M.G.R. Thomson, M.L. Yu, E. Kratschmer, H.S. Kim, K.Y. Lee, S.A. Rishton, S. Zolgharnain.Electron beam technology - SEM to microcolumn, Microelectron Eng, **32** (1996) 113-130.

[3] R. Saini, Z. Jandric, J. Gammell, S.A.M. Mentink, D. Tuggle.Manufacturable MEMS miniSEMs, Microelectron Eng, **83** (2006) 1376-1381.

[4] L.P. Muray.Developments in Low-Voltage Microscopy Instrumentation, Scanning, **33** (2011) 155-161.

[5] T.H.P. Chang, M.G.R. Thomson, E. Kratschmer, H.S. Kim, M.L. Yu, K.Y. Lee, S.A. Rishton, B.W. Hussey, S. Zolgharnain.Electron-beam microcolumns for lithography and related applications, J Vac Sci Technol B, **14** (1996) 3774-3781.

[6] S.Y. Chen, H.T. Ng, S.Y. Ma, H.H. Chen, C.H. Liu, K.Y. Tsai.Lithography-patterning-fidelity-aware electron-optical system design optimization, J Vac Sci Technol B, **29** (2011).

[7] H.S. Kim, S. Ahn, D.W. Kim, Y.C. Kim, S.J. Ahn.Photo-mask fabrication by low-energy microcolumn lithography, Microelectron Eng, **86** (2009) 2049-2052.

[8] P. Kruit.The role of MEMS in maskless lithography, Microelectron Eng, **84** (2007) 1027-1032.

[9] L.P. Muray, C.S. Silver, J.P. Spallas.Sub-100-nm lithography with miniature electron beam columns, J Vac Sci Technol B, **24** (2006) 2945-2950.

[10] H.S. Kim, S. Ahn, D.W. Kim, Y.C. Kim, H.W. Kim, S.J. Ahn.Sub-60-nm lithography patterns by low-energy microcolumn lithography, J Korean Phys Soc, **49** (2006) S712-S715.

[11] A. Jamieson, C.G. Willson, Y.Z. Hsu, A.D. Brodie.Low-voltage electron beam lithography resist processes: top surface imaging and hydrogen silisesquioxane bilayer, J Microlith Microfab, **3** (2004) 442-449.

[12] L.P. Muray, J.P. Spallas, C. Stebler, K. Lee, M. Mankos, Y. Hsu, M. Gmur, T.H.P. Chang.Advances in arrayed microcolumn lithography, J Vac Sci Technol B, **18** (2000) 3099-3104.

[13] T.S. Oh, D.W. Kim, Y.C. Kim, S. Ahn, G.H. Lee, H.S. Kim.Inspection of open defects in a thin film transistor-liquid crystal display panel by using a low-energy electron microcolumn, J Vac Sci Technol B, **28** (2010) C6c69-C66c73.

[14] H.S. Kim, D.W. Kim, Y.C. Kim, S. Ahn, S.J. Ahn.A Novel Inspection Method Using a Low-Energy Electron Beam for the Contact/Via-Holes in Multi-Layer ULSI Devices, J Korean Phys Soc, **55** (2009) 1758-1762.

[15] Y.C. Kim, D.W. Kim, S. Ahn, T.S. Oh, J.B. Kim, Y.S. Roh, D.G. Hasko, H.S. Kim.Inspection method for contact/via-holes using a low-energy electron microcolumn, J Vac Sci Technol B, **27** (2009) 3208-3212.

[16] J.P. Spallas, C.S. Silver, L.P. Muray.Arrayed miniature electron beam columns for mask making, J Vac Sci Technol B, **24** (2006) 2892-2896.

[17] T.H.P. Chang, D.P. Kern, L.P. Muray.Microminiaturization of Electron-Optical Systems, J Vac Sci Technol B, **8** (1990) 1698-1705.

[18] M.A. Mccord, T.H.P. Chang, D.P. Kern, J.L. Speidell.A Novel Scanning Tunneling Microscope Controlled Field-Emission Microlens Electron Source, J Vac Sci Technol B, **7** (1989) 1851-1854.

[19] M.A. Mccord, T.H.P. Chang, D.P. Kern, J.L. Speidell.An Stm Controlled Field-Emission Microlens Electron Source, Inst Phys Conf Ser, (1989) 165-166.

[20] A. Cerezo, M.K. Miller.Einzel Lenses in Atom Probe Designs, Surf Sci, **246** (1991) 450-456.

[21] L.P. Muray, U. Staufer, D.P. Kern, T.H.P. Chang.Performance-Measurements of a 1-Kev Electron-Beam Microcolumn, J Vac Sci Technol B, **10** (1992) 2749-2753.

[22] M. Despont, U. Staufer, C. Stebler, R. Germann, P. Vettiger.Microfabrication of Lenses for a Miniaturized Electron Column, Microelectron Eng, **27** (1995) 467-470.

[23] E. Kratschmer, H.S. Kim, M.G.R. Thomson, K.Y. Lee, S.A. Rishton, M.L. Yu, T.H.P. Chang.An electron-beam microcolumn with improved resolution, beam current, and stability, J Vac Sci Technol B, **13** (1995) 2498-2503.

[24] J.P. Spallas, C.S. Silver, L.P. Muray, T. Wells, M. El-Gomati.A manufacturable miniature electron beam column, Microelectron Eng, **83** (2006) 984-989.

[25] R. Saini, Z. Jandric, I. Gory, S.A.M. Mentink, D. Tuggle.Assembled microelectromechanical system microcolumns for miniature scanning electron microscopies, J Vac Sci Technol B, **24** (2006) 813-817.

[26] M.G.R. Thomson, T.H.P. Chang.Lens and deflector design for microcolumns, J Vac Sci Technol B, **13** (1995) 2445-2449.

[27] Y.C. Kim, S.J. Ahn, T.S. Oh, D.W. Kim, H.S. Kim, W.K. Jang.Low energy microcolumn for large field view inspection, Ultramicroscopy, **111** (2011) 1645-1649.

[28] H.S. Kim, Y.C. Kim, D.W. Kim, S.J. Ahn, Y. Jang, H.W. Kim, D.J. Seong, K.W. Park, S.S. Park, B.J. Kim.Low energy electron beam microcolumn lithography, Microelectron Eng, **83** (2006) 962-967.

[29] Y.C. Kim, H.S. Kim, S.J. Ahn, H.W. Kim, T. Yoshimoto, D.W. Kim.Advanced microcolumn operation for low-energy electron-beam lithography, J Korean Phys Soc, **49** (2006) 1428-1433.

[30] T.H.P. Chang, M. Mankos, K.Y. Lee, L.P. Muray.Multiple electron-beam lithography, Microelectron Eng, **57-8** (2001) 117-135.

[31] H. Kim, C. Han, K. Chun.The novel deflector for multi arrayed microcolumn using microelectromechanical system (MEMS) technology, Japanese Journal of Applied Physics Part 1-Regular Papers Short Notes & Review Papers, **42** (2003) 4084-4088.

[32] H.S. Kim, D.W. Kim, S. Ahn, Y.C. Kim, J. Cho, S.K. Choi, D.Y. Kim.Arrayed microcolumn operation with a wafer-scale Einzel lens, Microelectron Eng, **78-79** (2005) 55-61.

[33] H.S. Kim, D.W. Kim, S. Ahn, S.S. Park, M.H. Seol, Y.C. Kim, S.K. Choi, D.Y. Kim.Multi-beam microcolumns based on arrayed SCM and WCM, J Korean Phys Soc, **45** (2004) 1214-1217.

[34] J.W. Jeong, D.J. Kim, H.S. Kim, S.K. Choi, D.Y. Kim, H.R. Lee.Experimental evaluation of arrayed microcolumns with monolithic structure, Jpn J Appl Phys 1, **44** (2005) 5565-5569.

[35] R.Y. Lutsch, E. Plies.Initial resolution measurements of miniaturized electrostatic lenses for LVSEM, Ultramicroscopy, **93** (2002) 339-345.

[36] T.H.P. Chang, D.P. Kern, L.P. Muray.Arrayed Miniature Electron-Beam Columns for High Throughput Sub-100 Nm Lithography, J Vac Sci Technol B, **10** (1992) 2743-2748.

[37] Y.J. Lee, S.H. Kang, D.H. Kim, J.Y. Park, H.J. Choi, Y. Kuk, K. Chun.Construction of microcolumn system and its application to nanolithography, Microelectron Eng, **42** (1998) 485-488.

[38] H.S. Kim, D.W. Kim, S.J. Ahn, Y.C. Kim, S.S. Park, K.W. Park, N.W. Hwang, S.W. Jin, S.Y. Bae.Feasibility study of TFT-LCD array tester using low voltage micro-columns, Microelectron Eng, **85** (2008) 782-786.

[39] C. Stebler, M. Despont, U. Staufer.Miniaturized E-Beam Writer -Testing of Components, Microelectron Eng, **27** (1995) 155-158.

[40] J.P.S. Fitzgerald, R.C. Word, R. Konenkamp.Aberrations in asymmetrical electron lenses, Ultramicroscopy, **119** (2012) 40-44.

[41] E. Steinwand, J.N. Longchamp, H.W. Fink.Fabrication and characterization of low aberration micrometer-sized electron lenses, Ultramicroscopy, **110** (2010) 1148-1153.

[42] O. Sise, M. Ulu, M. Dogan.Aberration coefficients of multi-element cylindrical electrostatic lens systems for charged particle beam applications, Nucl Instrum Meth A, **573** (2007) 329-339.

[43] Z. Liu.Differential algebraic method for aberration analysis of typical electrostatic lenses, Ultramicroscopy, **106** (2006) 220-232.

[44] D. Dunham, D.M. Desloge, G.F. Rempfer, W.P. Skoczylas, B.P. Tonner.Evaluation of Aberration Coefficients of Practical Electrostatic Lenses for X-Ray-Absorption Micro-Spectroscopy and Imaging, Nucl Instrum Meth A, **347** (1994) 441-445.

[45] S.J. Ahn, D.W. Kim, H.S. Kim, K.H. Cho, S.S. Choi.Laser fabrication of micron-size apertures for electron beam microcolumns, Appl Phys a-Mater, **69** (1999) S527-S530.

[46] Y.V. White, X.X. Li, Z. Sikorski, L.M. Davis, W. Hofmeister.Single-pulse ultrafast-laser machining of high aspect nano-holes at the surface of SiO2, Optics express, **16** (2008) 14411-14420.

[47] O.K. Suwal, A. Sharma, Y.B. Lee, T.S. Oh, D.W. Kim, H.S. Kim.Influence of Einzel lens structure on the performance of a microcolumn fabricated through MEMS technology, Advanced Materials Research, **694-697** (2013) 1001-1007.

[48] S.S. Park, D.W. Kim, S. Ahn, Y.C. Kim, S.K. Choi, D.Y. Kim, H.S. Kim.High-beam-current microcolumns with large apertures, Japanese Journal of Applied Physics Part 1-Regular Papers Short Notes & Review Papers, **43** (2004) 3986-3989.

[49] H.S. Kim, D.W. Kim, S.J. Ahn, Y.C. Kim, S.S. Park, S.K. Choi, D.Y. Kim.The assembly of a fully functional microcolumn and its STEM-mode operation, J Korean Phys Soc, **43** (2003) 831-835.

[50] S. Ahn, D.W. Kim, H.S. Kim, S.J. Ahn, J. Cho.Fabrication of a miniaturized electron lens system and laser micro-machining condition for silicon membrane, Microelectron Eng, **69** (2003) 57-64.

[51] R.A. Bakish.Introduction to electron beam technology, Wiley, New York,, 1962.

[52] D.W.O. Heddle.Electrostatic lens systems, Adam Hilger, Bristol ; Philadelphia, 1991.

[53] G.F. Rempfer.The relationship of lens aberrations to image aberrations in electron optics, Optik, **110** (1999) 17-24.

[54] B. Lencova.Accuracy of electrostatic lens computations with FOFEM, Ultramicroscopy, **93** (2002) 263-270.

[55] Y.C. Kim, D.W. Kim, S. Ahn, S.K. Choi, D.Y. Kim, H.S. Kim.Effect of the Einzel lens structure in microcolumn, Japanese Journal of Applied Physics Part 1-Regular Papers Short Notes & Review Papers, **43** (2004) 3728-3730.

[56] COMSOL.COMSOL 4.3, http://www.comsol.com/products/acdc/, **4.3** (2012).

[57] Cobham.Opera simulation software, http://www.cobham.com/, **10** (2010).

[58] L.F. Thompson, C.G. Willson, M.J. Bowden.Introduction to microlithography, 2nd ed., American Chemical Society, Washington, DC, 1994.

[59] M.J. Madou.Fundamentals of microfabrication: the science of miniaturization, CRC PressI Llc, 2002.

[60] Z.S. Huang, Y. Melaku, W. Nguyen.A study of the O-2-SO2 plasma etch chemistry for top surface imaging photoresist dry development, Japanese Journal of Applied Physics Part 1-Regular Papers Short Notes & Review Papers, **37** (1998) 2373-2380.

[61] J. Munoz, C. Dominguez.Tone control in dry development of photosensitive polyimides, Vacuum, **49** (1998) 35-41.

[62] J. Munoz, C. Dominguez.Dry development of photosensitive polyimides for high resolution and aspect ratio applications, J Vac Sci Technol B, **13** (1995) 2179-2183.

[63] D. Louis, P. Laporte, P. Gachon.Improvement of Dry Development of Photoresist in a Ripe Source for 0.4 to 0.35 Mu-M Technologies, Microelectron Eng, **23** (1994) 271-274.

[64] C.C. Tin, T.H. Lin, Y. Tzeng.Effects of Rf Bias on Remote Microwave Plasma Assisted Etching of Silicon in Sf6, J Electrochem Soc, **138** (1991) 3094-3100.

[65] S. Tachi, K. Tsujimoto, S. Arai, T. Kure.Low-Temperature Dry Etching, Journal of Vacuum Science & Technology a-Vacuum Surfaces and Films, **9** (1991) 796-803.

[66] S. Tachi.Low-Temperature Dry Etching for Ulsi, Denki Kagaku, **57** (1989) 277-281.

[67] F.S. Laermer, DE), Schilp, Andrea (Schwa/ bisch Gmu/ nd, DE).Method of anisotropically etching silicon, in, Robert Bosch GmbH (Stuttgart, DE), United States, 1996.

[68] F.S. Laermer, DE), Schilp, Andrea (Schwaebisch Gmuend, DE).Method of anisotropic etching of silicon, in, Robert Bosch GmbH (Stuttgart, DE), United States, 2003.

[69] F.S. Laermer, DE), Schilp, Andrea (Schwaebisch Gmuend, DE).Method for anisotropic etching of silicon, in, Robert Bosch GmbH (Stuttgart, DE), United States, 2001.

[70] M.D. Henry, C. Welch, A. Scherer.Techniques of cryogenic reactive ion etching in silicon for fabrication of sensors, J Vac Sci Technol A, **27** (2009) 1211-1216.

[71] S. Samukawa, S. Furuoya.Polymerization for Highly Selective Sio2 Plasma-Etching, Japanese Journal of Applied Physics Part 2-Letters, **32** (1993) L1289-L1292.

[72] A.M. Hynes, H. Ashraf, J.K. Bhardwaj, J. Hopkins, I. Johnston, J.N. Shepherd.Recent advances in silicon etching for MEMS using the ASE (TM) process, Sensors and Actuators a-Physical, **74** (1999) 13-17.

[73] E.H. Klaassen, K. Petersen, J.M. Noworolski, J. Logan, N.I. Maluf, J. Brown, C. Storment, W. McCulley, G.T.A. Kovacs.Silicon fusion bonding and deep reactive ion etching: A new technology for microstructures, Sensors and Actuators a-Physical, **52** (1996) 132-139.

[74] F. Marty, L. Rousseau, B. Saadany, B. Mercier, O. Francais, Y. Mita, T. Bourouina.Advanced etching of silicon based on deep reactive ion etching for silicon high aspect ratio microstructures and three-dimensional micro- and nanostructures, Microelectron J, **36** (2005) 673-677.

[75] R. Abdolvand, F. Ayazi.An advanced reactive ion etching process for very high aspect-ratio sub-micron wide trenches in silicon, Sensor Actuat a-Phys, **144** (2008) 109-116.

[76] S. Rauf, W.J. Dauksher, S.B. Clemens, K.H. Smith.Model for a multiple-step deep Si etch process, J Vac Sci Technol A, **20** (2002) 1177-1190.

[77] F. Becker, I.W. Rangelow, R. Kassing.Ion energy distributions in SF6 plasmas at a radio-frequency powered electrode, J Appl Phys, **80** (1996) 56-65.

[78] H. Hayashi, S. Morishita, T. Tatsumi, Y. Hikosaka, S. Noda, H. Nakagawa, S. Kobayashi, M. Inoue, T. Hoshino.Mechanism of C4F8 dissociation in parallel-plate-type plasma, Journal of Vacuum Science & Technology a-Vacuum Surfaces and Films, **17** (1999) 2557-2571.

[79] H. Hayashi, M. Okigawa, S. Morishita, M. Sekine.Mechanism of fluorine reduction in C4F8/Ar parallel-plate-type electron-cyclotron-resonance plasma by a Si top plate, Journal of Vacuum Science & Technology a-Vacuum Surfaces and Films, **17** (1999) 2517-2524.

[80] H. Seidel, L. Csepregi, A. Heuberger, H. Baumgartel.Anisotropic Etching of Crystalline Silicon in Alkaline-Solutions .1. Orientation Dependence and Behavior of Passivation Layers, Journal of the Electrochemical Society, **137** (1990) 3612-3626.

[81] K. Sato, M. Shikida, T. Yamashiro, K. Asaumi, Y. Iriye, M. Yamamoto.Anisotropic etching rates of single-crystal silicon for TMAH water solution as a function of crystallographic orientation, Sensor Actuat a-Phys, **73** (1999) 131-137.

[82] J.T.L. Thong, W.K. Choi, C.W. Chong.TMAH etching of silicon and the interaction of etching parameters, Sensor Actuat a-Phys, **63** (1997) 243-249.

[83] E. Steinsland, M. Nese, A. Hanneborg, R.W. Bernstein, H. Sandmo, G. Kittilsland.Boron etch-stop in TMAH solutions, Sensor Actuat a-Phys, **54** (1996) 728-732.

[84] U. Schnakenberg, W. Benecke, P. Lange.TMAHW etchants for silicon micromachining, in: Solid-State Sensors and Actuators, 1991. Digest of Technical Papers, TRANSDUCERS '91., 1991 International Conference on, 1991, pp. 815-818.

[85] M. Shikida, T. Masuda, D. Uchikawa, K. Sato.Surface roughness of single-crystal silicon etched by TMAH solution, Sensor Actuat a-Phys, **90** (2001) 223-231.

[86] I. Zubel, M. Kramkowska.The effect of isopropyl alcohol on etching rate and roughness of (100) Si surface etched in KOH and TMAH solutions, Sensor Actuat a-Phys, **93** (2001) 138-147.

[87] A.B. Sproul, M.A. Green.Improved Value for the Silicon Intrinsic Carrier Concentration from 275-K to 375-K, J Appl Phys, **70** (1991) 846-854.

[88] W.R. Thurber, R.L. Mattis, Y.M. Liu, J.J. Filliben.Resistivity-Dopant Density Relationship for Boron-Doped Silicon, J Electrochem Soc, **127** (1980) 2291-2294.

[89] H.S. Min, Y.C. Joo, O.S. Song.Effects of wafer cleaning and annealing on glass/silicon wafer direct bonding, J Electron Packaging, **126** (2004) 120-123.

[90] F. Pigeon, B. Biasse, M. Zussy.Low-Temperature Pyrex Glass Wafer Direct Bonding, Electron Lett, **31** (1995) 792-793.

[91] A. Cozma, B. Puers.Characterization of the Electrostatic Bonding of Silicon and Pyrex Glass, J Micromech Microeng, **5** (1995) 98-102.

[92] W.B. Choi, B.K. Ju, Y.H. Lee, J.W. Jeong, M.R. Haskard, N.Y. Lee, M.Y. Sung, M.H. Oh.Experimental analysis on the anodic bonding with an evaporated glass layer, J Micromech Microeng, **7** (1997) 316-322.

[93] G. Wallis, Pomerant.Di.Field Assisted Glass-Metal Sealing, J Appl Phys, **40** (1969) 3946.

[94] K.M. Knowles, A.T.J. van Helvoort.Anodic bonding, Int Mater Rev, **51** (2006) 273-311.

[95] J. Wei, S.M.L. Nai, C.K. Wong, L.C. Lee.Glass-to-glass anodic bonding process and electrostatic force, Thin Solid Films, **462** (2004) 487-491.

[96] G. Blasquez, P. Favaro.Silicon glass anodic bonding under partial vacuum conditions: problems and solutions, Sensor Actuat a-Phys, **101** (2002) 156-159.

[97] G.W. Hsieh, C.H. Tsai, W.C. Lin.Anodic bonding of glass and silicon wafers with an intermediate silicon nitride film and its application to batch fabrication of SPM tip arrays, Microelectron J, **36** (2005) 678-682.

[98] T.M.H. Lee, I.M. Hsing, C.Y.N. Liaw.An improved anodic bending process using pulsed voltage technique, J Microelectromech S, **9** (2000) 469-473.

[99] T.M.H. Lee, D.H.Y. Lee, C.Y.N. Liaw, A.I.K. Lao, I.M. Hsing.Detailed characterization of anodic bonding process between glass and thin-film coated silicon substrates, Sensor Actuat a-Phys, **86** (2000) 103-107.

[100] M.X. Chen, L.L. Yuan, S. Liu.Research on low-temperature anodic bonding using induction heating, Sensor Actuat a-Phys, **133** (2007) 266-269.

[101] D.J. Lee, B.K. Ju, J. Jang, K.B. Lee, M.H. Oh.Effects of a hydrophilic surface in anodic bonding, J Micromech Microeng, **9** (1999) 313-318.

[102] T.H.P. Chang, L.P. Muray, U. Staufer, D.P. Kern.A Scanning Tunneling Microscope Based Microcolumn System, Japanese Journal of Applied Physics Part 1-Regular Papers Short Notes & Review Papers, **31** (1992) 4232-4240.

[103] H.A. Bethe.Theory of diffraction by small holes, Phys Rev, **66** (1944) 163-182.

# 8 ABSTRACT IN KOREAN

1990 년대 마이크로 칼럼의 개발 이후에 전자광학시스템의 소형화는 이 분야 연구의 주된 관심사 중의 하나였다. 마이크로 칼럼은 초소형 전자방출원, 소형화된 전자렌즈, 디플렉터, 그리고 소형화된 대물렌즈들로 구성된다. 마이크로 칼럼의 성능과 특성에 대한 꾸준한 개선이 이루어져 왔지만 아직도 마이크로 칼럼을 구성하는 각각의 부품들의 제작과 최적화를 위한 몇 가지 과제들이 남아 있으며, 이 논문에서는 그 중에서 전자렌즈의 디자인과 제작, 그리고 아인즐렌즈 구조에 따른 마이크로 칼람의 동작 성능에 대해 집중하여 기술할 것이다.

전자렌즈는 두 가지 종류를 고려하였다. 첫 번 째는 bulk Si 구조물에 의해 지지되는 얇은 Si 멤브레인형 전자렌즈이고, 두 번 째는 Si 구조물을 제거하고 단순히 절연체인 파이렉스에 의해 지지되는 Si 멤브레인형 전자렌즈이다. 전자의 경우에는 후자에 비해서 Si 멤브레인 막은 작지만 전자렌즈간의 간격을 조절하는 데는 한계가 있다. 후자의 경우에는 이러한 한계가 없으므로 렌즈간 간격을 자유롭게 조절할 수 있으며, 그만큼 소스렌즈나 아인즐렌즈 구조 디자인에서 유연성을 발휘할 수 있는 장점이 있다.

2 장에서는 위의 두 가지 유형에 전자렌즈 구조에 따른 정전위와 정전기장의 변화에 대한 전산모사 결과가 제시될 것이다. 또한, 아인즐렌즈 구조에서 전자렌즈간 간격 변화가 주는 영향을 조사하기

위해서, 렌즈간 간격이 서로 다른 몇 가지 종류의 아인즐렌즈에 대해 전산모사 연구를 진행하였으며, 이 때 렌즈간 간격은 150 μm 에서 500 μm 까지 변화시켰다. 기본적으로 아인즐렌즈는 retarding mode 로 동작시켰으며, one-lens focusing mode 와 two-lens focusing mode 에서 scan range 의 변화를 분석하였다.

전자렌즈의 제작과 마이크로 칼럼의 조립 등 자세한 실험과정은 3 장에 기술되어 있다. micro-electro-mechanical systems (MEMS) 공정을 기반으로 하는 박막형 Si 렌즈 제작 공정을 개발하였으며, 제작된 렌즈들은 레이저 디프렉션 패턴을 이용하는 방법으로 광축상에 ~1 μm 정밀도로 정렬하였다.

전산모사 결과를 구현하기 위해 아인즐렌즈 구조가 서로 다른 두 종류의 마이크로 칼럼을 제작하여 실험을 수행하였으며, one-lens focusing mode 와 two-lens focusing mode 로 실험한 결과가 4 장에 제시되어 있다. 아인즐렌즈 구조와 동작 모드에 따라서 이미지의 질과 해상도, 그리고 scan range 가 변화하였는데, 소스렌즈 focusing mode 에서는 렌즈간 간격이 감소할수록 scan range 가 증가하였고, two lens focusing mode 에서는 경향성이 역전되어 나타났다. 이러한 결과는 2 장의 전산모사에서 예측된 것과 일치하고 있으며, 보다 넓은 scan range 를 얻을 수 있는 아인즐렌즈 구조 디자인에 대한 논의가 이루어질 것이다.

# APPENDIX A: ELECTRON OPTICS AND ELECTRON MOTION IN ELECTRIC FIELD

## A.1 Principle of electrostatic lens

### A.1.1 Electron motion in electrostatic fields

Consider an electron with charge e mass m, moving with velocity **v** in an electric field **E**, the electric force on an electron is in general vector form and is given as [51]:

$$m\frac{d\boldsymbol{v}}{dt} = e\boldsymbol{E} \qquad \text{A.1}$$

and the electric field is determined from the electric potential V by taking the gradient as indicated by the statement:

$$\boldsymbol{E} = -\boldsymbol{\nabla}V \qquad \text{A.2}$$

Combining equations A.1 and A.2

$$m\frac{d\boldsymbol{v}}{dt} = -e\boldsymbol{\nabla}V \qquad \text{A.3}$$

Taking line integral of both sides of the equation, along any arbitrary path from point a to b. Thus

$$m\int_a^b \frac{d\boldsymbol{v}}{dt}.\boldsymbol{dl} = -e\int_a^b \boldsymbol{\nabla}V \cdot \boldsymbol{dl} \qquad \text{A.4}$$

or $$\frac{m}{2}(|v_b|^2 - |v_a|^2) = -e\int_a^b -\mathbf{E}\cdot\boldsymbol{dl} = -e(V_b - V_a) \quad \text{A.5}$$

It states that increase in kinetic energy of the particle between points a and b is equivalent to integral of force times displacement, i.e. work done by the field on the particle. It is a conservation of energy. Hence work done by an electron is stated in eV (electron-volt) which is $1.602 \times 10^{-19}$ joule.

For an electron that starts from rest and gain velocity **v** with potential difference V, the equation 5 leads to

$$|v| = \sqrt{-\mathbf{2}eV/m} \quad \text{A.6}$$

It holds true till the velocity is quite below the relativistic velocity and there is no high-frequency electric fields.

Equation A.1 can be expanded into three separate equations:

$$\frac{d^2x}{dt^2} = -\frac{e}{m}E_x$$

$$\frac{d^2y}{dt^2} = -\frac{e}{m}E_y \quad \text{A.7}$$

$$\frac{d^2z}{dt^2} = -\frac{e}{m}E_z$$

Each field component acts independently of the others.

Let an electron projected at an angle $\theta$ to x-axis into a uniform electric field. If the potential of the lower plate, y = 0, is $V_0$, then the initial velocity at this plane is

$$v_0 = \sqrt{-2eV_0/m} \qquad \text{A.8}$$

The initial x-velocity

$$v_{x0} = v_0 cos\theta \qquad \text{A.9}$$

remains unaffected throughout the electrons flight because there is no x-component of electric field. The y-velocity is initially

$$v_{y0} = v_0 sin\theta \qquad \text{A.10}$$

and decreases with time in the uniform retarding field. The maximum height on the trajectory is attained when this kinetic energy is all converted to potential energy; that is, when the potential has fallen by an amount given by

$$y_{max} = -\frac{m}{2e}\frac{v_0^2}{E} sin^2\theta \qquad \text{A.11}$$

The y-motion is governed by the second of equation A.7 with **E** constant. A simple integration with respect to time yields

$$\frac{dy}{dt} = \frac{e}{m} Et + v_0 sin\theta \qquad \text{A.12}$$

And second integration gives

$$y = \frac{e}{2m} Et^2 + v_0 t\ sin\theta \qquad \text{A.13}$$

Because of the uniform x-velocity, t may be expressed in terms of x

$$t = \frac{x}{v_0\ cos\theta} \qquad \text{A.14}$$

From which we find

$$y = x\,tan\theta - \frac{E}{4V_0}\frac{x^2}{cos^2\theta} \qquad \text{A.15}$$

The range of the electron, that is, the x-distance it travels before returning to the y = 0 plane, is found by setting y = 0 and solving for $x_0$, the corresponding value of x.

$$x_0 = \frac{2V_0}{E}\sin 2\theta \qquad \text{A.16}$$

### A.1.2 Electrostatic lens

The region between any two equipotential $V_n$ and $V_{n+1}$ is approximated by the constant average potential

$$\bar{V}_n = {}^1\!/_2\,(V_n + V_{n+1}) \qquad \text{A.17}$$

The electron, moving in this stepwise approximation to the real potential, follows straight-line paths between equipotential, but it is subject to an impulsive force at each boundary where the potential is assumed to be changed. This force is normal to the boundary thus leaving the momentum parallel to the boundary unaffected. Equating the tangential components of velocity we obtain

$$v_n \sin\theta_n = v_{n+1}\sin\theta_{n+1} \qquad \text{A.18}$$

Combining equations 18 and 5 leads to

$$\frac{\sin\theta_{n-1}}{\sin\theta_n} = \sqrt{\frac{\bar{V}_n}{\bar{V}_{n-1}}} = \sqrt{\frac{V_{n+1}+V_n}{V_n+V_{n-1}}} \qquad \text{A.19}$$

The equation A.19 is analogous to Snell's law for the refraction of a light ray as it passes from one medium to another. This similarity is one of the bases

for introducing the terminology of optics into certain problems of electron dynamics.

The field between the two equipotential $V_n$ and $V_{n+1}$ subjects the electron to a force given by

$$f_n = -e\left(\frac{V_{n+1} - V_n}{d_n}\right) \qquad \text{A.20}$$

where $d_n$ is the normal separation between the equipotential at the point where the electron enters this region.

The component of force normal to electron path is balanced by centrifugal force $mv^2/R_n$.

$$\frac{mv^2}{R_n} = -e\left(\frac{V_{n+1} - V_n}{d_n}\right)\sin\theta_n$$

Using equation numbers A.7, A.17 in A.19, the radius of circle, $R_n$ yields

$$\frac{2e\overline{V_n}}{R_n} = -e\left(\frac{V_{n+1} - V_n}{d_n}\right)\sin\theta_n$$

or

$$\frac{V_{n+1} + V_n}{R_n} = \left(\frac{V_{n+1} - V_n}{d_n}\right)\sin\theta_n$$

or

$$R_n = \left(\frac{V_{n+1} + V_n}{V_{n+1} - V_n}\right)\frac{d_n}{\sin\theta_n} \qquad \text{A.21}$$

At each intersection of the path with an equipotential, a new radius of curvature $R_n$ is calculated and a new arc is formed which gives the trajectories of electrons.

### A.1.3 Electron optics

From equation A.19, it is seen that the quantity analogous to the optical index of refraction is √V or simply electron velocity. A bundle of electron paths passing through a common point near the axis of an axially symmetric field system can be made to pass through another common point by a relatively limited region of field variation. The first common point is appropriate to call the object and the second point is the image. Imperfections in this process are naturally called aberrations.

Unlike light lens, the electron lens is not confined by well-delineated boundaries, but consists of a more or less indefinite region in which the potential distribution must be an appropriate solution of Laplace's equation. The Laplace's equation in cylindrical coordinates is given as

$$\frac{1}{r}\frac{\partial}{\partial r}\left(r\frac{\partial V}{\partial r}\right)+\frac{\partial^2 V}{\partial z^2}=0 \qquad \text{A.22}$$

Let assume a power series expansion in r for the potential, Laplace's equation enables us to determine the coefficients of the series in terms of the potential and its derivatives on the axis only as:

$$V(r,z)=V_0(z)+a_2(z)r^2+a_4(z)r^4+\cdots \qquad \text{A.23}$$

where, $V_0(z)$ is the potential on the axis. The first term of Laplace's equation on power series is as

$$\frac{1}{r}\frac{\partial}{\partial r}\left(r\frac{\partial V}{\partial r}\right)=2^2a_2+4^2a_4r^2+6^2a_6r^4+\cdots \qquad \text{A.24}$$

Similarly, for second term of Laplace's equation be:

$$\frac{\partial^2 V}{\partial z^2} = V_0'' + a_2'' r^2 + a_4'' r^4 + \cdots \qquad \text{A.25}$$

where the primes indicates derivative with respect to z. Equation A.24 and A.25 are equal and opposite. Hence comparing these series term by term and solving successively for the coefficients, we find that

$$V(r,z) = V_0(z) - V_0''(z)\frac{r^2}{2^2} + V_0^{IV}(z)\frac{r^4}{2^2 4^2} + \cdots \qquad \text{A.26}$$

Let all the electrons follow paths which lie in rz planes, then the equations of motion are particularly simple.

$$\ddot{r} = -\frac{e}{m}\frac{\partial V}{\partial r} \qquad \text{A.27}$$

$$\ddot{z} = -\frac{e}{m}\frac{\partial V}{\partial z} \qquad \text{A.28}$$

Combining these two equations into a single radial trajectory equation as follows:

$$\dot{r} = \frac{dr}{dz}\dot{z}$$
$$\ddot{r} = \frac{dr}{dz}\ddot{z} + \frac{d^2 r}{dz^2}(\dot{z})^2 \qquad \text{A.29}$$

or
$$-\frac{e}{m}\frac{\partial V}{\partial r} = -\frac{e}{m}\frac{dr}{dz}\frac{\partial V}{\partial z} + \frac{d^2 r}{dz^2}(\dot{z})^2 \qquad \text{A.30}$$

But average velocity $v = \dot{r}^2 + \dot{z}^2 = -2eV/m$ and with equation A.29, we can write

$$\dot{z}^2\left(\frac{dr}{dz}\right)^2 = \dot{r}^2 = -\frac{2eV}{m} - \dot{z}^2$$

$$\dot{z}^2 = -\frac{2eV/m}{1+(dr/dz)^2} \qquad \text{A.31}$$

Using equation A.31 in equation A.30,

$$-\frac{e}{m}\frac{\partial V}{\partial r} = -\frac{e}{m}\frac{dr}{dz}\frac{\partial V}{\partial z} + \frac{d^2r}{dz^2}\left(-\frac{2eV/m}{1+(dr/dz)^2}\right) \qquad \text{A.32}$$

or
$$\frac{\partial V}{\partial r} = \frac{dr}{dz}\frac{\partial V}{\partial z} + \frac{d^2r}{dz^2}\left(\frac{2V}{1+(dr/dz)^2}\right) \qquad \text{A.33}$$

or
$$2V\frac{d^2r}{dz^2} = \left(\frac{\partial V}{\partial r} - \frac{dr}{dz}\frac{\partial V}{\partial z}\right)\left[1+\left(\frac{dr}{dz}\right)^2\right] \qquad \text{A.34}$$

This non-linear differential equation for r as a function of z. let assume that the e-beam path never be large angles with the axis. In this case, $(dr/dz)^2 \ll 1$ and the equation is called paraxial ray equation. The equation 34 becomes

$$2V\frac{d^2r}{dz^2} - \frac{\partial V}{\partial r}\left(1-\frac{dr}{dz}\right) = 0 \qquad \text{A.35}$$

Since r and $\partial r/\partial z$ are small, it is approximated V, $\partial V/\partial r$, and $\partial V/\partial z$ by the first terms only of their respective series expansion (equation A.26). Thus

$$V \approx V_0(z)$$

$$\frac{\partial V}{\partial r} \approx -V_0''(z)\frac{r}{2} \qquad \text{A.36}$$

$$\frac{\partial V}{\partial z} \approx V_0'(z)$$

These substitutions lead to the final form of the paraxial ray equation as follows:

$$\frac{d^2r}{dz^2}+\frac{dr}{dz}\left(\frac{V_0'}{2V_0}\right)+\frac{r}{4}\frac{V_0''}{V_0}=0 \qquad \text{A.37}$$

This paraxial ray equations has several features. (i) It is independent to e/m. (ii) It is the field distribution or shape but not its intensity which governs the trajectories. (iii) The equation is unaltered in form if a scale factor to r. It is this fact that allows us to consider electron lens since it implies the same focus (r = 0) for all trajectories parallel to the axis independently of initial radius.

Equation A.37 can be re-written in the form

$$\frac{d}{dz}\left(\sqrt{V}\frac{dr}{dz}\right)=-\frac{r}{4}\frac{V_0''}{\sqrt{V_0}} \qquad \text{A.38}$$

It follows that

$$\left|\sqrt{V}\frac{dr}{dz}\right|_1^2=-\frac{1}{4}\int_1^2\frac{rV_0''}{\sqrt{V_0}}dz \qquad \text{A.39}$$

where, 1 and 2 are arbitrary limit points. We demand that the lens be thin (or weak) that is it active region is short compared to its focal length, so r cannot change appreciably between points 1 and 2. Now r can be taken out of the integral and we obtain

$$\sqrt{V_2}\left(\frac{dr}{dz}\right)_2-\sqrt{V_1}\left(\frac{dr}{dz}\right)_1=-\frac{r}{4}\int_1^2\frac{V_0''}{\sqrt{V_0}}dz \qquad \text{A.40}$$

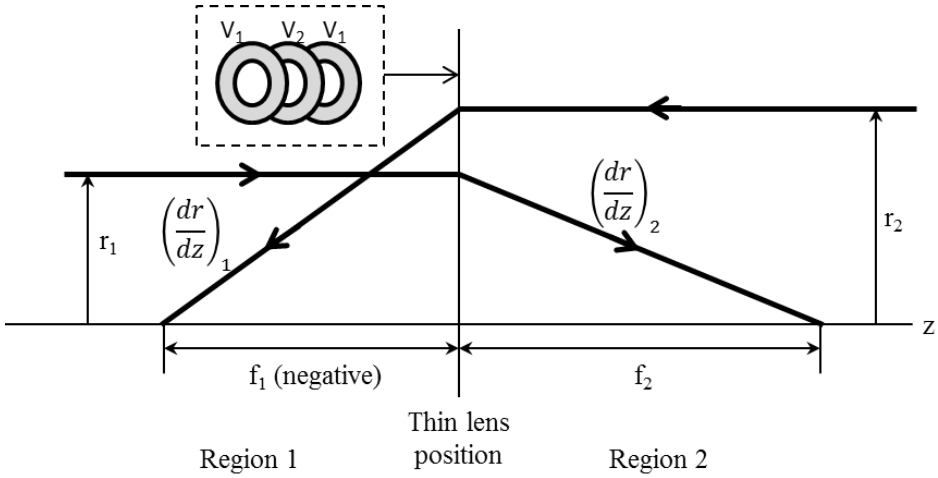


**Fig. A.1** Principal rays and location of foci for thin electrostatic lens.

If $V_0(z)$ is known explicitly, the integral can be evaluated either analytically or graphically. The focal lengths, $f_2$ for electrons moving parallel to the axis and to the right in the left-hand region (1) and $f_1$ for those moving parallel to the axis and to the left in region (2), are found by setting $(dr/dz)_1 = 0$ and $(dr/dz)_2 = 0$ separately.

This procedure results in

$$\frac{1}{f_2} = \frac{-(dr/dz)_2}{r_1} = \frac{1}{4\sqrt{V_2}} \int_1^2 \frac{V_0''}{\sqrt{V_0}} dz \qquad \text{A.41}$$

and

$$\frac{1}{f_1} = \frac{-(dr/dz)_1}{r_2} = \frac{1}{4\sqrt{V_1}} \int_1^2 \frac{V_0''}{\sqrt{V_0}} dz \qquad \text{A.42}$$

Thus

$$\frac{f_2}{f_1} = -\sqrt{\frac{V_2}{V_1}} \qquad \text{A.43}$$

Which is again analogous to the corresponding law in light optics for a lens between two different media. If $f_2$ is positive, then $f_1$ is negative, but both conditions imply convergence. Thus the diverging or converging action of the lens works both ways. The sign of lens depends on the sing of "$V_0$" which determines the integral, since all other factors are positive. Thus, wherever the axial potential curves concavely upward, it is a converging region, and wherever it curves concavely downward, it is diverging.

# APPENDIX B: FABRICATION PROCESS FLOW AND RECIPE

## B.1. Process flow for a lens electrode using various wafers

Single (Cz) crystal growth, 100 mm, DSP, Prime grade, 350 μm, P-type (boron doped), 1-10 Ω.cm.

| Step | Description | Process name | Material / Chemical | Remarks |
|---|---|---|---|---|
| 1 | Native oxide strip off | HF dipping | HF (1:10), 30 s | 25–100 Å $SiO_2$ is always present on Si surface which is recommended to be stripped off. |
| 2 | Passivation layer deposition/oxidation | Thermal oxidation | Steam, 1100 $^oC$, 4 hr | 1 μm oxide to use it as oxide etch mask during DRIE. Skip it if PR is enough to protect Si Surface during DRIE |
| 3 | Circular mask patterning | Front-side Photolithography | Photomask I | First mask patterning on PR coated wafer. |
| 4 | Oxide etching | RIE | SiO2 etching | SiO2 etching to create pattern on oxide layer. Skip if if no SiO2 or $Si_3N_4$ layer. |
| 5 | Si trenches | DRIE | Si | 25 μm |
| 6 | PR strip off | Ashing | $O_2$ plasma | Acetone cleaning is also recommended. |
| 7 | Etch mask deposition | Oxidation | $SiO_2$ or Si3N4 | 1 μm oxide or nitride is sufficient to protect the Si during wet etching process. |
| 8 | Back side patterning | Photolithography | Photomask II | Bottom side alignment |
| 9 | $SiO_2$ etching | RIE | $SiO_2$ etch | 1 μm |
| 10 | Photoresist strip off | PR strip | Acetone | |

| | | | | |
|---|---|---|---|---|
| 11 | Back side Si etching to release Si membrane and circular patterns at back side etched window | Wet etch | TMAH | ~340 μm. Si is to be etched till the pattern appears at the etched window. |
| 12 | Oxide strip off to release aperture on Si membrane | Oxide strip off | BOE | 1 μm. $SiO_2$ is required to be stripped off completely. |
| 13 | Boron doping for making conductive Si membrane | Boron doping | Diffusion furnace | ~$1 \times 10^{19}$ /$cm^3$ upto ~1 μm. Skip it if substrate has already conductive Si |
| 14 | Anodic bonding with pre-fabricated Pyrex chip | Anodic bonding | >400 $^oC$, >600 V | It takes 2-10 min depending upon cleanness and current flow. |
| 15 | Release of a lens-electrode | Release | | Detach from wafer |

## B.2. Photolithography process and recipe

| **Steps** | **AZ 7220** | **AZ 1512** | **AZ 5412** |
|---|---|---|---|
| PR | Positive tone | Positive tone | Positive tone |
| Thickness (μm) | 2.7 | 1.2 | 1.2 |
| HMDS | 500 rpm, 5 s, 4000 rpm, 30 s | 500 rpm, 5 s, 2000 rpm, 10 s | 500 rpm, 5 s, 2000 rpm, 10 s |
| PR coating | 500 rpm, 5 s, 3000 rpm, 30 s | 500 rpm, 5 s, 4000 rpm, 35 s | 500 rpm, 5 s, 4000 rpm, 35 s |
| Soft bake (Hot plate) | 95 $^oC$, 60 s | 90 $^oC$, 90 s | 90 $^oC$, 90 s |
| Dose | 230-270 mJ/cm2 | 60-100 mJ/cm2 | 60-100 mJ/cm2 |
| Expose time (MA6, Hg i-line (365 nm), 15 mW/cm2 | 17 s | 6.5 s | 6.0 s |
| Developer | CD 30 | AZ 300 MIF | AZ 400K |
| Developing time | 60 s | 70 s | 70 s |
| Hard bake (hot plate) | 115 $^oC$, 90 s | 115 $^oC$, 90 s | 115 $^oC$, 90 s |

## B.3. Anodic bonding process and recipe

| Step | Description | Remarks |
|---|---|---|
| 1 | Setup the equipment as in Fig. 3.23 | Take care heating system and electric field set up |
| 2 | Place a wafer upside up on a bonding plate | Don't put the wafer if the plate is hot. Thermal stress may break the wafer. |
| 3 | Position a Pyrex chip on the Si surface | Put gently. Mind that membrane is very thin. |
| 4 | Align the circular hole of Pyrex inscribing the align keys | Use cotton ball to align the Pyrex on Si substrate. |
| 5 | Position the cathode electrode connected with a spring over the Pyrex | Use x and y screw gauges |
| 6 | Lower the cathode so that it slightly press the Pyrex ensuring the contact between wafer and Pyrex | Be careful not to apply force |
| 7 | Heat the plate above 400 oC | Set the controller temperature ~ 450 oC |
| 8 | Turn on the high voltage (>400 V) | Use the knob to increase the voltage gradually. The wire get vibrate if high current is flowing. |
| 9 | Wait till the current be steady or zero | Current initially reduces rapidly and down to steady or zero indicating the completion of bonding. |
| 10 | Turn off the high voltage and unload the bonded lens | Don't touch the bonding heater and electrodes before turn off the high voltage line. |
| 11 | For multiple Pyrex bonding, place and align Pyrex with Si membrane and repeat steps 8-10 | Take care that bonbon plate is at high temperature. Use only cotton ball to position the Pyrex on Si substrate. |

## B.4. Silicon surface cleaning

Surface cleaning is the first and mandatory process prior to any sort of additive process (*e.g.*, deposition, PR coating, and oxidation) to avoid from contamination and proper adhesion. Many methods of cleaning processes are in every day practice in micro/nanofabrication lab. Both the chemical (wet) and plasma enhanced (dry) process can be used to remove micro/nano particles from

surface. The selection of cleaning process depends on the choice of particles to be removed out. The mostly three types of contamination are occurred during the fabrication process: Particles and Metals contaminants and Organic impurities.

Micro or nano size particles get stiction on surface due to adhesion force. Adhesion force includes Van der walls force, $F_v$, and adhesion-induced deformation force, $F_{deformation}$. It is given as:

$$F_{ahesion} = F_v + F_{deformation} = \frac{AR}{6z_0^2}\left(1 + \frac{a^2}{Rz_0}\right)$$

where, A = Hamaker constant, R = Radius of particle, $z_0$ = the distance between particle and substrate (~4Å), a = contact radius, From MP model for silicon substrate, it is given as:

$$a = \sqrt{\frac{2W_A R}{H}} \qquad (1)$$

and

$$W_A = 2\sqrt{\gamma_1 \gamma_2} \qquad (2)$$

Where, $W_A$ is work of adhesion between particles and surface. 1 and 2 are surface free energy of two contact materials. For, $SiO_2$, $W_A$ = 70 mJ/m$^2$ and H = 750 MPa

To overcome this particle adhesion force, mega sonic agitation is generally carried along with chemical etching.

General Clean (SPM Clean): A mixture of Sulfuric Acid and Hydrogen Peroxide (SPM or piranha solution) does clean almost all sort of contamination

(particle, organic, inorganic or metal). The chemical reaction is very exothermic and rises temperature of solution above 100 $^{o}$C. In our laboratory, I prepare it mixing 1 part of $H_2O_2$ with 4 parts $H_2SO_4$ at chemical bath and use at 120 $^{o}$C. Here, $H_2O_2$ oxidize contaminants and $H_2SO_4$ dissolve the oxidized particles.

$H_2SO_4 + H_2O_2 = H_2SO_5 + H_2O$

For example, $H_2SO_5$ oxidizes the carbon compound and reduces to $H_2SO_4$:

$H_2SO_5$ + Carbon Compound = $CO_2 + H_2SO_4 + H_2O$

The solution can be re-vitalized by adding little amount of $H_2O_2$ if the solution gets cool after its use. 10 minute clean is normally carried out and followed by at least 30 min rinsing in running DI water for sample. For small size sample, it is important to increase the rinsing time for well cleaning of the SPM cleaned sample.

Particle Removal (SC-1): A mixture of ammonium hydroxide, hydrogen peroxide and water in ratio (1:1:5) at about 70 $^{o}$C will remove silica and silicon particles from the wafer, as well as it removes certain organic and metal surface contamination. It is also called standard cleaning-1 (SC-1) as it is first employed to bare wafer before it is used for further process. About 10 minute cleaning is normally carried out in our laboratory. Additional mega sonic agitation can be done with this SC-1 cleaning.

Oxide Removal (HF dip): A 10-60 second dip in 1:10 HF:DI water removes the native oxide layer (~30-100 Å). HF reduces the oxide in forming a water soluble compound.

$6HF + SiO_2 = H_2SiF_6 + 2H_2O$.

$NH_4F$ can be used as buffering agent for this solution which keeps almost constant the concentration of HF by reverse reaction.

HF dip is normally carried out in before processing the bare wafer and wet etching of silicon for short time (e. g., 10 s) to strip of the native oxide (~20 Å). HF dip is not required for the process which has been already re-oxidized to retain the oxide thickness.

Metal Contamination Removal (SC-2): A mixture of HCl, $H_2O_2$, and DI water in ratio (1:1:5) at temperature about 70 $^oC$ removes certain ionic and metal surface contamination. I normally do 10 minute cleaning and followed by strong rinse in DI water.

Degreasing and solvent cleaning: Acetone, methanol, iso-propanol (IPA) and DI water in sequential cleaning is useful to remove photoresist and organic contaminants. This cleaning process is useful even the metal deposited sample. The usual cleaning process includes acetone (boiling) (5 min) → methanol (5 min) → IPA (5 min) → running DI water (15 min).

Spin, Rinse, and Dry: It is a standard process to dry wafer which also help in cleaning wafer better.

Quick, Dump, and Rinse (QDR): Quick dump and rinse QDR) is a fast cleaning method in DI (deionized) water and N2 bubble without using any chemicals. It is just DI water cleaning to remove surface dust, chemicals, etc. QDR is carried out in almost every steps of chemical processing.

---